Revista ALCONPAT

Journal of the Latin-American Association of Quality Control, Pathology and Recovery of Construction

Complete issue DOI: http://dx.doi.org/10.21041/ra.v6i2

revistaalconpat@gmail.com

eISSN: 2007-6835 Volume 6 May - August 2016 Issue 2

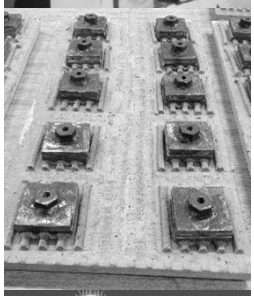

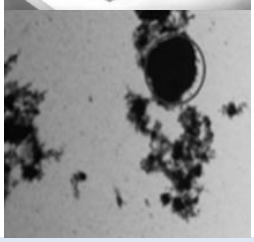

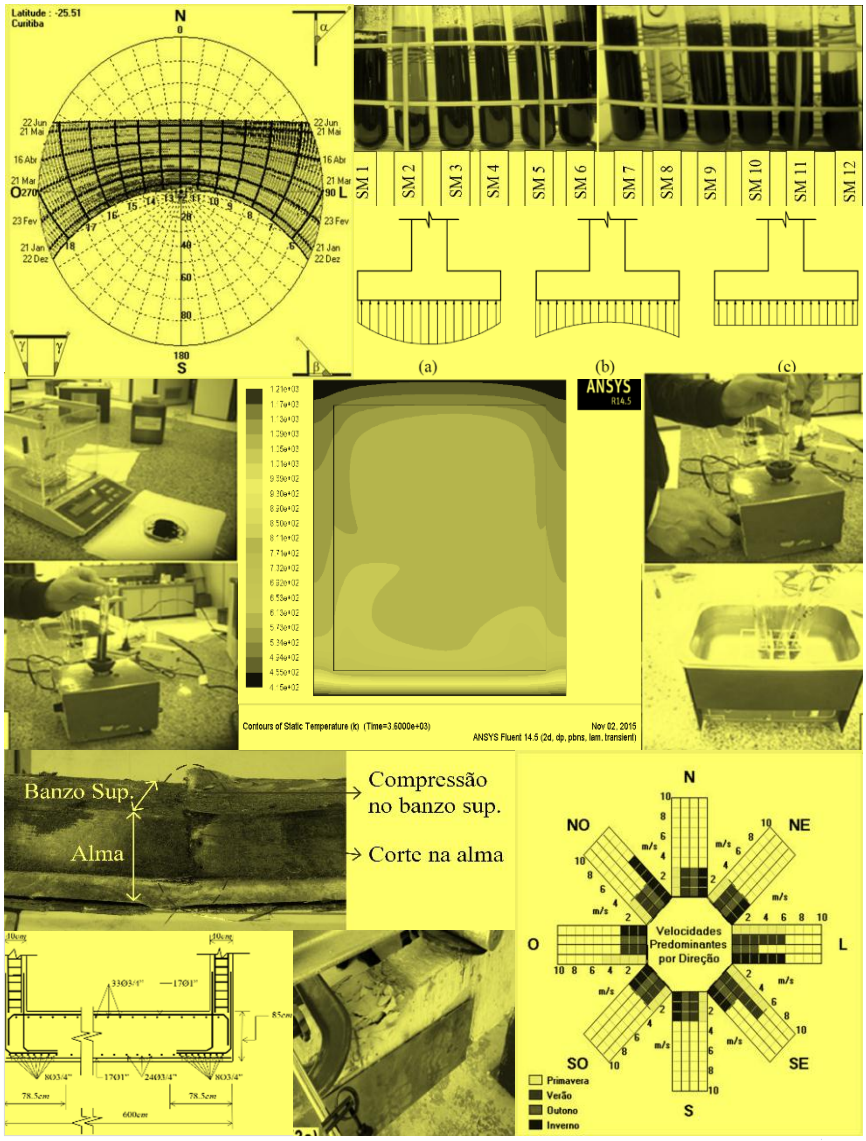

Journal of the Latin-American Association of Quality Control, Pathology and Recovery of Construction

http://www.revistaalconpat.org

RAV6N2, May – August 2016

Message from the Editor-in-chief

LATIN AMERICAN JOURNAL ON QUALITY CONTROL, PATHOLOGY, AND THE RECUPERATION OF CONSTRUCTION

www.revistaalconpat.org

It is gratifying for the team of the ALCONPAT Journal to see the second issue of our sixth year published.

The purpose of the ALCONPAT (RA) Journal is to publish case studies related to the topics of our association, such as quality control, pathology, and the recuperation of constructions, all the while motivating the presentation of basic or applied researches, revisions, or documental researches.

This edition V6N2 begins with a work from **Brazil**, in which C. G.N. Marcondes and M. H. F. Medeiros demonstrate that hierarchical analysis is an efficient tool in investigating the dispersion efficiency of carbon nanotubes in a water in concrete mixture. Twelve types of dispersions were studied for multi-walled carbon nanotubes both in dust form and already dispersed in water in an aqueous medium with various chemical products.

The second work, from **Mexico**, by L. Y. Gómez-Zamorano and C. E. Castillo-Linton, deals with the evaluation of the effect of adding silica nanoparticles (SN) to two cementing matrices, ordinary Portland cement based as well as sulphoalumineous cement based, with the purpose of establishing its influence on the mechanical properties and the chemical resistance of said materials. To this end, the SN were added in dosages of 0.30% to 5.0% in weight. The results indicated that both the resistance to compression and to a chemical attack by sulfates were improved due to the addition of SN.

In the third article, from **Brazil**, P. Valentini and C. S. Kazmierczak analyze the pathological manifestations that can occur in ceramic tiles, such as the loss of adherence, which is considered the most serious due to the risk of accidents by falling and the elevated repair costs. This work had the objective of evaluating the influence of the properties of different ceramic slabs, applied with two types of mortar and subject to three different curing conditions (established by standard ABNT 14.081-4:2012), on the adherence resistance of the coating system. It was observed that the type of curing is the variable that shows the most significant influence on the adherence resistance, followed by the type of mortar used.

The fourth article is from **Argentina**, by Néstor F. Ortega et al., and deals with the results obtained from exposing reinforced concrete beams subject to flexural stress to a process of accelerated corrosion, thus generating tensile stress on the corroded reinforcement. The results evidenced the influence of the reinforcement coating thickness on the corrosion process and its external manifestation (cracking of the coating), considering the same mechanical needs.

The fifth work in this issue is from **Brazil**, by Wellingthon Mazer et al., and evaluates the incidence of the pathological manifestations in the facades of buildings correlated with the geographical direction. It was found that the pathological manifestations in the facades appear in different amounts and directions, having identified a relation with the temperature variation and the direction of the wind in function of the geographical orientation.

The sixth article is from **Portugal**, in which Tiago Morgado et al. present a study on the fire resistance of beams manufactured with profiles of glass fiber reinforced polymer (GFRP). With the results obtained, it was possible to develop a numeric model in the ANSYS FLUENT software to simulate the evolution of the temperature ranges in the cross-section, as well as an analytical model to determine the evolution of the deformation of the beams.

The seventh work is by Arnulfo Luévanos Rojas, from **Mexico**, in which a model is presented for the design of rectangular combined boundary footings with two restricted opposite sides, considering the real pressure of the ground on the contact surface of the footing. The mathematical focus suggested in this work produces results that have a tangible precision to find the most economical solution.

The closing article is by Caroline C. Deghenhard et al., from **Brazil**, who present a work on external structural reinforcement through steel sheets adhered with epoxy adhesive as an option to increase the load capacity of reinforced concrete elements. As a result, they present a relative comparison on the performance of the beams.

In this V6 N2, RA is pleased to increase its publication rate from 6 to 8 articles per issue, thanks to the enthusiastic participation of its authors and readers. It should be noted that RA now has DOI numbers to facilitate the indexation and localization of the works. Likewise, RA launched an OJS portal and a more user-friendly address for our readers (www.revistaalconpat.org). We thank the authors participating in this issue for their willingness and effort in presenting quality articles and for their compliance regarding the established deadlines.

By the Editorial Board

Pedro Castro Borges
Editor-in-chief

Revista ALCONPAT

Journal of the Latin-American Association of Quality Control, Pathology and Recovery of Construction

Complete issue DOI: http://dx.doi.org/10.21041/ra.v6i2

revistaalconpat@gmail.com

eISSN: 2007-6835 Volume 6 May - August 2016 Issue 2

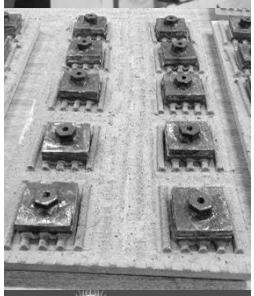

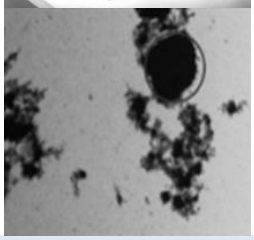

CONTENT

ALCONPAT Journal
www.revistaalconpat.org
eISSN 2007-6835
Journal of the Latin-American Association of Quality Control, Pathology and Recovery of Construction

Analyzing the dispersion of carbon nanotubes solution for use in Portland cement concrete

C. G. N. Marcondes[1]; M. H. F. Medeiros[2]

[1] Pontifical Catholic University of Paraná (PUCPR), Brazil.
[2] Department of Civil Engineering, Federal University of Paraná, Brazil.

Article information
DOI:
http://dx.doi.org/10.21041/ra.v6i2.131
Article received on January 29th 2016, reviewed under publishing policies of ALCONPAT journal and accepted on April 14th 2016. Any discussion, including the replica of the authors, shall be published in the first number of the year 2017 as long as the information is received prior to the closing of the third number of the year 2016.

ABSTRACT
Carbon nanotubes (CNTs) are nanometric carbon structures with cylindrical formats. For use in concretes, one of the difficulties is in its dispersion, focus this work. It used a tool known as hierarchical analysis to investigate the efficiency of the dispersion of carbon nanotubes in concrete kneading water. Were studied 12 forms of dispersions in aqueous medium containing hum Miscellaneous Chemicals. Carbon nanotubes multi-walled in powder form and Processed already dispersed in water were used. The study showed that the hierarchical analysis tool might constitute an alternative to the election of the best choice among the available options, considering the factors of influence in a systemic way.
Keywords: analytical hierarchy process; concrete; carbon nanotubes

RESUMO
Os nanotubos de carbono (CNT) são estruturas nanometricas de carbono com formatos cilíndricos. Para uso em concretos, uma das dificuldades está na sua dispersão, foco deste trabalho. Foi usada uma ferramenta conhecida como análise hierárquica. Para investigar a eficiência da dispersão dos nanotubos de carbono na água de amassamento do concreto, foram estudados 12 formas de dispersões em um meio aquoso contendo diversos produtos químicos. Foram utilizados os nanotubos de carbono de paredes múltiplas em forma de pó e os industrializados, já dispersos em água. O trabalho demonstrou que a ferramenta de análise hierárquica poderia se constituir em uma alternativa eficiente para a eleição da melhor dispersão, considerando os fatores de influência de forma sistêmica.
Palavras-chave: análise hierárquica; noncreto; nanotubos de carbono.

RESUMEN
Los nanotubos de carbono (CNT) son estructuras nanométricas de carbono en formas cilíndricas. Para su uso en hormigón, una de las dificultades es su dispersión, enfoque de este trabajo. Se utilizó una herramienta conocida como análisis jerárquico para investigar la eficiencia de dispersión de los NTC en el agua de la mezcla de hormigón. Fueron estudiados 12 maneras de dispersiones en medio acuoso que contiene diferentes productos químicos. Se fue utilizado los nanotubos de carbono de pared múltiple en forma de polvo y los ya procesados, dispersos en agua. El estudio mostró que la herramienta de análisis jerárquico podría constituir una alternativa eficaz para la elección de una mejor dispersión, teniendo en cuenta los factores que influyen en forma sistémica.
Palabras clave: proceso de análisis jerárquico; hormigón; nanotubos de carbón.

Autor de contacto: Marcelo Medeiros (medeiros.ufpr@gmail.com)

1. INTRODUCTION

Research in cement and nanotechnology areas, such as Makar et al. (2005), Gleize (2007), Nochaiya e Chaopanich (2011), have shown that some nano-composite additions on cement may allow important changes in the cementitious composites properties, allowing the production of stronger cements, less porous and durable. Among these possible nano materials are carbon nanotubes (CNT), the main focus of this paper.

Carbon nanotubes (CNTs) are carbon structures that, once synthesized, get cylindrical shape in nanometer scale and measure approximately 3nm in diameter and 1000nm in length, one nanometer corresponds to 10E-9 meter (Couto, 2006).

From the structural point of view, there are two types of carbon nanotubes: single wall, consisted of a single graphene sheet rolled up on itself to form a cylindrical tube, and multiple walls, comprising a set of coaxial carbon nanotubes, with several graphene sheets rolled up into a tube (Zarbin, 2007). Single-walled carbon nanotubes (SWNTs) are more difficult to be synthesized, which increases their cost and virtually precludes its application in large scale.

The addition of CNTs to cementitious compounds is a topic that has been studied by various brazilian and international universities and the justification for this is that some surveys, attest the good performance of nanoparticles when added to Portland cement mortars and pastes. However, there are still some barriers to overcome. According to Batiston (2012), the two main challenges for the introduction of carbon nanotubes in cementitious matrices are: homogenizing the distribution of carbon nanotubes in the matrix and tailoring the interaction of CNTs with the resulting compounds from the hydration of cement.

Regarding the distribution of CNTs to a cementitious matrix, several methods have been used, highlighting the sonification and functionalization of CNTs using nitric and sulfuric acid mixture. An appropriate dispersion of carbon nanotubes (CNTs) is a prerequisite for their use in improving the mechanical properties of cement-based composites (Sobolkina et al., 2012).

For researchers Koshio et al. (2001), ultrasound can be considered an effective technology for dispersing carbon nanotubes in water, oil or polymers. For them, the shear forces generated by ultrasound outweigh the attraction forces between the nanotube particles, being able to separate them. This has been proven by Konsta et al. (2010) who achieved an efficient dispersion by application of ultrasonic energy and the use of a surfactant. The results of this research show that there was adequate dispersion with the application of ultrasonic energy. It was also evident in this study that multi-walled carbon nanotubes can reinforce cement matrix, while increasing the amount of CSH and reducing porosity. This contribution is also due to the fineness of the particles, which results in a reduction of the pore size of the hydrated cement paste (Neville, 1996).

As the use of carbon nanotubes in cement compounds is a field of study in its early stages and promising development, this study aims to contribute to a better understanding regarding the carbon nanotube dispersion efficiency in aqueous solutions. In order to choose the best additions to perform the dispersion was employed hierarchical analysis tool, which will be presented below, and has the advantage of being a systematic method of choice, in which several criteria can be evaluated in a comprehensive manner.

2. THEORY OF HIERARCHICAL ANALYSIS

The Analytical Hierarchic Process, AHP, is one of the multi-criteria analysis methodologies that assists the decision making in several fields of human knowledge. In civil engineering, the potential of AHP has been little explored, however it is possible to mention examples of studies that have used this tool as a decision making tool, such as: Marchezetti et al. (2011), in the treatment of household waste; Lai et al. (2008), in public works projects; Costa and Correa (2010), in post-occupation evaluation of buildings;

Pereira, Medeiros and Levy (2012) and Mattana et al. (2012) in studies on recycling of construction waste for the manufacture of concrete and mortar.

According to Costa (2002) the method proposed by Saaty in the early 70s (Saaty, 1978), can be classified as one of the most known and used methods of multi-criteria analysis, aiming at the selection/choice of alternatives in a process that considers different evaluation criteria.

For the use of this important tool that deals with complex problems in a more simplified way, key elements are needed to determine the global target: feasible alternatives and the set of criteria and attributes. It is important that the user of the technique is aware that the established criteria do not cause a superposition effect on each other and are able to cover all solutions of the problem.

The AHP allows to consider the subjectivity of some parameters and uses forms of judgment to quantify these items, so that hierarchical levels are built. The results are presented in the format of priorities, enabling the determination of how much one alternative is superior to the other, or their degree of importance about the other variables.

This review influences the quality and effectiveness of the obtained results, since it is the evaluator's responsibility to determine the modelling of alternatives and criteria, and the judgment on the assigned values in the involved evaluations. Requiring the evaluators knowledge about the subject of each topic.

3. EXPERIMENTAL PROCEDURE

The focus of the developed experiment is basically to classify a composition and a dispersion method of carbon nanotubes in aqueous solution. The reason is the fact that being the carbon nanotubes previously dispersed in water, its distribution in the concrete mass to be made will be more homogeneous than if the CNT powder is simply added to the mixer at the time of concrete manufacture. With this focus, 12 dispersion alternatives were evaluated by the point of view of turbidity, diameter of group formation and sedimentation tendency. Table 1 shows the general plan of the experiment, with the number of samples and the used dosage.

Table 1. Overview of the experiment.

Sample	Description	Dosage
SM 1	CNT in powder with water	10g water + 0.03g of CNT
SM 2	CNT in powder with water and additive based on polycarboxylate (Tec Flow 8000 – at 2% relative to the mass of water)	10g water + 0.03g of CNT + 0.2g of additive
SM 3	CNT in powder with water and additive based on polycarboxylate (Tec Flow 8000 – at 1% relative to the mass of water).	10g water + 0.03g of CNT + 0.1g of additive
SM 4	CNT Aquacyl 0301 with water.	9.03g water + 1g of CNT Aquacyl 0301
SM 5	CNT Aquacyl 0301 with water and additive based on polycarboxylate (Tec Flow 8000 - at 1% relative to the mass of water).	9.03g water + 1g of CNT Aquacyl 0301 + 0.1g of additive.
SM 6	CNT Aquacyl 0301 with water, CNT in powder and additive based on polycarboxylate (Tec Flow 8000 - at 1% relative to the mass of water).	9.57g water + 0.5g of CNT Aquacyl 0301 + 0.015g CNT in powder + 0.1g of additive
SM 7	CNT Aquacyl 0301 with water and additive based on polycarboxylate (Tec Flow 8000 – at 0.5% relative to the mass of water).	9.03g water + 1g of CNT Aquacyl 0301 + 0.05g of additive.

SM 8	CNT Aquacyl 0301 with water, CNT in powder and additive based on polycarboxylate (Tec Flow 8000 – at 0.5% relative to the mass of water).	10g water + 0.03g of CNT + 0.05g of additive.
SM 9	CNT Aquacyl 0301 with water, and CNT in powder.	9.57g water + 0.5g of CNT Aquacyl 0301 + 0.015g CNT in powder
SM 10	CNT Aquacyl 0301 with water, CNT in powder and additive based on polycarboxylate (Tec Flow 8000 – at 0.5% relative to of water).	9.57g water + 0.5g of CNT Aquacyl 0301 + 0.015g CNT in powder + 0.05g off additive
SM 11	CNT in powder and gum arabic and water	9.0g water + 1g Goma arabic + 0.03g CNT in powder
SM 12	CNT in powder and water with surfactant - Sodium Lauryl Ether sulfate	– 10g water + 0.03g of CNT in powder + 0.1g of surfactant.

3.1. Materials

The materials employed were: carbon nanotubes (CNT), superplasticizer admixture, distilled water, Arabic gum and Lauryl ether sodium sulfate.

In the case of Arabic gum, the manufacturer does not provide data of chemical and mechanical characterization, therefore, it is not presented in this paper. The sodium Lauryl Ether sulphate is basically a chemical product which formula is $CH_3(CH_2)10CH_2(OCH_2CH_2)nOSO_3Na$. Both materials had already been searched by Ibarra et al. (2006) and Metaxa et al. (2012) respectively, which obtained good dispersion results.

The CNTs used in this research were acquired in Nanocyl SA company, located in Belgium. The amount paid for the powder product was 120 Euros per kilo. These are multi-walled CNTs synthesized by the method of chemical vapour deposition, also called CVD. Commercially the products are specified with the names NC 7000 for powder form and AQUACYL 0301, to the one already dispersed in water. Both cases were employed in this study.

Tables 2 and 3 show the chemical and physical information of CNTs used in this study.

To perform the experiment, a superplasticizer based on polycarboxylate admixture was used. Polycarboxylate are macromolecules used as dispersants in cementitious compositions of high efficiency by reducing the viscosity of the suspensions and minimizing the amount of water used for the process (Mehta; Monteiro, 2013).

Table 2. CNT characterization provided by the manufacturer.

Properties	**Unity**	**Value**
Average diameter	nanometers	9.5
Average length	micron	1.5
Carbon purity	%	90
Metal oxide	%	10
Surface area	m^2/g	250-300
Average density	g/l	60

Table 3. Product composition provided by the manufacturer.

Components	**% (weight)**
Synthesized graphite (CNT)	90%
Cobalt oxide	< 1%
Others	9%

The admixture used in the experiment consists of a carboxylic ether polymer modified with a solid concentration of approximately 49%. The product meets the requirements of ASTM C 494/2013 (TYPE A and F) (2013), ASTM 1017/2007 (2007), NBR 11768/2011 (2011). Some of its properties can be viewed in Table 4.

Table 4. Information about the superplasticizer admixture provided by the manufacturer.

Recommended dosage (on weight of cement)	pH (ABNT 10908)	Specific mass (ABNT 10908)
0.3% a 2%	5.5 ± 1,0	1.10 ± 0.02 g/cm^3

3.2. Procedure for the preparation of CNT dispersion

Figure 1-a shows the weighing of nanotubes using an electronic balance accurate to 0.001g. In all cases, the percentage of 0.3% in relation to the total water added was maintained. The mixtures were made in test tubes, which were shaken in a mechanical shaker (Figure 1-b, before, and Figure 1-c, after shaking). As a next step, the solutions in the test tubes were subjected to sonication in an ultrasound bench device, from Thornton Ltd. with a nominal frequency of 40 KHz and 100W of power (Figure 1-d).

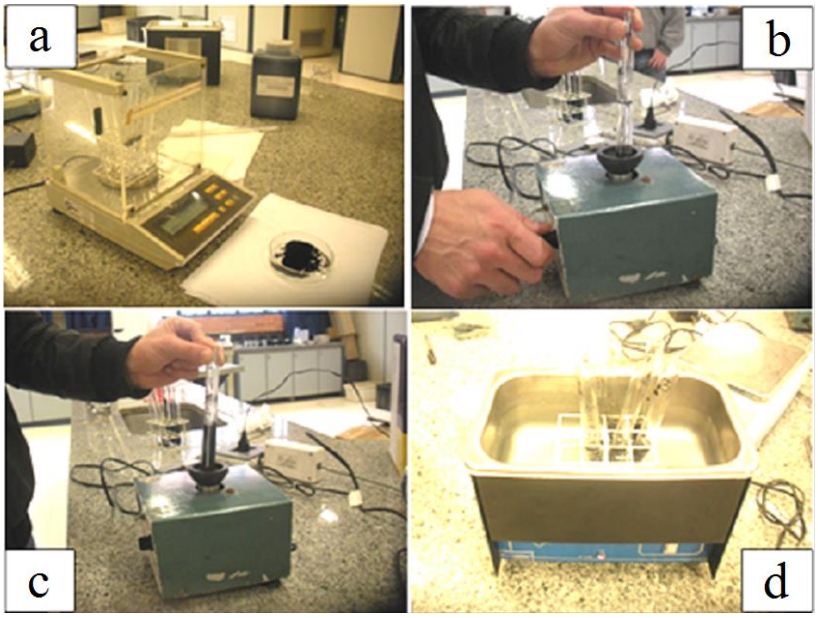

Figure 1. a) Weighing of CNTs in balance, b) appearance of the solution prior to mechanical agitation, c) appearance of sample after mechanical agitation, d) samples in ultrasound.

The sample remained in the ultrasound for 1 hour. This time was determined based on a visual analysis that indicated that after 60 minutes, the samples showed no changes regarding tonality and turbidity and showed no settling after a rest time of 24 hours, as explained in section 3.3

3.3. Defining the sonication time of dispersions

This part of the study was intended to determine the permanence time of the aqueous solutions, with CNT, in ultrasound. Thus, dispersions were made by using the times of 10, 20, 40 and 60 minutes in ultrasound. The objective was to set a time of sonication that would generate a minimal incidence of dispersion decantation after 24 hours of settling. Figure 2 is a comparison example of decantation after 24 hours and for 40 minutes of sonication.

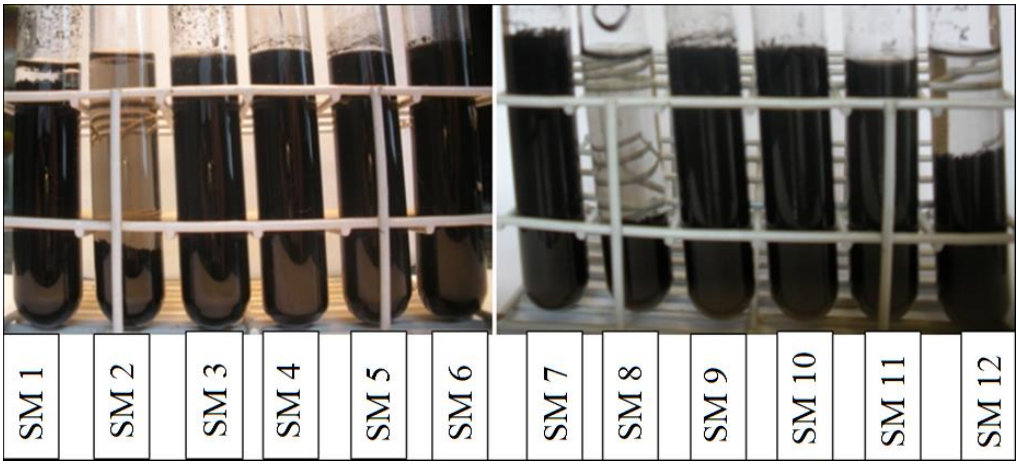

Figure 2. Visual analysis of samples with sonication time of 40 minutes after 24 hours of rest.

The result of this comparison is shown in Table 5 and indicates that sonication times of 40 and 60 minutes were those with lower occurrence of decantation. Thus, it was decided that this study would have as standard procedure to fix a time of 60 minutes for submission to sonication.

Table 5. Samples decantation after 24 hours at rest in relation to the time of ultrasonic waves' application.

Samples / Sonication time	**SAM1**	**SM2**	**SM3**	**SM4**	**SM5**	**SM6**	**SM7**	**SM8**	**SM9**	**SM10**	**SM11**	**SM12**	**Total occurrences of decantation**
10 min.	Y	Y	Y	N	N	N	N	Y	N	N	Y	Y	6
20 min.	Y	Y	Y	N	N	N	N	Y	N	N	Y	Y	6
40 min.	Y	Y	N	N	N	N	N	Y	N	N	N	Y	4
60 min.	Y	Y	N	N	N	N	N	Y	N	N	N	Y	4

Y – Decantation occurred
N – Decantation did not occurred

3.4. Use of microscopy for dispersions evaluation

After preparing the samples of dispersions, they were analyzed in an optical reflection microscope brand Olympus, model BX60 equipped with a digital camera Olympus UC 30 that can be observed in Figure 3. Images were made with different magnifications (50x, 100x and 200x) with lighting in clear weather and lower incidence.

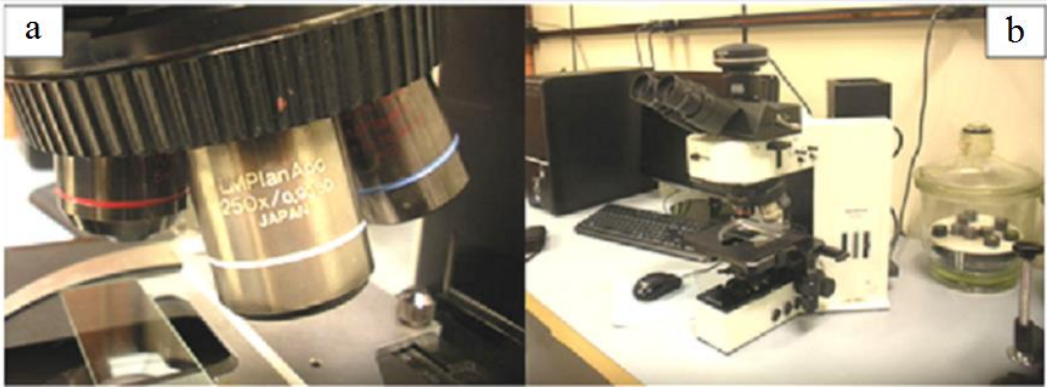

Figure 3. a) Detail of the equipment's lens b) Olympus BX 60 microscope.

Samples were collected from the test tube, immediately after preparation, before the decantation of the CNTs occurred and arranged in glass plates with the help of a pipette, dripping one drop on each plate. In all tests, it was used the incidence of illumination from down in order to examine the transparency and turbidity of the sample.

3.5 Evaluation Criteria

Three criteria for evaluation of dispersion of carbon nanotubes were used in this study. Turbidity, the diameter of clumps and decantation. The explanation of each of these criteria is presented below:

3.5.1 Turbidity

Turbidity is a physical property of fluids which results in reduction of their transparency due to the presence of suspended materials that interfere with the passage of light trough them. However, the complexity of optical interactions between incident light, optical properties of the suspended and dissolved materials, in particular its refractive index and color, turn turbidity a subjective visual property, not behaving as a directly measurable physical quantity. However, analysis of this criterion was performed in qualitatively way with the visualization or not of turbidity and its classification was made by three parameters that can be seen in Table 6. Thus, the more turbid the solution is, the more efficient the CNTs dispersion was. To determine the turbidity, it was used the incidence of light under the sample to make sure the samples were always photographed focusing the edge of the dispersed solution drop.

Table 6. Parameters for analysis and classification of turbidity.

Incidence of light passing through the sample	Parameters	Classification
No incidence of light	Blurred	Great dispersion
Low incidence of light	Translucent	Good dispersion
High incidence of light	Translucent	Bad dispersion

3.5.2 Diameters of clumps

The formation of clumps denotes the agglutination of particles and therefore that there was no efficient dispersion of CNT in the sample. The larger the diameter of the formed clump is, the less efficient the dispersion was. The images obtained by microscopy allowed to measure the diameter of clumps formed in each sample. To measure the clumps images increased 50 x in microscope were used, and it was agreed to measure, in microns, the diameter of the greater clump found. The measurement was made by comparison with the reference scale of the image. Figure 4 illustrates the adopted procedure.

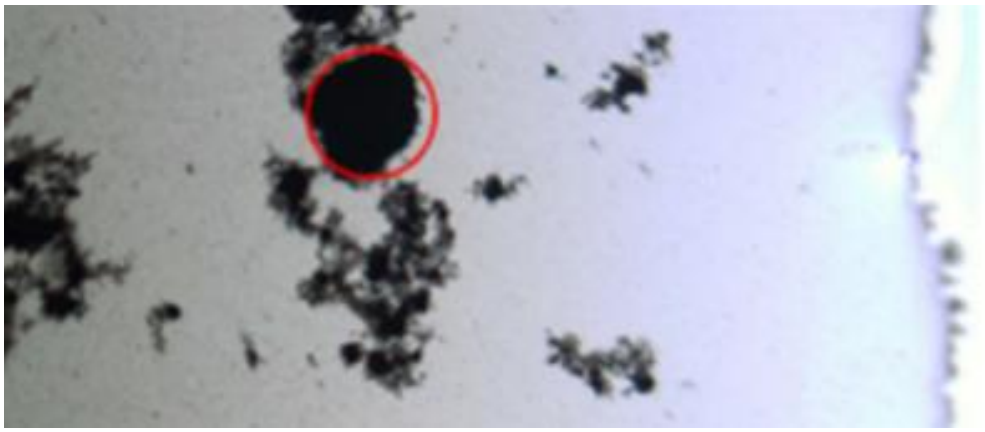

Figure 4. Measurement of the diameter in microns of the largest CNT clump.

3.5.3 Decantation in test tube

Decantation is the process of separating the phases of a mixture or solution (see Figure 3). If there is considerable portion of particles in the sample, it means that there was no decantation. This is important so that there is proper dispersion of CNTs in aqueous media, and the higher the concentration of suspended particles is, the better, as for making concrete with CNTs it will be initially necessary to perform the CNTs dispersion in a liquid for later implementation.

4. RESULTS AND DISCUSSION

4.1. Evaluation of microscopy photos

In Figure 5 to 16 it is possible to view photos taken on the microscope that were used for analysis of turbidity and size of formed clumps. They have magnifications of 50x, 100x and 200x, which can be perceived in images A, B and C - respectively, in each figure. As a standardized form of images, all photos were taken using as reference one of the edges of the drop placed on a glass plate. In the photos, it is also possible to see the size of clumps formation as well as the transparency of samples with light with low incidence.

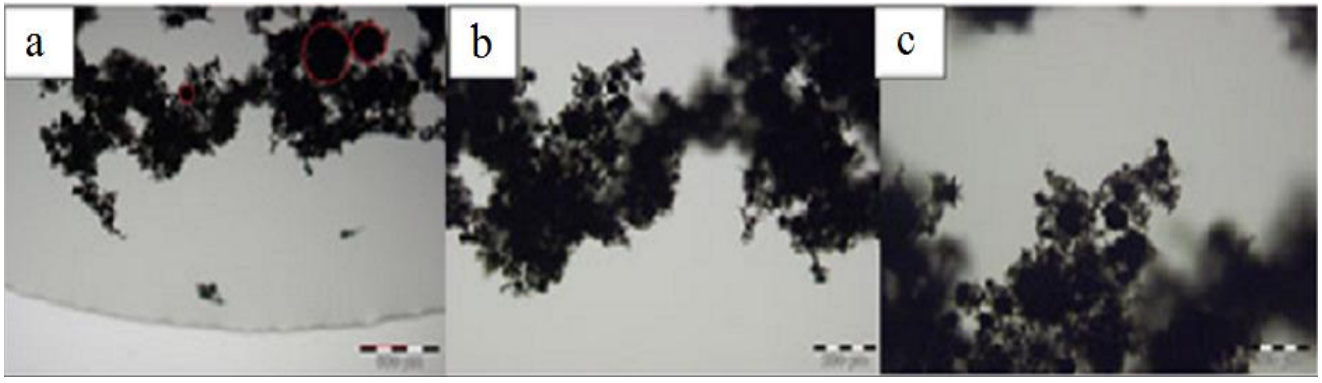

Figure 5. Sample SM 1 - powder CNT dispersed in water alone.

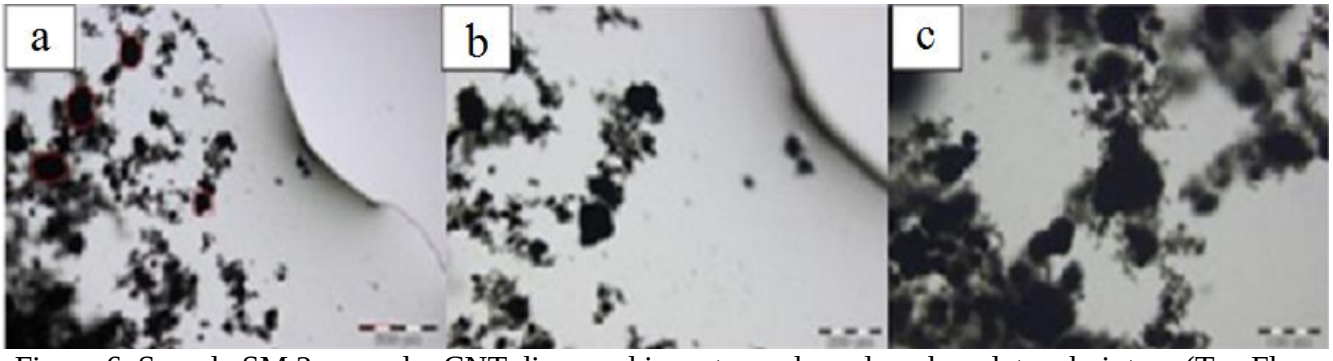

Figure 6. Sample SM 2 - powder CNT dispersed in water and a polycarboxylate admixture (Tec Flow 8000 - at 2%).

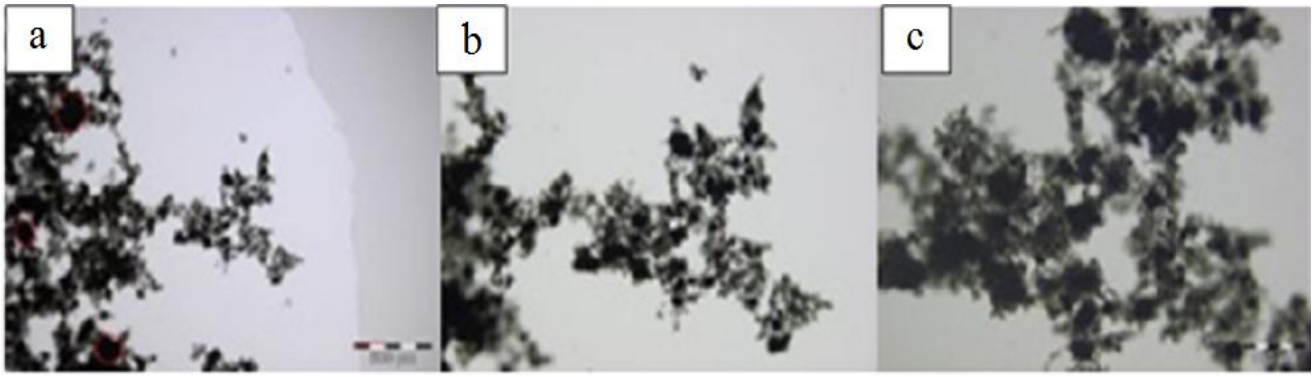

Figure 7. Sample SM 3 - powder CNT dispersed in water and a polycarboxylate admixture (Tec Flow 8000 - at 1%).

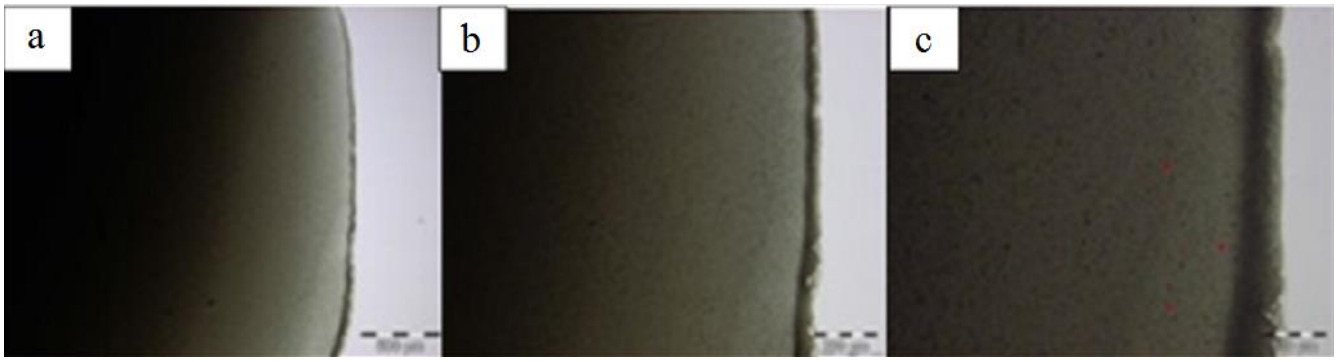

Figure 8. Sample SM 4 - CNT Aquacyl 0301 dispersed in water.

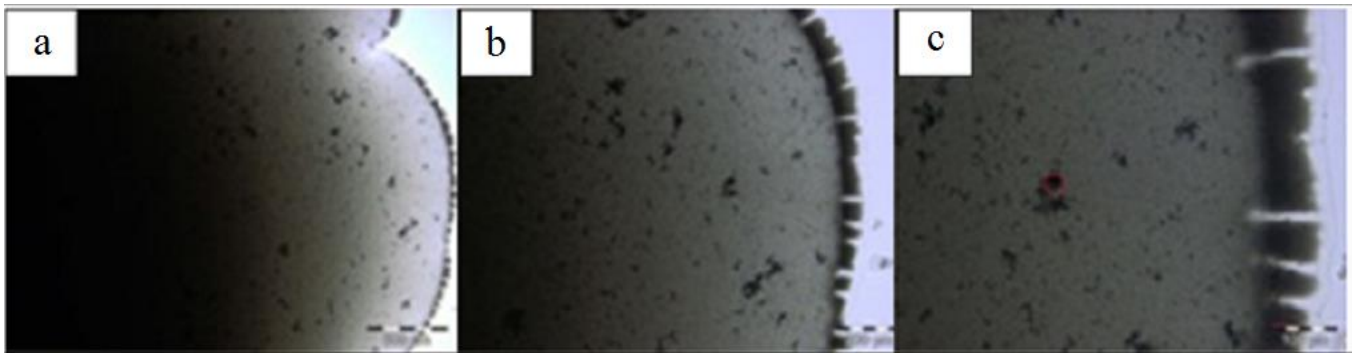

Figure 9. Sample SM 5 – CNT Aquacyl 0301 dispersed in water and polycarboxylate admixture (Tec Flow 8000 - at 1%).

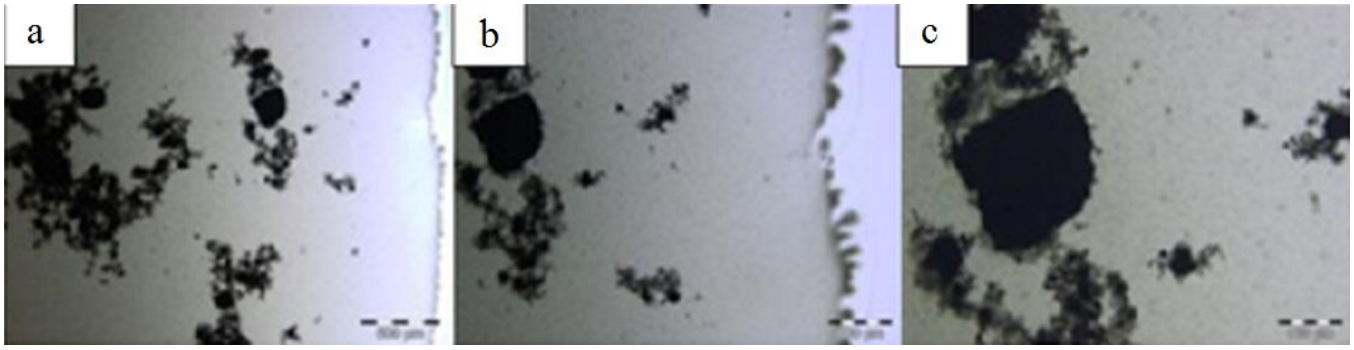

Figure 10. Sample SM 6 - CNT Aquacyl 0301 dispersed in water, with powder CNT and polycarboxylate admixture (Tec Flow 8000 - at 1%).

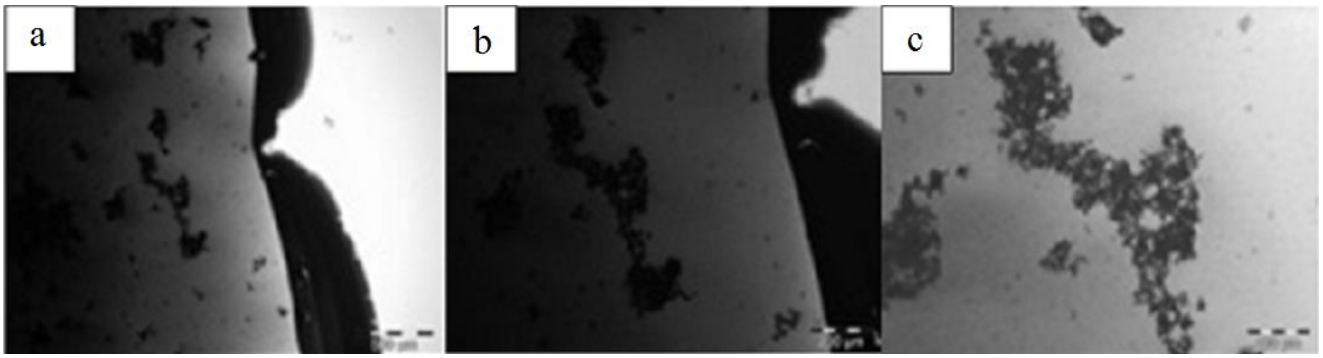

Figure 11. Sample SM 7 - CNT Aquacyl 0301 dispersed in polycarboxylate admixture (Tec Flow 8000 - at 0.5%) and water.

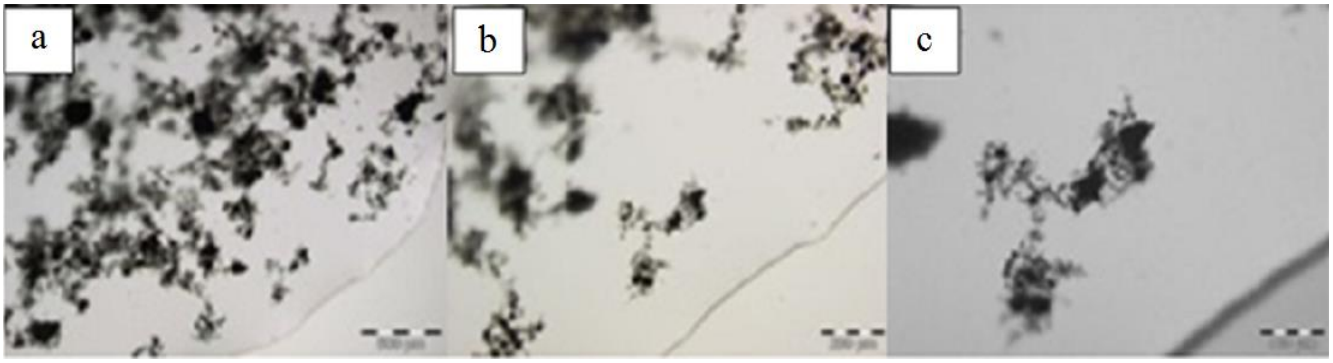

Figure 12. Sample SM 8 - powder CNT dispersed in polycarboxylate admixture (Tec Flow 8000 - at 0.5%) and water.

Figure 13. Sample SM 9 - CNT Aquacyl 0301 dispersed in water and powder CNT.

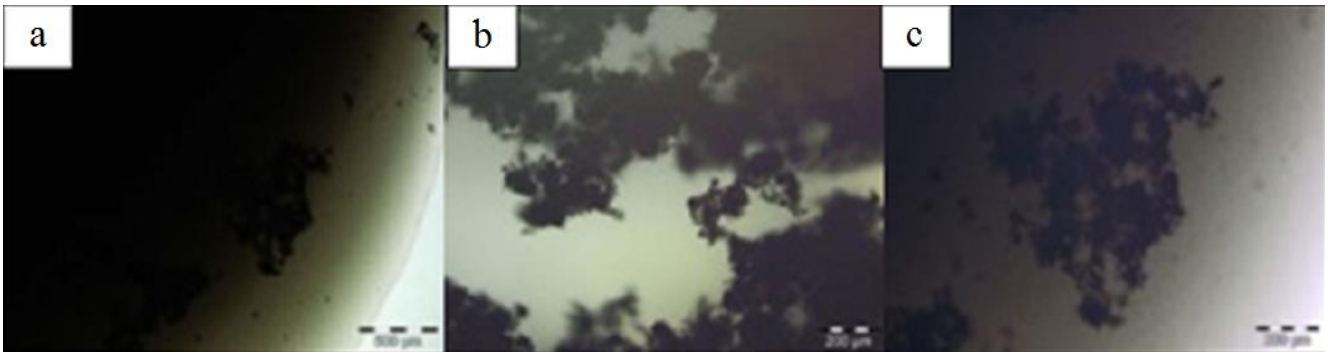

Figure 14. Sample SM 10 - CNT Aquacyl 0301 dispersed in water, with powder CNT and polycarboxylate admixture (Tec Flow 8000 - at 0.5%).

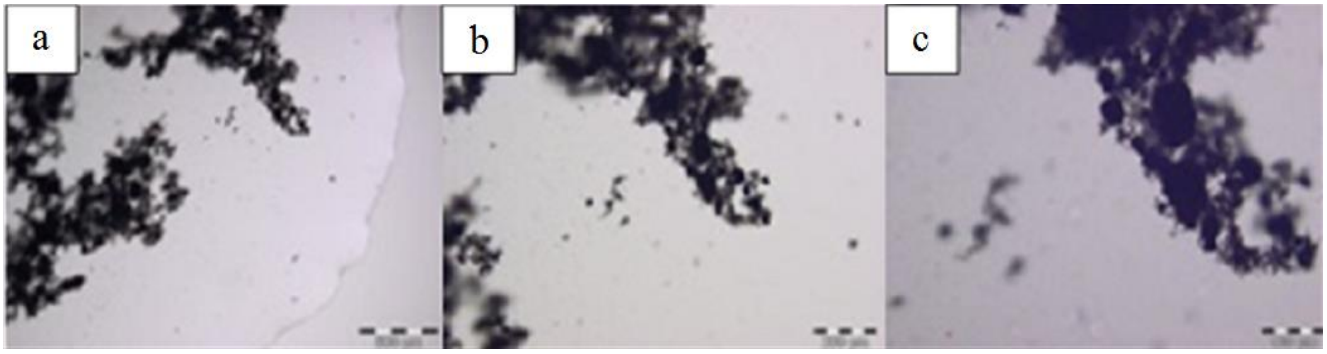

Figure 15. Sample SM 11 - powder CNT dispersed with Arabic gum and water.

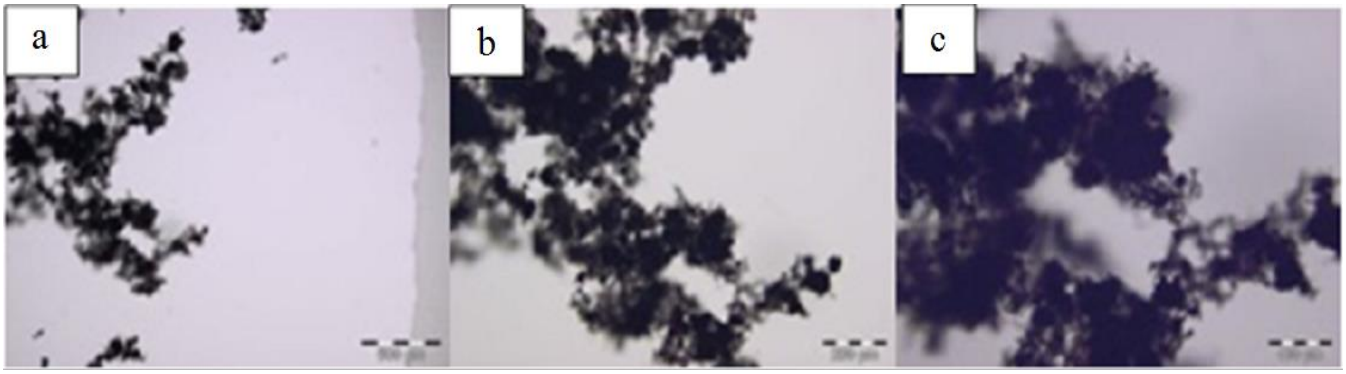

Figure 16. Sample SM 12 - powder CNT dispersed in water and surfactant.

Comparing sample SM 4 (Figure 8), which is the case of the industrially dispersed product (Aquacyl) mixed with water and subjected to 60 minutes of sonication, with the cases where were used the CNTs in powder for dispersion, it is verified that none of alternatives using powder CNT (Figures 5 to 7, Figure 10 and Figures 12 to 16) resulted in the same efficiency of the industrial dispersion of the supplier. Exceptionally, the manufacturer does not provide information about the technique used to disperse the CNTs. It is noteworthy that this difference was verified by microscopic evaluation, although many of the dispersions made with powder CNT were visually identical to SM 4, as can be seen in Figure 2.
It can be seen that, in sample SM 5 (Figure 9), with superplasticizer additive TF8000 and Aquacyl product, CNTs formed some clumps and had an orientation at the edge of the drop solution. It is possible to imagine that the additive action was the cause for this occurrence, since in the sample containing only the Aquacyl and water (SM 4) this was not observed (Figure 8).

4.2. Application of hierarchical analysis for interpreting results

For the purposes of analyzing the efficiency of dispersion three criteria were adopted. In Figure 17 there is a general flowchart of the application of hierarchical analysis, showing that the criteria considered in the evaluation were: turbidity of dispersion, diameter of formed clumps and decantation tendency.

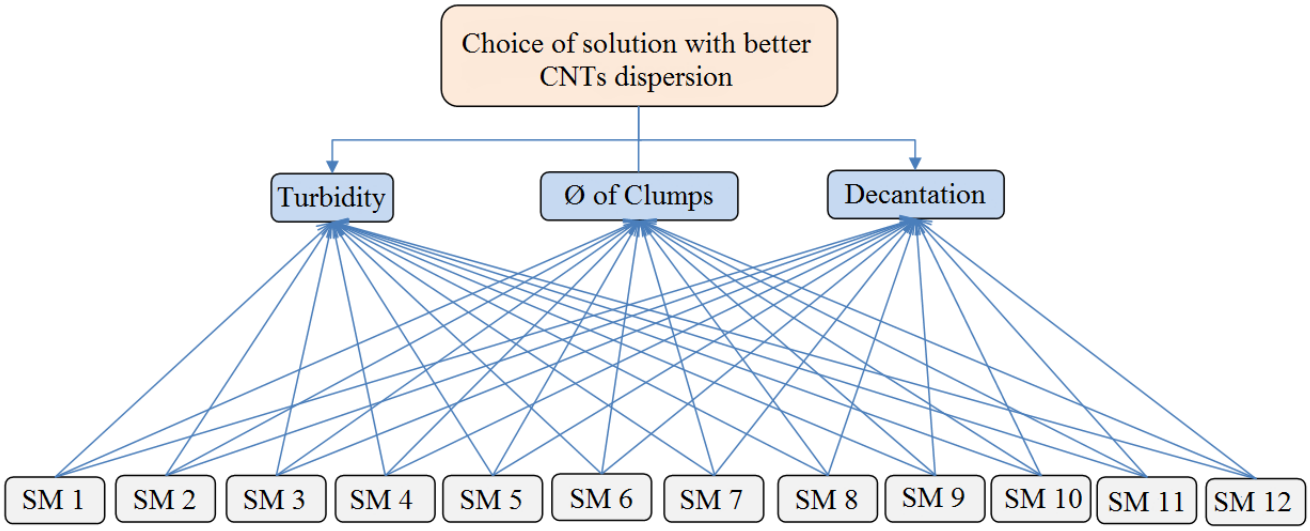

Figure 17. Flowchart of hierarchical analysis.

From the choice of this criteria, limits of performance were suggested that will be analyzed based on visual analysis and microscopy of CNT dispersions. The performance limits adopted can be seen in Table 7.

Table 7. Suggested limits for analysis of alternatives performances.

Criterion	Performance limits	Test method
Liquid turbidity	If blurred - optimum If translucent* – good If transparent** - bad	Microscope
Ø of clumps	From 0 to 500 µm – optimum From 500 to 1000 µm – good Higher than 1000 µm - bad	Microscope
Decantation	Did not decanted– optimum Decanted - bad	Visual - Test Tubes

** Lets few light pass by*
*** Lets much light pass by*

To estimate the importance of each criterion a matrix was developed, which can be seen in Table 8 and is contained in ASTM E 1765/2011 (2011). In the matrix, the attributes were compared by paired analysis (two by two), which aims to rank the criteria. A feature of AHP is the subjectivity of the process, since it depends of the importance that the evaluator gives to each criterion. Nevertheless, this aspect can be seen as a positive factor because it indicates that the evaluation system is open to the convictions of the decision maker, i.e., one can introduce prior experience from the expertise of the decision maker.
Regarding the use of the ASTM E 1765/2011 (2011) scale of importance, it should be clarified that when the comparison results in a reverse way to the cases of Table 8, the reverse of the note is adopted. That is, if B is more important than A, its note is 1/5.

Table 8. Scales of importance for the evaluated criteria (ASTM E 1765/2002).

Comparisons	Scale
A equal to **B**	1
A slightly more important than **B**	3
A more important than **B**	5
A much more important than **B**	7
A extremely more important than **B**	9

The next step was to mount a decision matrix and proceed to calculate the relative weight (Pr) of each considered criterion. For this, the sum of each individual criterion is considered, dividing it by the total sum of the criteria and multiplying by one hundred. Equation 1 illustrates this calculation.

$$\mathrm{Pr} = \frac{\sum Criterion(totalo\ frow)}{\sum Total(criteriacolumn)} \cdot 100 \quad (1)$$

Table 9. Matrix with paired analysis and weight for each criterion.

Evaluated criteria using the importance scale according to ASTM E 1765/2002	Turbidity of liquid	Ø of clumps	Decanting	Criteria – Sum (Line Total)	**Weight (Pr) - %**
Turbidity of liquid	1.00	3.00	3.00	7.00	53.9
Ø of clumps	0.33	1.00	0.33	1.66	12.8
Decanting	0.33	3.00	1.00	4.33	33.3
Total - criteria column				13.00	100%

From the measurement of weights for each criterion, the samples were classified according to their performance. For this purpose, three levels of performance classification where agreed as shown in Table 10.

Table 10. Standard for analysis of samples.

Performance limits	Points
Comply with high performance	2
Comply averagely	1
Comply underperforming	0

Thus, after sorting the samples according to their performance, each variable was divided by its greatest value as shown in Table 11. This practice has the function of normalizing all quantities measured so that all range from 0 to 1.

Table 11. Results of samples.

Scale of importance according with the analysis of CNTs dispersion	General data												Normalized data											
	SM 1	SM 2	SM 3	SM 4	SM 5	SM 6	SM 7	SM 8	SM 9	SM 10	SM 11	SM 12	SM 1	SM 2	SM 3	SM 4	SM 5	SM 6	SM 7	SM 8	SM 9	SM 10	SM 11	SM 12
Turbidity of liquid	1	0	0	2	2	2	2	0	2	2	0	0	0,5	0	0	1	1	1	1	0	1	1	0	0
Ø of formed clumps (µm)	1600	1350	1100	50	180	1180	350	850	420	620	700	600	0	0	0	1	0,3	0	0.1	0.1	0.1	0.1	0.1	0.1
Decanting	0	0	2	2	2	2	2	0	2	2	2	0	0	0	1	1	1	1	1	0	1	1	1	0

Finally, each variable was multiplied by its respective relative weight, obtaining the performance index to each alternative and criterion, as shown in Table 12. Adding the data of columns in Table 12 the general index of performance of each alternative is obtained. The performance index of the 12 samples can be seen at the penultimate row of Table 12. As a result, it appears that the best dispersions were SM 4 (1st place), SM 5 (2nd place), SM 7 (3rd place) and SM 9 (3rd place). It should be noted that SM 3 and SM 11 immersions were the ones with the best performance among those who used the addition of powder CNTs.

Table 12. Alternatives performance.

Scale of importance according to the analysis of CNTs dispersion	Variable weight	Normalized data x weight of variable											
		SM 1	SM 2	SM 3	SM 4	SM 5	SM 6	SM 7	SM 8	SM 9	SM 10	SM 11	SM 12
Turbidity of liquid	0.539	0.27	0.00	0.00	0.54	0.54	0.54	0.54	0.00	0.54	0.54	0.00	0,00
Ø of formed clumps (µm)	0.128	0.00	0.00	0.01	0.13	0.04	0.01	0.02	0.01	0.02	0.01	0.01	0,01
Decanting	0.333	0.00	0.00	0.33	0.33	0.33	0.33	0.33	0.00	0.33	0.33	0.33	0,00
Total		0.27	0.00	0.34	1.00	0.91	0.88	0.89	0.01	0.89	0.88	0.34	0.01
Classification		6	7	5	**1**	**2**	4	**3**	8	**3**	4	5	8

5. CONCLUSIONS

The highest value found corresponds to the best alternative of choice, so it can be said that in this case, SM 4, containing water and Aquacyl 0301 CNT, corresponds to the sample with the best dispersion. This demonstrates that the industrially dispersion method is really more efficient than all the other tested dispersion attempts in this study. According to the analysis, the samples that used Aquacyl product had the highest values of performance in the AHP, as can be seen in Table 12, the samples SM 4, SM 5, SM 6, SM 7, SM 9 and SM 10. Despite evidence of clumping in most samples with powder CNT, demonstrating that they were not fully dispersed in an aqueous medium, the study helped to understand the functioning of CNTs dispersion in various media, helping to define with a little more precision products and forms of dispersion to be used in the research. Samples with the best results with powder CNT were: SM 3 containing water, CNT and polycarboxylate additive (Tec Flow 8000 - at 1% relative to the mass of water) and SM 11 containing water, Arabic gum and CNT. It was demonstrated that the increase in sonication time of dispersion reduced the occurrence of decantation of the solutions, seen as an increasing factor for the dispersion of solutions. The study employing microscope was important because many findings based on the images obtained with this equipment revealed information that could not be obtained from observations with the naked eye. Notwithstanding, the worst dispersing results consisted in samples SM 8, with water, CNT and polycarboxylate additive (Tec Flow 8000 - at 0.5% relative to the mass of water) and SM 12 with water, powder CNT and surfactant (sodium lauryl ether sulphate), which were discarded. Comparing the results from SM 4 (Figure 9) with the ones of SM 5 (Figure 10), it was demonstrated that the introduction of polycarboxylate additive (Tec Flow 8000) caused the formation of clumps, initially non-existent, in liquid with CNTs industrially dispersed. One of the possible explanations is that electric bi polar charges, have accumulated on the surface of the particles causing the phenomenon of agglutination. This could be best explained if we knew exactly the dispersion process applied in the industrialized product. It is therefore suggested that further research be conducted to explain this fact.

6. ACKNOWLEDGMENTS

The authors thank the entire team of the Alconpat Journal. This paper was based in part on Marcondes dissertation (2012) developed the Program of Graduate Studies in Civil Engineering from the Federal University of Parana, Brazil.

7. REFERENCES

American Society for Testing and Materials. *Standard Specification for Chemical Admixtures for Concrete*. ASTM C494/C494M. In: Annual book of ASTM Standards, West Conshohocken, 2013.
American Society for Testing and Materials. *Standard Specification for Chemical Admixtures for Use in Producing Flowing Concrete*. ASTM C1017/C1017M. In: Annual book of ASTM Standards, West Conshohocken, 2007.
American Society for Testing and Materials. *Standard practice for applying analytical hierarchy process (AHP) to multi attribute decision analysis of investments related to buildings and buildings systems*. ASTM E 1765. In: Annual book of ASTM Standards, West Conshohocken, 2011.
Associação Brasileira de Normas Técnicas. *"Chemical additives for Portland cement concrete – Requirements", (Aditivos químicos para concreto de cimento Portland – Requisitos).* NBR 11768. Rio de Janeiro, 2011.

Batiston E. R. (2012), "*Carbon Nanotubes incorporation in Portland cement matrices"*, (*Incorporação de Nanotubos de Carbono em Matrizes de Cimento Portland)*. Tese (Doutorado em Engenharia Civil), Universidade Federal de Santa Catarina, Florianópolis.

Costa H. G., Correa P. S. (2010), *"Construction of an AHP-based model to catch criteria weights in port-occupancy evaluation"* International journal of the analytic hierarchy process; 2(1) 30-43.

Costa H. G. (2002), *"Introduction to hierarchical analysis method: multi-criteria analysis in the decision aid" (Introdução ao método de análise hierárquica: análise multicritério no auxílio à decisão)*, Niterói, R. J.

Couto, G. G. (2006), "*Nano nickel particles: synthesis, characterization, properties and study their use as catalysts in obtaining carbon nanotubes" (Nano partículas de níquel: síntese, caracterização, propriedades e estudo de sua utilização como catalisadores na obtenção de nano tubos de carbono),* Dissertação (Mestrado em Química) – Departamento de Química, Universidade Federal do Paraná, Curitiba.

Gleize P. J. P. (2007), *"Nanotechnology and construction materials"* (*Nanotecnologia e materiais de construção)*, In: ISAIA, Geraldo C. (Ed.). Materiais de construção civil e princípios de ciência e engenharia de materiais. São Paulo: IBRACON. v. 2. cap. 50, p. 1659-1685.

Ibarra Y. S., Gaitero J. J., Erkizia E., Campillo I. (2006), *"Atomic force microscopy and nanoindentation of cement pastes with nanotube dispersions",* Physica Status Solidi; 203(6) 1076–1081. doi: 10.1002/pssa.200566166

Koshio A., Yudasaka M., Zhang M., Lijima S. (2001), "*A Simple Way to Chemically React Single-Wall Carbon Nanotubes with Organic Materials Using Ultrasonicatio*n", Nano Letters; 1(7) 361-363. doi: 10.1021/nl0155431

Konsta-Gdoutos M. S., Zoi S. M., Surendra P. S. (2010), "*Highly dispersed carbon nanotube reinforced cement based materials",* Cement and Concrete Research; 40(7) 1052-1059. doi:10.1016/j.cemconres.2010.02.015

Lai Y., Wang W., Wang H. (2008), "*AHP and simulation-based budget determination procedure for public building construction projects. Automation in Construction",* 17(5) 623-632. doi: 10.1016/j.autcon.2007.10.007

Marcondes C. G. N. (2012), *"Addition of carbon nanotubes in concrete portland cement - absorption, permeability, chloride penetration and mechanical properties" (Adição de nanotubos de carbono em concretos de cimento portland – absorção, permeabilidade, penetração de cloretos e propriedades mecânicas*). Dissertação (Mestrado em Engenharia de Construção Civil) – Departamento de Construção Civil, Universidade Federal do Paraná, Curitiba.

Marchezetti A. L., Kaviski E., Braga M. C. B. (2011), *"Application of AHP method for ranking of alternative treatment of solid waste" (Aplicação do método de AHP para a hierarquização das alternativas de tratamento de resíduos sólidos domiciliares*). Ambiente Construído; 11(2) 173-187.

Mattana A. J, Medeiros M. H. F., Silva N. G, Costa M. R. M. M. C. (2012), "*Hierarchical analysis to choose between natural aggregate and sand rock crushing for making mortar coating" (Análise hierárquica para escolha entre agregado natural e areia de britagem de rocha para confecção de argamassas de revestimento*), Ambiente Construído; 12(4) 63-79. doi: 10.1590/S1678-86212012000400006

Makar J., Margeson J., Luh J. (2005), "*Carbon nanotube / cement composites – early results and potential applications",* in: International Conference on Construction Materials: Performance, Innovations and Structural Implications, 3, Vancouver; p. 1-10.

Metaxa Z. S., Seo J., Konsta-Gdoutos M. S., Hersam M. C., Shah S. P. (2012), "*Highly concentrated carbon nanotube admixture for nano-fiber reinforced cementitious materials".* Cement and Concrete Composites; 34(5) 612-617. doi: 10.1016/j.cemconcomp.2012.01.006

Mehta P. K., Monteiro P. (2013) "*Concrete Microstructure Properties and Materials*", New York: McGraw-Hill.

Neville A. M. (1996), "*Properties of Concrete",* John Wiley & Sons.
Nochaiya T., Chaipanich A. (2011), "*Behavior of multi-walled carbon nanotubes on the porosity and microstructure of cement-based materials",* Applied Surface Science; 257(6) 1941-1945. doi:10.1016/j.apsusc.2010.09.030
Pereira E., Medeiros M. H. F., Levy S. M. (2012) *"Concrete durability with recycled aggregates: an application hierarchical analysis" (Durabilidade de concretos com agregados reciclados: um aplicação de análise hierárquica),* Ambiente Construído; 12(3) 125-134. doi: 10.1590/S1678-86212012000300009
Sobolkina A., Mechtcherine V., Khavrus V., Maier D., Mende M., Ritschel M., Leonhardt A. (2012) "*Dispersion of carbon nanotubes and its influence on the mechanical properties of the cement marix",* Cement and Concrete Composites; 34(10) 1104-1113. doi: 10.1016/j.cemconcomp.2012.07.008.
Saaty T. L. (1978) "*Exploring the interface between hierarchies, multiple objectives and Fuzzy sets", Fuzzy Sets Systems"*; 1 57-68.
Zarbin A. J. G. (2007) *"Chemistry of nanomaterials" (Química de nano materiais),* Quim. Nova; 30(6) 1469-1479.

ALCONPAT Journal, Volume 6, Issue 2, may – august 2016, Pages 101 – 115

ALCONPAT Journal

www.revistaalconpat.org

eISSN 2007-6835

Journal of the Latin-American Association of Quality Control, Pathology and Recovery of Construction

Effect of the addition of nanosilica particles on the properties of two cementitious matrices

L. Y. Gómez-Zamorano[1], C. E. Castillo-Linton[1]

[1]Universidad Autónoma de Nuevo León, Facultad de Ingeniería Mecánica y Eléctrica, Programa Doctoral en Ingeniería de Materiales, Ave. Universidad s/n, Ciudad Universitaria, San Nicolás de los Garza, Nuevo León, México, CP 66450.

Article information
DOI:
http://dx.doi.org/10.21041/ra.v6i2.132
Article received on February 08th 2016, reviewed under publishing policies of ALCONPAT journal and accepted on March 10th 2016. Any discussion, including the replica of the authors, shall be published in the first number of the year 2017 as long as the information is received prior to the closing of the third number of the year 2016.

Legal Information

ALCONPAT Journal, Year 6, No. 2, May – August 2016, is a quarterly publication of the Latin American Association of Quality Control, Pathology and Construction Recovery, International, A.C., Km. 6, Old Highway to Progreso, Mérida, Yucatán, Zip Code 97310, Tel. +52 1 (999) 738-5893, alconpat.int@gmail.com, Website: www.alconpat.org Responsible Editor: Dr. Pedro Castro Borges. Responsible for the last update of this number, Informatics Unit ALCONPAT, Elizabeth Sabido Maldonado, Km. 6, Old Highway to Progreso, Mérida, Yucatán, Zip Code 97310, publication date: May 30, 2016.

ABSTRACT

This research focused on evaluating the effect of adding silica nanoparticles (NS) to two cementitious matrices, as ordinary portland and sulfoaluminate cement, in order to establish their influence on the mechanical and chemical properties. To conduct this evaluation, the NS were added in dosages of 0.30-to-5.0% by mass relative to cement. The results indicated that the compressive strength and resistance to chemical attack by sulfates were improved due to the addition of silica nanoparticles, in both matrices. Finally, the resistance to chemical attack by sulfates showed an improvement with the addition of silica nanoparticles when comparing with pure cement, suggesting an increase in the densification.
Keywords: reactivity; supplementary cementitious materials.

RESUMEN

Este trabajo de investigación evaluó el efecto de la adición de nanopartículas de sílice (NS) a dos matrices cementantes, base cemento portland ordinario y cemento sulfoaluminoso, con el fin de establecer su influencia en las propiedades mecánicas y de resistencia química de dichos materiales. Para esto, se adicionaron las NS en dosificaciones de 0.30% a 5.0% en peso. Los resultados indicaron que la resistencia a la compresión y al ataque químico por sulfatos, se ven mejoradas debido a la adición de NS. La resistencia al ataque químico por sulfatos se mejoró de forma importante con la presencia de NS en comparación al cemento sin adiciones. Este resultado sugiere que ambas matrices presentaron una mayor densificación.
Palabras claves: reactividad; materiales cementosos suplementarios.

RESUMO

Este estudo avaliou o efeito da adição de nanopartículas de sílica (NS) em duas matrizes cimentícias, base cimento Portland comum e cimento sulfoaluminoso, a fim de estabelecer a sua influência sobre as propriedades de resistência mecânica e química dos referidos materiais. Para isso, foram adicionadas as NS em dosagens de 0,30% a 5,0% em massa. Os resultados indicaram que a resistência à compressão e ao ataque químico por sulfatos são aumentadas devido à adição do NS. A resistência ao ataque químico por sulfatos melhorou significativamente com a presença de NS em comparação com o cimento sem adições. Este resultado sugere que ambas as matrizes apresentaram uma maior densificação.
Palavras-clave: reatividade; materiais cimentícios suplementares.

Corresponding author: Lauren Y. Gómez Zamorano (lauren.gomezzm@uanl.edu.mx)

1. INTRODUCTION

Among the recent research in the construction industry, it is possible to identify the use of nanomaterials, added to the cementitious matrix, which can modify the rheological properties of the concrete. Some of the most commonly used compounds are: nanosilica, photocatalytic nanocomposites as TiO_2, nano-$CaCO_3$ and nanoclays; the use of nanomaterials in the development of hybrid materials was also investigated, where the nanoparticles are not added, but formed in the cementitious matrix.

Other types of materials that have been tested, are carbon nanofibers, cellulose nanofibers, including the utilization of nanomaterials to modify the properties of the aggregates used in the manufacture of concrete. One of the most widely used nanomaterial is silica (silica nanoparticles, NS) due to its pozzolanic behavior. The results generally agree that when using this material, the mechanical properties are improved, as reported by (Sobolev et. al., 2009), who added 5-70 nm NS; they reported that, both compressive strength (RC) and the flexural strength, of mortars with an addition of 0.25% of nano-SiO_2 were improved in percentages of 16% at 24 hours and 18% at 28 h respectively. Other studies (Belkowitz et. al., 2010) have focused on the comparison of the properties obtained in the concrete when using microsilica particles and compared with NS (Mondal et. al. 2010, Shah et al, 2009), where the addition of up to 15% NS substantially improves the durability of concrete by increasing the rigidity of the CSH gel. These observations are also consistent with those reported when by (Hosseni et. al., 2010), where ferrocements mortars with 1-3% NS presented an improvement in the compressive strength and better densification in the interfacial transition zone, with a w/c ratios of 0.35 and 0.40. On the other hand, nanomaterials were studied to improve the performance of recycled aggregates (Hosseni et. al., 2009), where while the use of those nanoparticles improved the hydration reactions, the use of recycled aggregates generated lower strength and workabilities when using 1.5-3% of silica nanoparticles. Furthermore, the formation of a thin film of nanoparticles directly on the surface of the aggregates was studied (San Filippo et. al., 2009), the adhesion of aggregate and cement paste was improved, obtaining better mechanical properties. Additionally, they reported improvements up to 35% RC with an addition of 0.032% SiO_2.

As mentioned above, the use of nanotechnology in the construction industry can modify the properties of cement and/or concrete produced with these materials. However, a key point of several studies includes the process of the addition of nanoparticles and its proper dispersion in the matrix. As mentioned by (Sobolev et. al., 2009), the distribution of nano-SiO_2 in the cement paste plays an essential role on the performance of the cement and the products obtained. In other nanomaterials, such as carbon nanotubes, the problem of dispersion was also reported, (Shah et. al., 2009) and the biggest drawback of the incorporation of carbon nanotubes was the poor dispersion obtained.

It is worth notice that through this article a relevant contribution concerning the study of a sulfoaluminate cement with addition of NS is presented, since there is very little information related to this (Raki et. al., 2010, Jewell, 2015 Chung et. al., 2012). Additionally, the sulfates attack in both matrices with the NS additions is an interesting topic that has not been extensively studied.

2. EXPERIMENTAL PROCEDURE

Two cementitious matrices were used: (a) Ordinary Portland Cement CPO 40, according to Mexican standard NMX-C-414-ONNCCE-2010 and (b) Sulfoaluminate Cement (CSA) which main characteristic is that contains, in addition calcium sulfoaluminate (C_4A_3S), besides the traditional cement phases (C_3S, C_2S, C_3A and C_4AF). The results of chemical composition of both cements are presented in Table 1.

Table 1. Chemical composition of both types of cements.

Oxides (mass%)	SiO_2	Al_2O_3	Fe_2O_3	CaO	MgO	SO_3	Na_2O	K_2O	TiO_2	P_2O_5	Mn_2O_3	CaO	P.P.I	R.I.	A.T.
CPO 40	19.07	4.97	1.98	62.54	1.55	4.14	0.36	0.68	0.21	0.13	0.067	1.2	4	1.06	0.813
CSA	18.67	4.44	1.66	63.14	0.83	3.91	0.2	0.15	0.18	0.07	0.03	0.6	6.42	0.5	0.295

** P.P.I.: lost on ignition; R.I: insoluble residues; A.T.: Total alkalis.*

Table 1 shows that the content of SO_3 of both cements is in the range of 4.0%, i.e. 4.14% for CPO and 3.91% for the CSA. It is also noted that the CaO content is slightly higher in the CPO compared to the CSA cement (63.14% vs. 62.54%), indicating a higher content of limestone addition. Quantification of both cements phases was carried out using Rietveld refinement with HighScore Plus Software, version 3.05. Rietveld refinement results are presented in Figure 1 and Table 2. The results of the mineralogical quantification confirmed that both cements, have different contents of the main clinker phases, as C_3S, C_2S, C_3A. The analysis also showed the presence of $CaCO_3$ in both cements, although in the CSA cement was around 15% compared with 2.5% for the CPO. The main mineralogical differences were the presence of 15% Yelimite or C_4A_3S, identified only in the CSA cement. The nanosilica used was a commercial product and its characterization is presented in Table 3.

Table 2. Results of Rietveld quantification for the studied cements.

Component	Chemical formulae	CPO 40	CSA
C_3S- Alite, de la Torre et al	Ca_3SiO_5	61.9	36.4
C_2S - Belite	Ca_2SiO_4	18.9	27.3
C_3A- Cubic Aluminate	$Ca_9(Al_6O_{18})$	5.0	1.2
C_3A- Aluminate	$Ca_9(Al_6O_{18})$	----	1.8
Calcium Ferroaluminate	$Ca_2Fe_{1.52}Al_{0.48}O_5$	3.7	3.7
Yelimite	$Ca_3Al_6O_2CaSO_4$	----	1.5
Anhidrite	$CaSO_4$	0.8	3.2
Gypsum	$CaSO_4{\cdot}2H_2O$	7.2	5.5
Calcium Carbonate	$CaCO_3$	2.5	15.1
Calcium oxide	CaO	----	4.3
	GOF	8.6	11.2

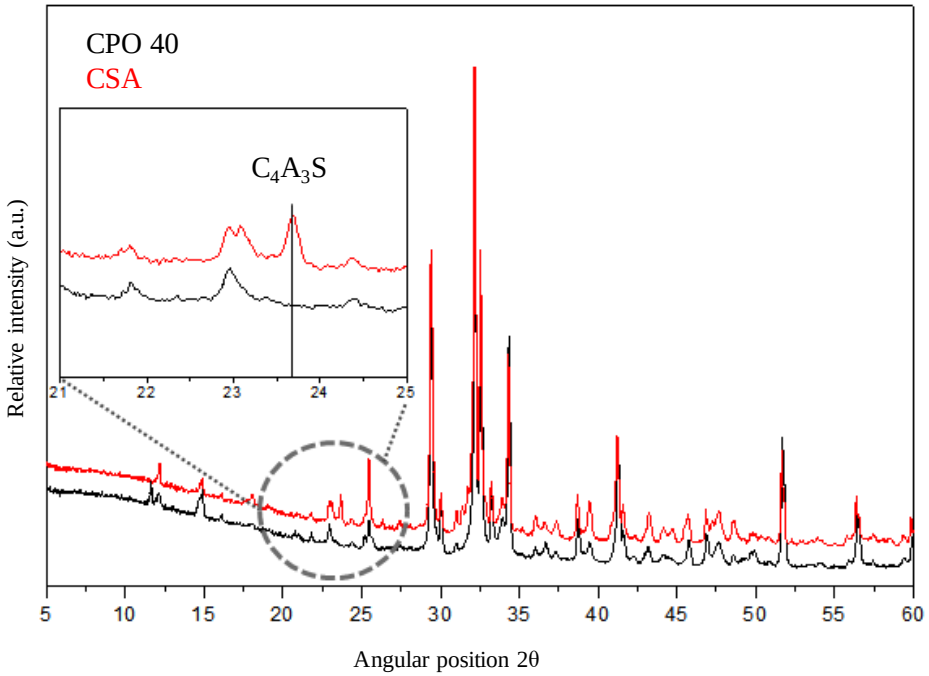

Figure 1. Comparison of diffraction patterns for both cements; In detail C_4A_3S phase observed in CSA

The NS were added in replacement levels of 0, 0.3, 1 and 5% by weight. It is noteworthy that even though for this type of materials the use of higher dosages than 1.0% could be unviable due to the costs, in the present investigation these levels were utilized to determine their influence on mortars properties. The mixing process used was similar to that indicated in the NMX-C-085-ONNCCE-2010 Mexican Standard, with a slight modification; mixing water was added first, then SP, and mix for 60s prior to adding NS and mix again for 1 minute; afterwards the process was carried out as indicated by the standard. It was necessary to use 0.5% SP, to ensure dispersion of the NS. After 24 h, the specimens were demolded and placed in a saturated calcium hydroxide (to avoid leaching) for the different curing periods.

The samples were characterized by compressive strength (RC); subsequently solid fractions of the samples were immersed in acetone and vacuum dried at 50°C for 24 h, to stop the hydration reactions and be analyzed by scanning electron microscopy (SEM). Also, the samples were characterized by isothermal conduction calorimetry.

Table 3. Characterization of the nanosilica

Characteristic	Specification	Result
Presentation	Liquid	Liquid
Color	Semi-Transparent white	Semi-Transparent white
Specific gravity, 20°C	1.134±0.03	1.22
Viscosity, 20°C, Brookfield, Sp 00/100 rpm	< 30 cps	ND
pH	10±1	10.3
Solid %	----------	32.5

**Where ND = Not determined*

3. RESULTS

4.1 Isothermal calorimetry

Isothermal calorimetry tests were carried out in pastes for both type of cements; the results are shown in Table 4. To evaluate the effect on the heat generated during the hydration reactions, samples were prepared with 0.50% SP and 1.0 and 5.0% NS. The pastes were had a water/cement (w/c) ratio of 0.40 and 0.50 (see Table 4).

Table 4. Samples prepared for characterization with isothermal calorimetry, cements were prepared with NS and SP.

Sample	1	2	3	4	5	6	7	8
Type of cement	CPO 40	CPO 40	CSA	CSA	CPO 40	CPO 40	CSA	CSA
NS (mass%)	---	---	---	---	1	5	1	5
SP (mass%)	0.5	0.5	0.5	0.5	0.5	0.5	0.5	0.5
w/c ratio	0.5	0.4	0.5	0.4	0.5	0.4	0.5	0.4

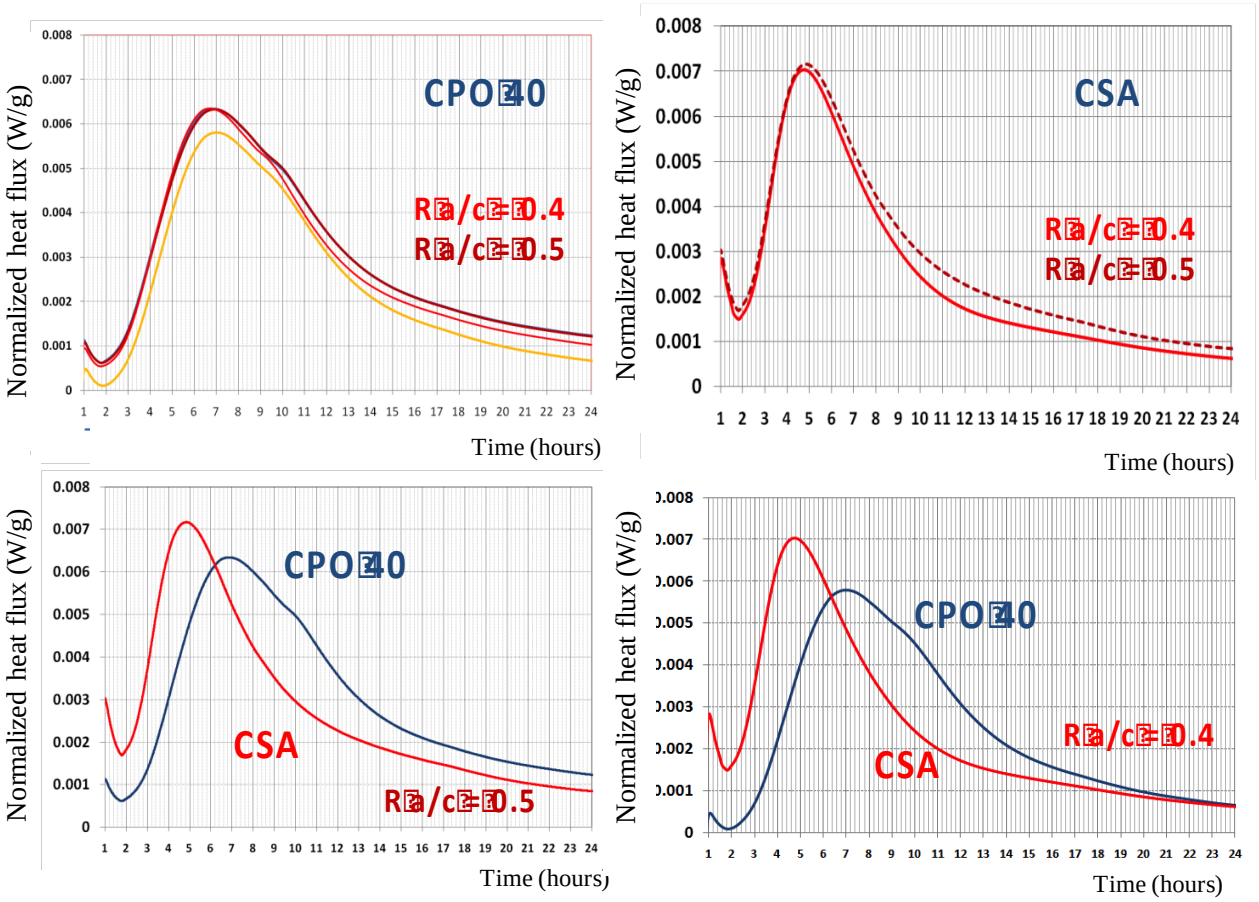

Figure 2. Isothermal calorimetry curves for both cements at different w/c ratios.

Figure 2 shows that the induction period ended after 2.0 hours for the CPO 40, while for CSA, finished before. It is at this time, when the setting period starts and the C-S-H layer breaks, with the continuation of the hydration process. Results shows that lower w/c ratios slightly accelerate the hydration reaction; this effect is more noticeable for CPO 40.

As shown in Figure 2, when adding 5% SP for both type of cements, a shift of the exothermic curve was observed, indicating an extended sleeping period, causing the curve became more pronounced with a lower crest, having a maximum heat release at 15 h for CPO 40 with 0.5% SP, compared to 7 h without SP, i.e. the addition of 0.5% SP increases the starting time for the development of RC two times. A similar behavior is shown for CSA; where the effect of SP appears to be slightly higher, since cement without SP registers its exothermic maximum at 4.7 h, whereas with the addition of 0.5% SP, the exothermic maximum is observed at 13h, i.e., almost three times slower than the plain cement.

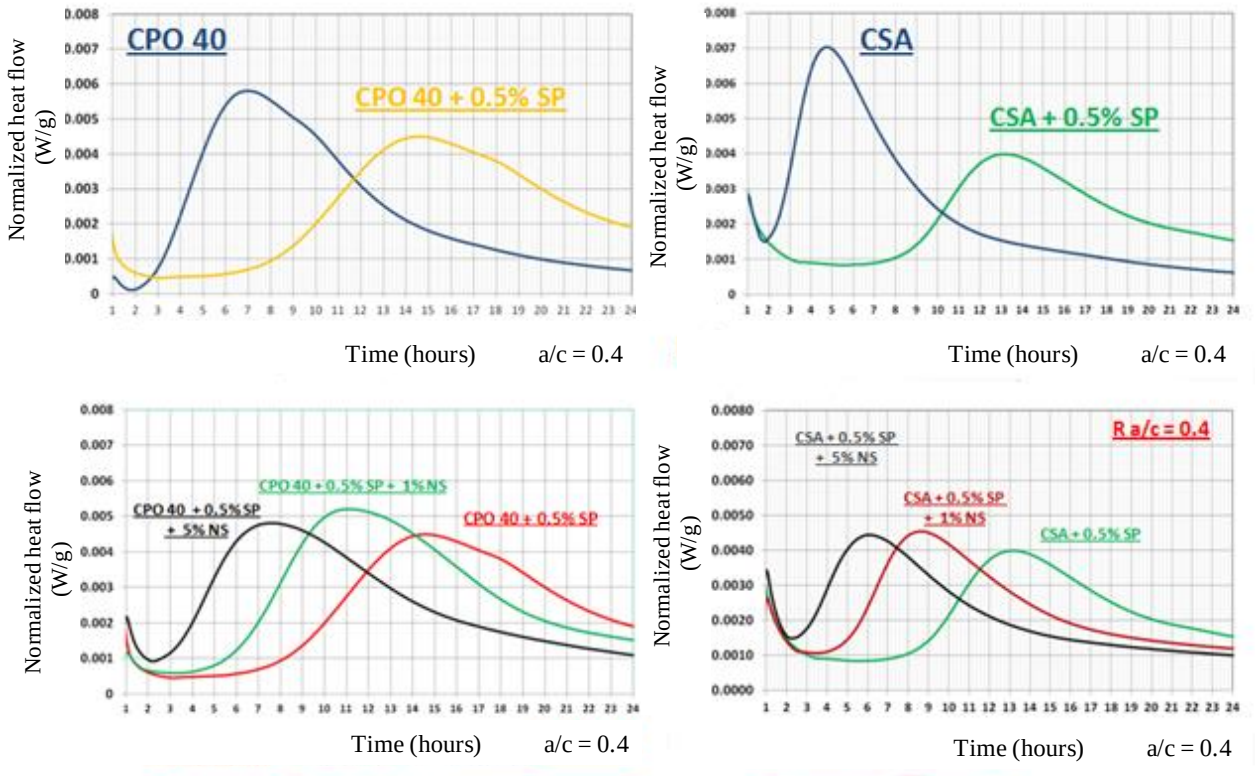

Figure 3. Isothermal calorimetry curves for the cements with NS and SP; w/c = 0.40.

On the other hand, at the same w/c ratio, it is observed that the CSA presents a different heat evolution curve compared with CPO 40, where the main peak due to the exothermic reaction of C_3S was at 6.5 h for CPO 40, and 4.5 h for CSA. Additionally, the exothermic peak reached a maximum heat flux for CSA of 0.07 W/g, while for the CPO 40 of 0.06 W/g. This indicates that the hydration reaction of cement CSA starts faster, and the initial RC should be greater in CSA; however, the RC values were higher at 24 hours for CPO 40 (18 MPa) compared to CSA (13.1MPa). This could be due to the dilution effect of CSA, which according to the results of the chemical composition, contains a higher content of limestone, compared with CPO 40. The results also show a shorter setting period of CSA with respect to CPO 40. After the pure cements analysis, the effect of NS addition was studied.

These results confirm those reported by Puertas (Puertas et. al., 2001 and Puertas et. al., 2005), indicating that regardless of the nature of the SP added, the hydration reactions of calcium silicates were delayed, extending the setting period. This effect can be explained due to an adsorption of the polymer in the cement grains, forming a layer barrier around grains, and preventing the transport of water molecules to the cement particles, in addition to the formation of complexes between Ca^{2+} ions formed in the initial hydration and the anions of the polymers that affect nucleation and precipitation of $Ca(OH)_2$. However, the RC of mortars with SP indicated that at 24 h, the RC of pure CPO 40 was lower than those containing 0.5% SP, i.e., 18 MPa and 23.5 MPa respectively.

The isothermal calorimetry results indicated a significant extension of the initial setting time, however, this result does not necessarily imply any relation with the RC expected by these cements, since the setting process and the development of strength process are independent. It is noteworthy that that for CS, the effect was different, and the addition of SP decreased the RC at 24 hours, from 13.1 to 8.2 MPa.

Figure 3 also showed that by adding the nanoparticles to the same w/c ratio the evolution heat curves shifted to shorter times, suggesting that the processes of setting and hydration reactions were accelerated by the addition of the silica nanoparticles. This trend was observed for both types of cements.

This behavior confirms that reported by (Qing et. al., 2007), they observed that with the increase in the percentage of NS, the workability decreased, and the hydration process was accelerated compared to other pozzolanic materials such as silica fume. Other authors (Björnström et. al., 2004, Morteza et. al., 2014 and Li et. al., 2004) found that nanosilica also accelerates the process of hydration and C-S-H gel formation due to its particle size; moreover, with the increase of the addition percentage of NS, the heat of hydration of the mixture incremented.

Hence, it is possible also to observe that at higher NS load, the exothermic maximum is reached at lower time. According to curves for CPO 40, form 0 to 1.0% NS, the time at which the maximum was reached moved from 14.5 h to 11 h, and by adding 5% NS time fell from 11 to 7.5 h. For the CSA, the behavior was similar, i.e., with no additions the maximum was observed at 13.3 h, with 1% NS at 8.8 h and for 5% NS at 6 h.

This experimentally observed behavior had a parabolic shape and can be explained through the following equation:

$$\mathbf{f(x)=ax^2+bx+c} \quad (1)$$

where: f (x) = maximum time of heat release, x = % of nanoparticles; a, b and c are coefficients of each of the systems.

Equation for the system with CPO 40:

$$TTMáx = 0.525(\%NS)^2 - 4.025(\%NS) + 14.5 \quad (2)$$

Equation for the system with CSA:

$$TTMáx = 0.76(\%NS)^2 - 5.26(\%NS) + 13.3 \quad (3)$$

From figure 4 it can be concluded that, while adding nanoparticles to the cementitious matrix accelerates hydration reactions and therefore increase RC, there is a point where the increase in the nanoparticles content will not have an improvement effect in the cement. In Figure 4 it can also be noted that higher that 3.5% contents of NS, the time where the exothermic maximum is reached, increase again. This would confirm that the nanoparticles presence, accelerated the development of the initial RC, but only up to this content.

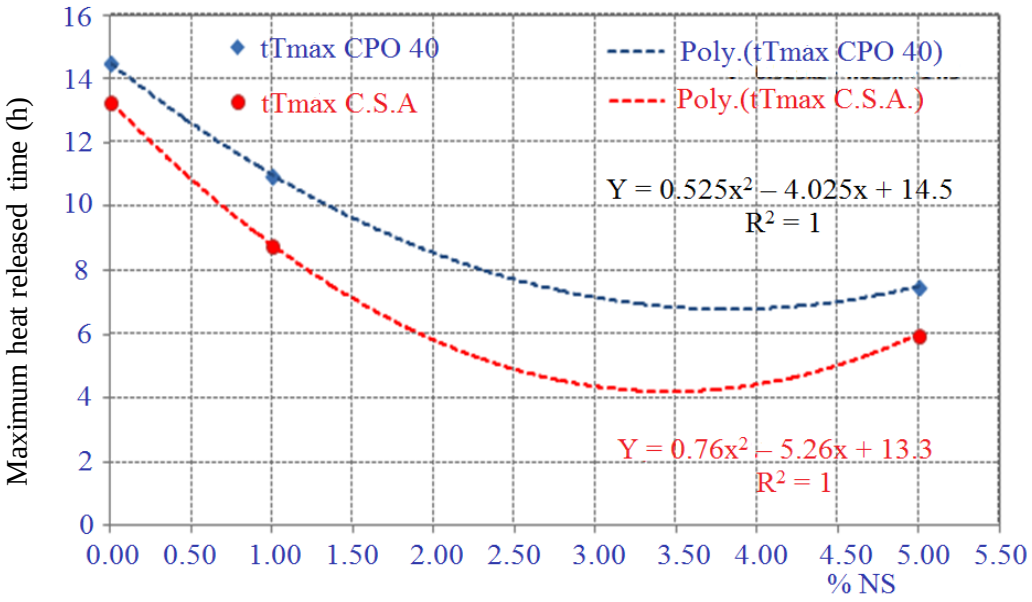

Figure 4. Maximum heat release time vs % NS.

4.2. Compressive strength results.

Samples with 0.5%SP and 0.3%, 1% and 5% NS were used to estimate the compressive strength. The results of 24 h, 3, 7, 28, 90 and 150 days are presented in Figure 5. It is worth to notice that, for this first set of results, the water added to the mix was corrected considering the water supplied by NS (which was provided in suspension), in order to keep the ratio w/c of 0.485 constant.

From the results, it can be observed that for the CPO 40, the best RC was obtained for the mixture with SP. The RC results also showed that all the systems with NS tested at 24h exceed the results obtained by reference (neat CPO 40), with an increase up to 43% (25.8 MPa vs 18 MPa), for sample with 5% NS. After 3 days of hydration, these percentages decreased, observing an increase of 15% of for mixtures with 5% NS (40 MPa vs 34.9 MPa). At 7 days, the improvement was of 11% for CPO + SP while, with the incorporation of 5%NS the RC was 8% higher than that obtained by the reference. At 28 days, the samples with SP developed a RC 17% RC higher that the reference (54.9 vs. 47.1 MPa), while the increase for samples with NS was around 11% compared to the reference (52.1 and 52.3 MPa for samples with 0.3% and 5% NS vs 47.1 MPa for the reference). After 150 days of curing, all samples with NS reaching almost the same value as obtained by reference and only the sample with SP developed a 18% greater 34.9 MPa than the neat CPO.

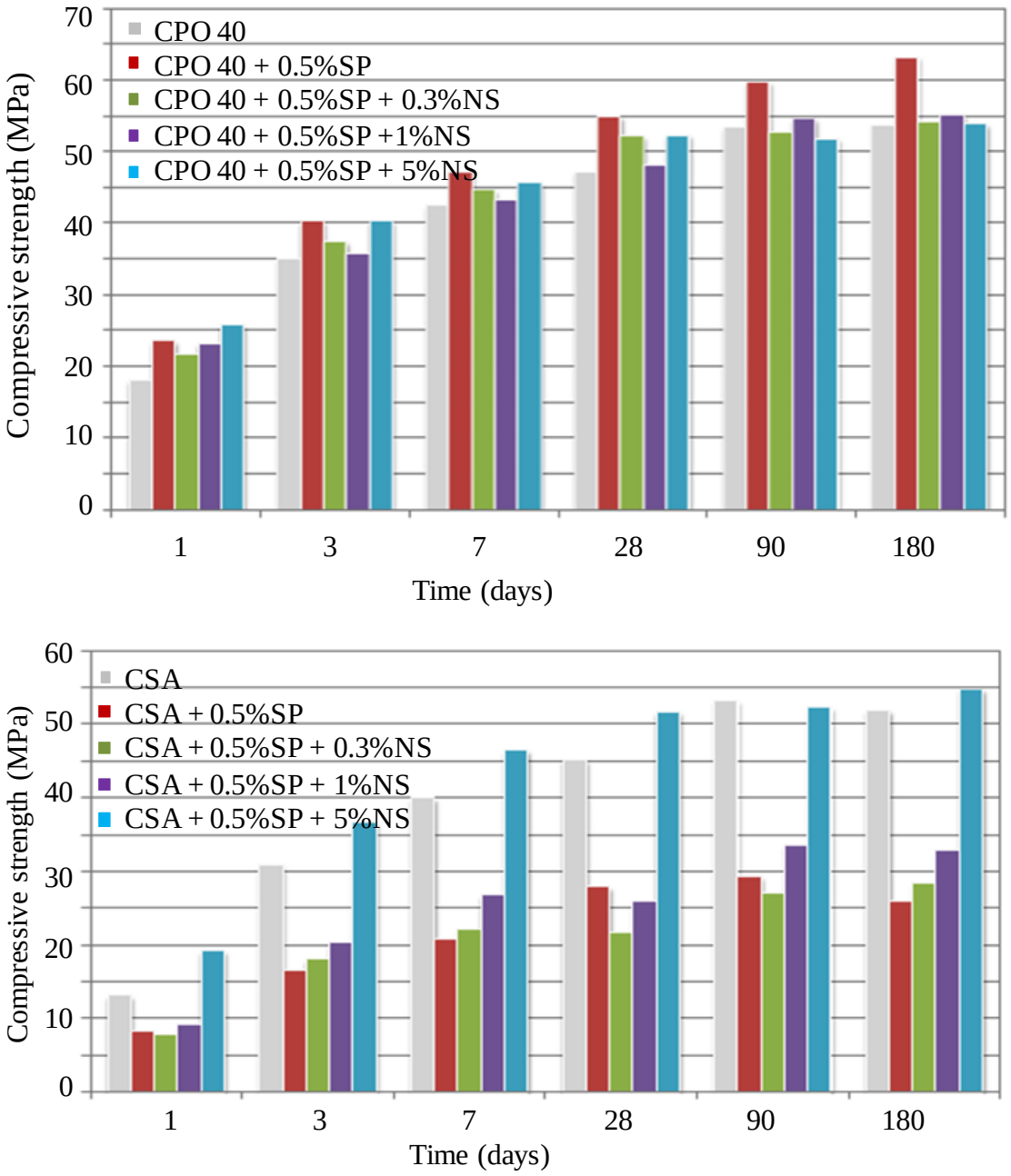

Figure 5. Compressive strengths results of the CPO 40 and CSA, without adjusting the amount of water.

The effect shown for CSA, was different as that observed for CPO 40, since the addition of SP, did not favor the development of RC, but rather inhibited the hydration processes. Therefore, all the RC results for the mixtures containing 0.5% SP, showed lower RC with respect to the reference, as 63%, 54%, 52%, 62% and 55% at 24 h, 3, 7, 28, 90 and 150 days respectively due to the decrease in the aforementioned reactivity, since SP are designed for ordinary Portland cement and the sulfate phases contained in the CSA may negatively affect the functionality of the SP.

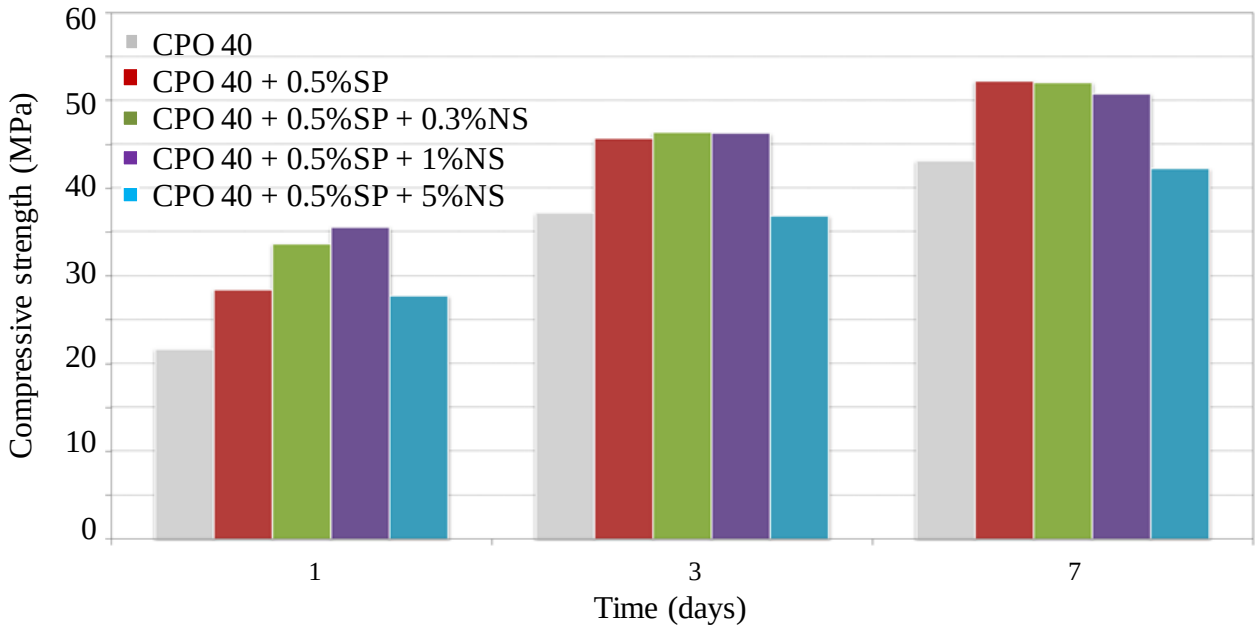

Figure 6. Compressive strength results for the CPO 40 for a constant flow.

This behavior was observed for CSA cement in all samples, except for the mixture with 5% NS, where it possible to observe an increase in the RC of about 47% at 24h, 19% at 3 days, 16% at 7 days, and 14% after 28 days. According to (Ma et. Al., 2014) when adding SP, the RC for belite-sulfoaluminate cementsat 24 h decreased, however, at 28 days RC were equivalent to the reference and even higher when dosed in percentage of 0.075%. This was to the delay in the ettringite formation after 1 day of hydration, especially at high concentrations, resulting in a poor RC. This could explain that the 0.5% CSA load used in this research could be relatively high for the nature of this cement.

As can be seen in Figure 6, at similar values of fluidity, by adjusting the mixing water for the same fluidity; RC results for CPO 40 with NS change with respect to those previously described, although the best results are observed in presence of SP, the results with the NS are very similar, and even superior at 24 h for samples with 0.3% and 1% NS.

These results are relevant because it raises a question relative with the Mexican standard specifications of consumption of water to use when it comes to assessing ordinary cements. As is known, the standard indicates that for an ordinary Portland cement, the w/c ratio recommended to evaluate RC is 0.485. The results obtained in this research suggest that for systems with SP systems, or nanoparticles, it is best to seek the fluidity and water required to adjust to this fluidity and do not use a fixed w/c ratio.

4.3. Chemical resistance to sulfate attack

The sulfate attack tests were carried out according to the procedure specified in ASTM-C-1012. Figures 7 and 8 show the results for each type of cement measured during 550 days, include the standard sets a minimum duration of 12 months. From the results, it is possible to observe that neat CPO 40 and CSA do not have good resistance to chemical attack by sulfates, since the change in length exceeds the allowable expansion value of NMX-C-414-ONNCE-2010 standard of 0.1% at 125 days for CPO 40 and at 50 days for CSA.

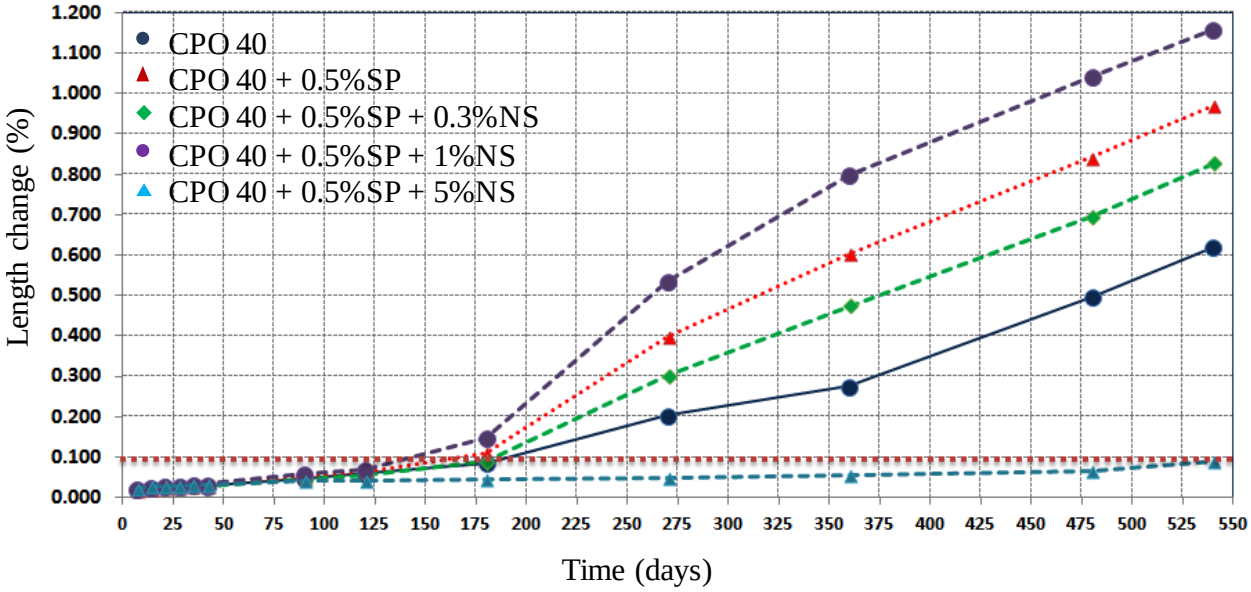

Figure 7. Sulfate attack chemical resistance of CPO 40 after 550 days of exposition.

The addition of nanoparticles in percentages of 5%, promotes the chemical resistance to sulfates, for both types of cement. In the case of CPO 40, the benefit of adding nanoparticles is so favorable that the cement changes from a cement without resistance to sulfate attack ("RS" in the nomenclature used in the Mexican standard NMX-C-414- 2010-ONNCCE) to be a resistant to sulfates at least up to 550 days, with contents of 0.5% of SP and 5% NS. The addition of less than 5%NS did not improve the resistance.

For the CSA, the addition of nanoparticles showed a lower resistance to chemical attack by sulfates compared to CPO 40, since CSA without additions exceeded the limit established by NMX-C-414-2010-ONNCCE standard after only two months of exposure. However, by adding SP and NS, cement remained with characteristics of resistance to chemical attack up to 275 days (9 months). This change was 94.8% for 180 days, which was the maximum age at which the reference specimen cement volume remained stable with respect to neat CSA.

According with the results observed for CPO 40 the addition of both SP and NS, in low dosages for the latter was not beneficial in terms of resistance to chemical attack, however, with all the additions, the CSA resistance was improved compared with pure CSA.

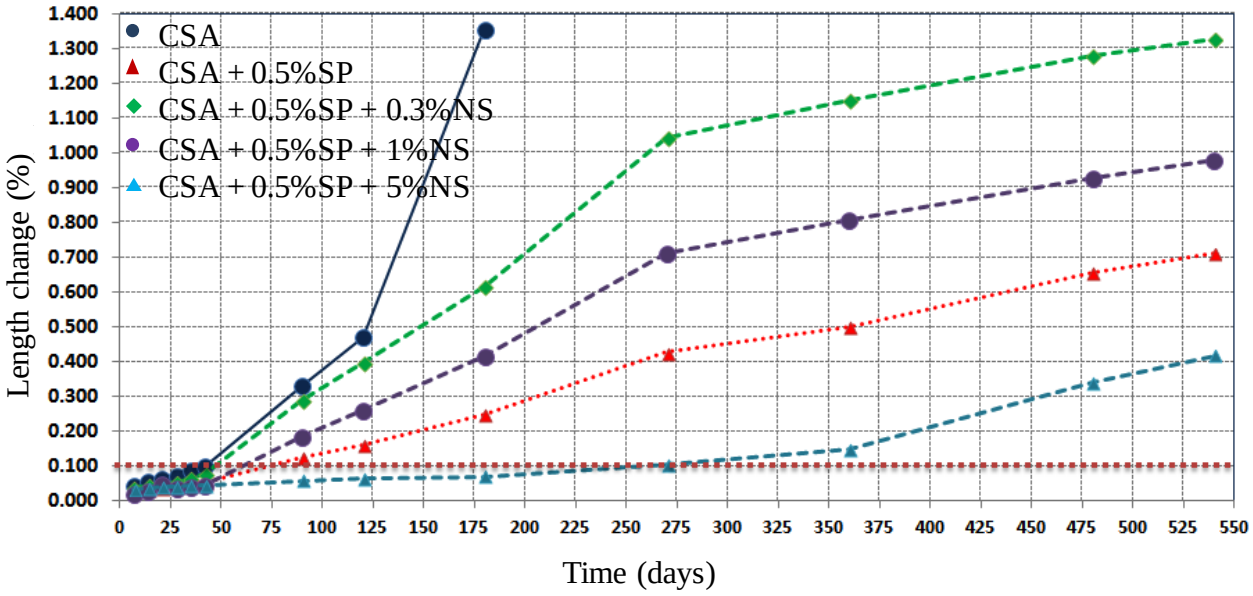

Figure 8. Sulfate attack chemical resistance of CSA after 550 days of exposition.

As mentioned above, this behavior can be explained by a densification of the matrix, which increased with the content of NS, and thus a reduction in porosity and sulfate attack tends to be slower than in cement samples without NS. The NS would be acting as nucleation sites for the generation of gel C-S-H and to promote reduction in porosity. This behavior was confirmed by other investigators (Quercia et. al., 2012 and Li et. al., 2004), they reported that the addition of NA increased RC and decreases permeability through the pozzolanic reaction, resulting in an increased denser structure with a further formation of C-S-H. According to (Khater et. Al., 2006), with the use of modified montmorillonites, the permeability was 100 times reduced compared to neat cement.
Thus, durability of the cements could be modified and improved with the presence of NS, due to the filler effect of these nanoparticles, densifying the matrix and decreasing the porosity and permeability, this in turn increases the RC, as for microsilica.

4. CONCLUSIONS

- Lower w/c ratios accelerated the hydration reactions and this effect was more pronounced for the CPO 40 for the CSA.
- The CSA reacted faster than CPO 40, and consequently higher initial compressive strength.
- Adding SP retarded hydration reactions of cement and its effect was reversed when using NS.
- Following from that, NS accelerated the hydration reactions, up to a limit, otherwise this effect was reverted. In this study the optimal acceleration was observed at 3.5% NS.
- SP addition substantially improved the compressive strength of CPO 40, for the case of the CSA, the behavior was the opposite, with the addition of SP, cement developed only 50% of the compressive strength achieved by the reference, except when using 5% NS, where the results were superior compared with those obtained for pure CSA. These results were obtained at a w/c constant ratio.
- With constant fluidity, the results indicated hat with 1% NS the compressive strength was improved up to about 60% compared to cements without additions; due to an acceleration effect acting as nucleation sites and also its pozzolanic behavior, which was more pronounced at early ages, as observed in the calorimetry results.

- In general, it was found that adding NS in both cements, the sulfate attack was not as pronounced as compared to samples without any additions.
- For the case of CPO 40 this addition gives the concrete the characteristic of resistance to chemical attack by sulfates, when originally it is an ordinary Portland cement; increasing its added value. However, lower than 5%NS contents do not offer advantages in in this chemical resistance.
- For the CSA, the presence of NS reduced the sulfate attack up to 95% compared to neat CSA. This is relevant because the CSA without adding any additional material exceeded the limit established by the Mexican Standard for sulfate resistant cement only after two months of exposure.

5. ACKNOWLEDGEMENTS

Financial support from CONACYT and CEMEX for the realization of this project is widely appreciated.

6. REFERENCES

ASTM C1012/C1012M – 15, *Standard Test Method for Length Change of Hydraulic-Cement Mortars Exposed to a Sulfate Solution*.

Belkowit J. S., Armentrout D. (2010) "*An investigation of Nano Silica in the Cement Hydration Process*", Proceeding 2010 Concrete Sustainability Conference, National Ready Mixed Concrete Association, U.S.A., pp. 1-15

Björnström J., Martinelli J., Matic A., Borjesson L., Panas I. (2004), "*Accelerating effects of colloidal nano-Silica for beneficial calcium-silicate-hydrate formation in cement*", Chemistry Physic Letters; 392, pp. 242-248

Chung D. L. (2012) "*Carbon materials for structural self-sensing, electromagnetic shielding and thermal interfacing*", Elsevier, CARBON 50, pp. 3342-3353

Hosseni P., Booshehrian A., Delkash M., Ghavami S., Zanjani M. K. (2009), *"Use of Nano-SiO2 to Improve Microstructure and Compressive Strength of Recycled Aggregate Concretes",* Nanotechnology in Construction 3, pp 215-221

Hosseni P., Booshehrian A., Farshchi S. (2010), "*Influence of Nano-SiO2 addition on Microstructure and mechanical Properties of Cement Mortars for Ferrocement*", Transportation Research Record; Journal of the transportation Research Board No. 2141, pp. 15-20

Jewell R. B. (2015) "*Influence of Calcium Sulfoaluminate Cement on the Pullout Performance of Reinforcing Fibers: An Evaluation of the Micro-Mechanical Behavior*", PhD Thesis, Civil Engineering, University of Kentuky.

Li H., Xiao H., Yuan J., Ou J. (2004) "*Microstructure of cement mortar with nano-particles*", Composites Part B: Engineering, 35, pp. 185-189

Ma B., Ma M., Shen X., Li X., Wu X. (2014), "*Compatibility between a polycarboxylate superplasticizer and the belite-rich sulfoaluminate cement: Setting time and the hydration properties*", Construction and Building Materials, 51, pp. 47-54

Mondal P., Shah S. P., Marks L. D., Gaitero J. J. (2010), "*Comparative Study of the effect of Microsilica and Nanosilica in concrete*", Transportation Research Record; Journal of the transportation Research Board No. 2141, pp. 6-9

Morteza B., Baghbadrani M., Aslani F. (2014), "*Performance of nano-Silica modified high strength concrete at elevated temperatures*", Construction and Building Materials, 68, pp. 402-408

Norma NMX-C-085-ONNCCE-2010, *Industria de la construcción - Cementos hidráulicos - Determinación estándar para el mezclado de pastas y morteros de cementantes hidráulicos*

Norma NMX-C-414-ONNCCE-2010, *Industria de la construcción-Cementantes- Especificaciones y método de ensayo*.

Puertas F., Vázquez T. (2001), "*Hidratación inicial del cemento. Efecto de aditivos superplastificantes*", Materiales de Construcción 51(262), pp 53-61.

Puertas F., Santos H., Palacios M., Martínez S. (2005), "*Polycarboxylate superplaticizer admixtures: effect on hydration, microestructure and rheological behavior in cement pastes*", Advances in Cement Research, 17, pp. 77-89

Qing Y., Zenan Z., Deyu K., Rongshen C. (2007), "*Influence of nano-SiO_2 addition on properties of hardened cement paste as compared with silica fume*", Construction and Building Materials 21(3), pp. 539–545

Quercia G., Zpuesz P., Hüsken G., Brouwers J. (2012), "*Effects of Amorphous Nano-Silica additions on Mechanical and Durability Performance of SCC Mixtures*", Proceedings of the International Congress on Durability of Concrete (ICDC 2012), 18-21 June, Trondheim, Norway, pp. A2-A4

Raki L., Beaudoin J., Alizadeh R., Makar J. Sato T. (2010), "*Cement and Concrete Nanoscience and Nanotechnology*", Materials, **3**(2), 918-942

San Filippo J. M., Muñoz J. F., Isabel Tejedor M., Anderson M. A., Cramer S. M. (2009), "*Nanotechnology to Manipulate the aggregate-Cement Paste Bond Effects on Mortar Performance*", Nanotechnology in Construction 3, pp. 29-33

Shah S. P., Konsta-Gdoutos M. S., Metaxa Z. S., Mondal P. (2009), "*Nanoscale Modification of Cementitious Materials*", Nanotechnology in Construction 3, Proceedings of the NICOM3, pp. 125-130

Sobolev K., Flores I., Torres-Martinez L. M., Valdez P. L., Zarazua E., Cuellar E. L. (2009) "*Engineering of SiO_2 Nanoparticles for Optimal Performance in Nano Cement-Based Materials*"; Proceedings of the Nanotechnology in Construction 3 (NICOM3) 01/2009; pp. 139-148.

ALCONPAT Journal, Volume 6, Issue 2, may – august 2016, Pages 116 – 128

ALCONPAT Journal

www.revistaalconpat.org

eISSN 2007-6835

Journal of the Latin-American Association of Quality Control, Pathology and Recovery of Construction

Evaluation of the adherence of ceramic tiles applied as facade lining

P. Valentini[1], C. S. Kazmierczak[2].

[1] Civil Engineering Course, Universidade do Vale do Rio dos Sinos (UNISINOS), Brazil.
[2] Civil Engineering Postgraduate Program, Universidade do Vale do Rio dos Sinos (UNISINOS), Brazil.

Article information
DOI:
http://dx.doi.org/10.21041/ra.v6i2.133
Article received on September 04th 2015, reviewed under publishing policies of ALCONPAT journal and accepted on December 02th 2015. Any discussion, including the replica of the authors, shall be published in the first number of the year 2017 as long as the information is received prior to the closing of the third number of the year 2016.

ABSTRACT

The most serious pathology in ceramic tile is detachment because of the risk of accidents due to fall and the cost of repair. This research aims to evaluate the influence of ceramic plates applied with two types of adhesive mortar subjected to three different curing conditions (established by the ABNT 14081-4:2012) on the adhesion to the coating system. It was observed that cure is the variable with higher influence on the adhesive strength, followed by the type of adhesive mortar, while the water absorption of ceramic plate has a little influence on the results.

Keywords: adherence; ceramic tiles; adhesive mortar.

RESUMEN

Dentro de las manifestaciones patológicas que pueden ocurrir en azulejos de cerámica se encuentra la pérdida de adherencia considerada la más seria debido a los riesgos de accidentes por el efecto de las caídas y el costo de la reparación. Este trabajo tiene como objetivo evaluar la influencia de las propiedades de diferentes placas de cerámica aplicadas con dos tipos de mortero de pega y sometidos a tres diferentes condiciones de curado (establecidas por la norma ABNT 14.081-4:2012) en la resistencia de adherencia del sistema de revestimiento. Se observó que el tipo de curado es la variable que presenta la influencia más significativa en la resistencia de adherencia, seguida por el tipo de mortero de pega, ya que el azulejo de cerámica ejerce poca influencia una vez hecho un análisis global de los resultados.

Palabras Clave: adherencia; azulejo de cerámica; mortero de pega.

RESUMO

Dentre as manifestações patológicas que podem ocorrer em revestimentos cerâmicos os descolamentos são considerados as mais sérias, devido aos riscos de acidentes em decorrência da queda de placas e por seu custo de reparo. Este trabalho tem como objetivo avaliar a influência das propriedades de diferentes placas cerâmicas aplicadas com dois tipos de argamassa colante e submetidas a três diferentes condições de cura (estabelecidas pela norma ABNT 14.081-4:2012) na resistência de aderência do sistema de revestimento. Observou-se que o tipo de cura é a variável que apresenta influência mais significativa na resistência de aderência, seguida pelo tipo de argamassa colante, enquanto a placa cerâmica exerce pouca influência em uma análise global dos resultados.

Palavras-chave: aderência; revestimento cerâmico; argamassa colante.

Corresponding author: Claudio S. Kazmierczak (claudiok@unisinos.br)

1. INTRODUCTION

Among the pathological problems that could occur in ceramic lining, the ones that stand out are: the detachment of the tiles, splitting or cracking, efflorescence, and the deterioration of the joints (Campante and Baía, 2008). Among these, the detachment of the ceramic tiles is considered the most serious due to the risk of accidents as consequence of the tile or parts of it falling, as well as the repair costs this could entail (Campante and Baía, 2008; Mansur, 2007).

A main characteristic of the detachments or separations is the loss of adherence of the ceramic tiles with the substrate or the mortar, which occur when the tensions of the ceramic lining exceed the adherence capacity of the connections of these layers (Barros and Sabatini, 2001). External factors such as thermal shock, directed rain, solar radiation, and humidity are the ones that exercise the greatest influence in the degradation of the facade lining system (Antunes, 2010).

Temperature variation is an expressive degradation agent of the ceramic facade linings (Consoli, 2006). The thermal variation in single day in the city of Porto Alegre – RS, for example, can be rather high, generating a temperature gradient of up to 50°C on the surface of the facade. In an investigation looking to evaluate the durability of ceramic lining systems, carried out with ceramics and mortars adhered in concrete substrates through the induction of tensions of a thermal nature (Chew, 1992), determined a 20% reduction in the resistance of traction adherence of the ceramics when compared with systems that did not go through the action of the cycles.

Another significant degradation agent of the facades is humidity, which is characterized by the existence of water in the materials in a liquid, solid, or gas form (Ribeiro, 2006). The hygroscopic movement is a significant cause for the detachment of ceramic tiles (Bauer, 1995; Ribeiro, 2006). In order to limit the hygroscopic movements in ceramic facade linings, it is recommended to use low water absorption ceramic tiles (Goldberg, 1998). With this in mind, the British standard BS 5385-2 (BSI, 2015) specifies, both for extruded and pressed ceramic tiles, the use of tiles for facades with a water absorption below 3%. In this respect, the Brazilian standard NBR 13.818 (ABNT, 1997) does not provide a specific limit. In tests carried out on ceramic tiles in three different humidity conditions: air dried, with 0.2% humidity; slowly brushed with water, resulting in a 2.0% humidity; and submerged in water for a period of 30 seconds, with the tiles being kept in a vertical position before settlement in order to drain excess water, resulting in 8.5% humidity. It was verified that the greatest adherence between the ceramic tile and the mortar occurred with dried pieces and there was a decrease in adherence as the quantity of humidity of the tile increased at the time of its adherence (Bauer, 1995).

The durability of a facade lining system with ceramic tiles, therefore, depends on the exposure conditions. The contraction and expansion movements that result from the variance in temperature and humidity generate tensions in the bond with the substrate, which with the passage of time will result in detachments. These detachments of ceramic facade linings could occur due to adhesive rupture in the ceramic tile/mortar, mortar/gypsum, gypsum/thick frieze, and thick frieze/substrate bonds, or due to a cohesive rupture in the interior of any of these layers (Mansur, 2007). Regarding the rise of pathological problems in linings with ceramic tiles, it was observed that in 84% of the analyzed buildings there was detachment with adhesive rupture in the ceramic tile/frieze bond (Mansur, Do Nascemento and Mansur, 2012). This is due to the fact that this bond is the most requested area of the system for shear stress when thermal effects and the hygroscopic expansion of the ceramic tiles are considered (Abreu, Leitão and Lucas, 2004; Saraiva, Bauer and Bezerra, 2001).

Since the exposure conditions of a specific facade would be difficult to change, the useful life of the lining will depend on the decisions of the project and the quality of the execution, which will define the initial adherence resistance of the lining. The correct specification of the ceramic tile, adhesive mortar, and the adherence procedure is fundamental for this performance.

In this work, we evaluated the relation between the porosity of the ceramic tiles (using three types of ceramics with different water absorption), the composition of the mortar (utilizing two types of mortar), and the curing conditions (adopting the three different forms of curing stablished by the ABNT 14.081-4:2012 standard) with regard to the adherence resistance of the lining system.

2. MATERIAL UTILIZED

We evaluated compositions between a substrate-pattern, ceramic tiles with three different water absorption concentrations, two mortars, and three curing conditions. The substrate-pattern utilized for the adhesion tests was acquired through the provider standardized by the ABNT, addressing the requirements of the NBR 14.08-2 (ABNT, 2012). The absorption of the blocks is of 0.3 cm^3 of water in the course of 4 hours, being below the 0.5 cm^3 limit established by the standard.
Pressed ceramic tiles were utilized with three different water absorption levels (IIa, IIb, and III), which were determined through NBR 13.817 (ABNT, 1997). The water absorption was determined for each type of tile, in accordance to NBR 13.181 (ABNT, 1997), and the water absorption per capillarity in accordance to the specifications of the procedure of the RILEM TC 116 PCD (1999).
Table 1 shows the water absorption values of the ceramic tiles.

Table 1. Water absorption of the ceramic tiles

	BIIa	**BIIb**	**BIII**
Lower limit	3.01%	6.01%	10.01%
Result obtained in the test	4.80%	7.30%	12.50%
Upper limit	6.00%	10.00%	

All the ceramic tiles are within the limits stablished by the NBR 13.817 (ABNT, 1997), confirming the classification of the absorption group indicated by the manufacturer.
The water absorption profile (in g/cm^2) obtained by the procedure of the RILEM can be observed in Figure 1.
The average capillarity coefficient value of the type BIIa ceramic tile is of 0.046 $g/cm^2.min^{½}$, of the BIIb tile it is of 0.085 $g/cm^2.min^{½}$, and of the BIII tile it is of 0.185 $g/cm^2.min^{½}$. The ceramics of group BIIa have the lowest capillarity coefficient, followed by BIIb and, finally, the BIII tiles show the same behavior observed in the water absorption tests.

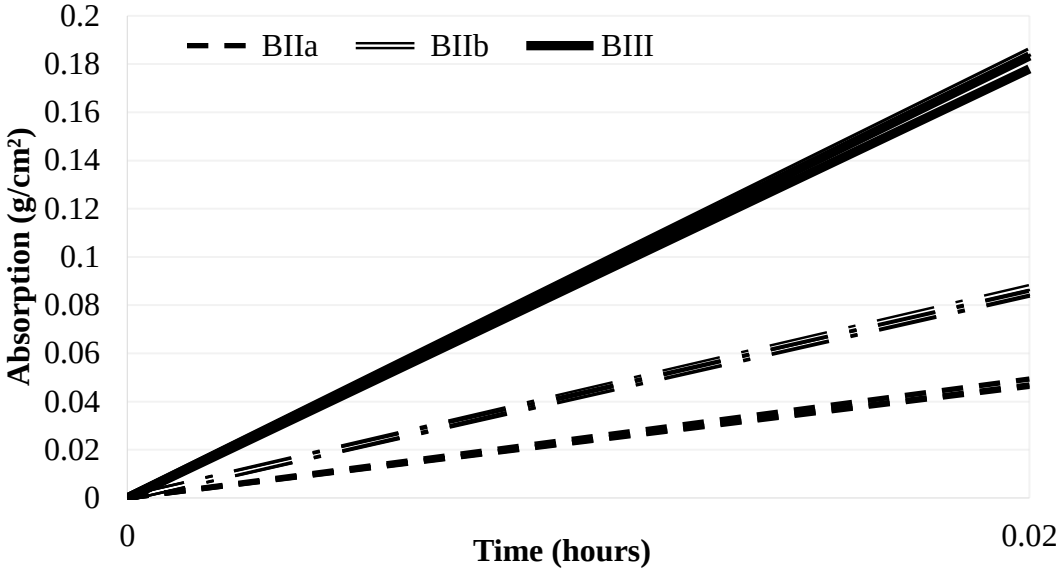

Figure 1. Water absorption per capillarity profile of the ceramic tiles

Two types of industrialized mortar for external applications were used: industrialized adhesive mortar type AC II and industrialized adhesive mortar type AC III, which possess in its composition more adherence promoting additives and water retainers than the type AC II.

The type AC II adhesive mortar used in the study is comprised of Portland cement CP IV (pozzolanic cement), sand, and additives. According to the manufacturer, the additive "Ecocel Uno" has the function of promoting little sliding, workability, and greater water retention. The "PLV 2000" product is a polymer that provides an increase in the chemical resistance and flexibility, in addition to better adhesion.

The adhesive mortar type AC III, in addition to the cited materials, contains calcium formate. Calcium formate is a curing accelerator for Portland Cement based systems, promoting acceleration in the chemical reactions of the aluminates and facilitating the dissolution of the lime. It provides an increase of the open time, less permeability, and a significant increase of the mortar resistance.

The tests carried out in the experimental program are listed in Table 2.

Table 2. Tests carried out and their respective standards.

Characterization tests	Standard utilized
Tests in the fresh state	
Density of the apparent weight	NBR 14.086 (ABNT, 2004)
Consistency index	NBR 13.276 (ABNT, 2005)
Water retention	NBR 13.277 (ABNT, 2005)
Sliding determination	NBR 14.081-5 (ABNT, 2012)
Open time determination *	NBR 14.081-3 (ABNT, 2012)
Tests in the hardened state	
Absorption by capillarity	NBR 15.259 (ABNT, 2005)
Total water absorption	NBR 9.778 (ABNT, 2005)
Resistance to traction in the flexion	NBR 13.279 (ABNT, 2005)
Resistance to compression	NBR 13.279 (ABNT, 2005)
Determination of the dimensional variation and weight	NBR 15.261 (ABNT, 2005)

- Observation: for the execution of this test two sets were utilized comprised by the pattern substrate, ceramic tiles of the absorption group BIII, and adhesive mortar type AC II and AC III prepared in accordance to NBR 14.081-2 (ABNT, 2012) on the pattern substrate in the longitudinal direction.

Of the tests carried out for the characterization in the hardened state, only the test of resistance to traction adherence is planned for by a specific standard of mortars. The other tests were adapted from the standards of linings mortars. The results are shown in Table 3.

Table 3. Characterization of the mortars in a fresh and hardened state.

Mortar Characterization Tests:	**Results:**		**Limits specified by the Standards**
Fresh State	**AC II**	**AC III**	
Density of the apparent weight - γs (g/cm³)	1.46	1.44	-
Consistency index (mm) *	213	214	-
Water retention (%) *	99	99	-
Sliding determination (mm)	0.1	0.1	2
Hardened State	**AC II**	**AC III**	
Capillarity coefficient (g/dm².min½) *	3.49	4.96	-
Total water absorption (%) *	23.78	23.50	-
Vacuum index (%) *	34.51	35.69	-
Real specific weight (g/cm³) *	2.22	2.36	-
Resistance to traction in the flexion (MPa) *	2.5	2.6	Max abs. deviation ≤0.3MPa
Resistance to compression (MPa) *	3.9	4.3	Max abs. deviation ≤0.5MPa

* Adapted from the standards specific to lining mortars

In the fresh state, both adhesive mortar AC II as well as AC III obtained very close results, not being possible to distinguish them from the properties measured in those tests. In the Sliding Determination test the mortars showed the same value, which was lower than maximum 2 mm allowed by the NBR 14.081-5 (ABNT, 2012). In the determination of time in open sky, AC II had a result of 0.50 MPa and AC III of 0.62 MPa. The values obtained in the tests correspond to the NBR 14.081-3 (ABNT, 2012), which specifies a minimum value of 0.50 MPa. In the hardened state, the results for both mortars have very close values, except for capillarity, where mortar AC III obtained a higher value than that of AC II. The adhesive mortar type AC III has a dimensional variation greater than that of type AC II, with significant variation in the early ages, which can be observed in Figure 2.

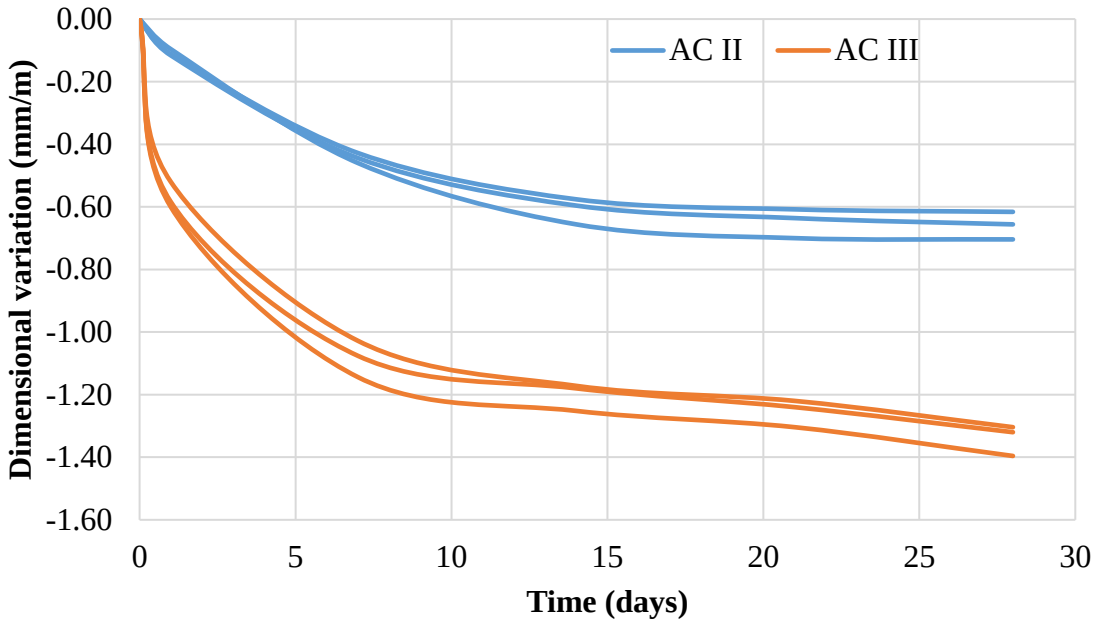

Figure 2. Dimensional variation of the mortars.

Both mortars show great weight variation in the first couple of days (with a variance of 5 to 8%), therefore, contrary to what was verified in the dimensional variation, the weight variation was greater for the type II adhesive mortars. Starting on the seventh day the variation of the two mortars began to stabilize, with little variance until the end of the test, in accordance to what is shown in Figure 3.

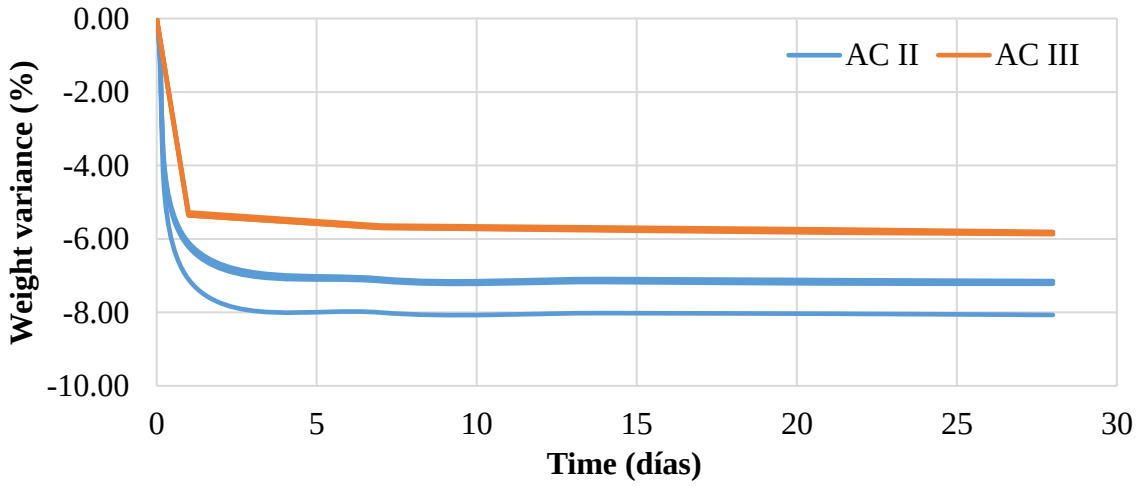

Figure 3. Weight variance of the adhesive mortars.

3. RESULTS AND DISCUSSION ON THE ADHERENCE OF THE SUBSTRATE-PATTERN/MORTAR/CERAMIC TILE SYSTEM

The various systems formed by the combinations between substrate pattern / mortar / ceramic tile were evaluated using the determination of the adherence resistance to traction and of the extension of the adherence. The compositions, in total eighteen sets of ten samples, were identified in the following manner:

- II and III: Type II and III mortars, respectively;
- BIIa, BIIb, and BIII: Ceramic water absorption group;
- N, IA, and AE: Types of curing to which the sets were subjected (normal, water immersion, and stove heating, respectively). The procedures seek to evaluate the behavior of the mortar in different curing situations: the normal condition simulates an ideal implementation condition; curing by immersion simulates the act of wetting due to rain and accumulations that can occur in tiles; and curing with a stove seeks to evaluate the effect of intense exposure to the sun during the curing period.

Following the setting of the ceramic tiles with the use of the mortar on the substrate-pattern, the sets were subjected to three curing conditions. In normal curing (N) the sets remained for 28 days in laboratory environmental conditions (a temperature of 23 ± 2ºC and a relative humidity of 60 ± 5%), in accordance to the specifications of the NBR 14.081-2 (ABNT, 2012). In curing with water immersion (IA) the sets were subjected to laboratory conditions for seven days, subsequently they were immersed in water at (23 ± 2) ºC, where they remained for twenty days. In curing with stove heating (AE) the sets were subjected to normal curing in a laboratory environment for 14 days, after which they were placed in a stove with forced ventilation at a temperature of (70 ± 2) ºC until the age of 28 days. The adherence resistance to traction test was carried out per the NBR 14.081-4 (ABNT, 2012), as can be observed in Figure 4. Ten tests were carried out in each substrate, evaluating the adherence resistance to traction and the extension of the adherence, following the curing period of the sets. The tests were carried out following the specifications of the NBR 14.081-4 (ABNT, 2012), using Dinatest brand equipment, model DS2-DPU-1100, with a maximum capacity of 5000N.

Figure 4. Metallic pieces attached on the ceramic tiles adhered to the substrate-pattern.

Figure 5 shows the average of the results obtained in the adherence resistance test carried out on the sets. Of the nine test sets of the type II adhesive mortar, only those subjected to normal curing complied with the minimum value of 0.5 MPa required by the NBR 14.081-1 (ABNT, 2012). Although the values of the adherence resistance to traction of the type III adhesive mortars were greater than those of the type II mortar, no set using the type III adhesive mortar achieved the minimum adherence value of 1.0 MPa required by the NBR 14.081-1 (ABNT, 2012).

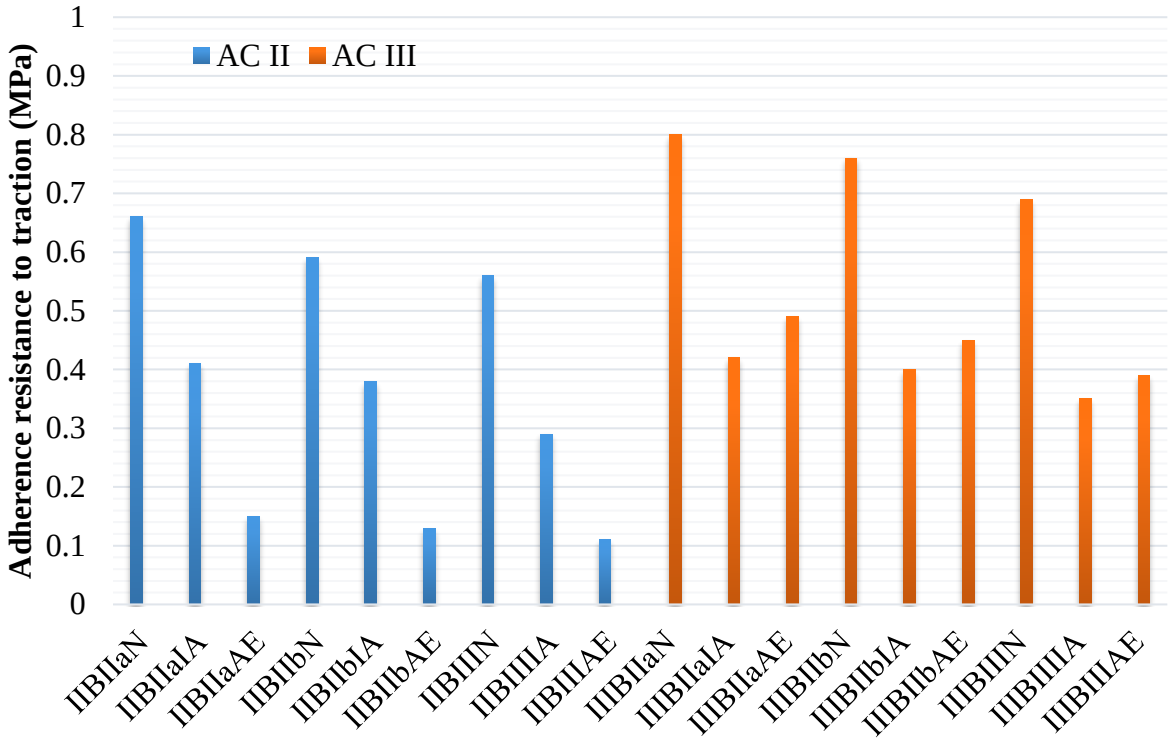

Figure 5. Results of the adherence resistance to traction of the sets executed and the minimum values to be reached, per the NBR 14.081-1 (ABNT, 2012).

The influence of the materials' properties in the adherence resistance of the sets was statistically evaluated. The significance of the effect of the studied variables (independent variables) in the adherence resistance was also evaluated. The results of the analysis are shown in Table 4.

Table 4. Variance analysis of the variables studied in relation to the adherence resistance.

	Sum of the squares	**Degrees of freedom**	**Sum of the average squares**	**Variance value**	**Level of significance**
Adhesive Mortar	1200.50	1	1200.50	22.5133	0.000476
Ceramic tile	245.78	2	122.89	2.3046	0.142235
Curing	5018.11	2	2509.06	47.0530	0.000002

Considering a 5% ($p < 0.05$) level of significance, it is verified that the type of curing is the variable that shows the greatest significant effect, followed by the type of mortar.
Comparing the characteristics of the mortars used, a hypothesis can be made regarding the behavior of the adherence resistance.
The greatest adherence resistance was obtained in the N curing processes (curing at a laboratory environment for 28 days). In the IA (water immersion) curing process, the adherence resistance fell to 60% for the type AC II adhesive mortar and 52% for the type AC III adhesive mortar. In this process, the curing occurs at laboratory temperature and humidity for seven days, followed by the immersion of the pieces. Considering that the two mortars used in the study are Portland pozzolanic cement based (with pozzolan doses of 50%), it can be estimated that the degree of hydration at seven days is still small and that the ensuing saturation, due to the immersion, results in a differential expansion of the ceramic

tile and/or the substrate; this causes shear stress in the interface with the mortar, reducing the adherence of the system. In the AE (with stove) curing process, the adherence fell to 22% for the type AC II adhesive mortar and to 59% for the type AC III adhesive mortar. A period of 14 days is used in this curing process followed by heating in a stove until the age of 28 days, which significantly harms the curing process of the pozzolanic cement and causes the lowest adherence resistance. For the type, AC III adhesive mortar, losing the adherence resistance of the curing with water immersion is almost equivalent to losing the adherence resistance of the curing with stove heating, brought about by to the presence of calcium formate in its composition, which accelerates the increase of the adherence resistance at early ages.
It is observed that for all the mortars and curing conditions, the adherence resistance of the BIIa ceramic tiles was superior to that of the BIIb ceramic tiles, which was also superior to the adherence of the BIII ceramic tiles. This result has a direct relation with the water absorption of the ceramic tiles, indicating that excess water absorption can harm the adherence.
The internal face of the ceramic tiles used in the adherence test was photographed for the determination of the adherence extension. The program AutoCAD was used, implementing the "polyline" command and manually tracing the borders of the adhered region. Finishing the execution of the tracings, these were reticulated and the area was determined. Figure 6 (right) shows the reticule with the tracing highlighted in white and with the use of a transparency effect.

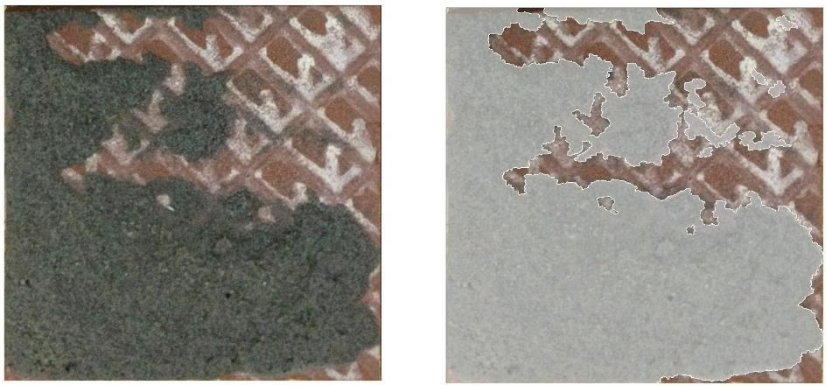

Figure 6. Visualization of the adherence extension of a ceramic tile.

Adherence extension was elevated in all the sets, as only the sets IIBIIbN and IIIBIIbN have an average adhesion extension value below 90%. Figure 7 shows the individual results for the adherence extension of the 180 tiles tested, making it possible to affirm that there is no direct relation between adherence extension and resistance. The adherence extension can be influenced by the nature of the materials that comprise the substrates and the mortars, as well as the properties of the mortars themselves (Maura, 2007). A good adherence extension, even when basic, is not enough to guarantee a good fastening of the mortar applied to substrates of ceramic blocks (Pagnussat, 2013).

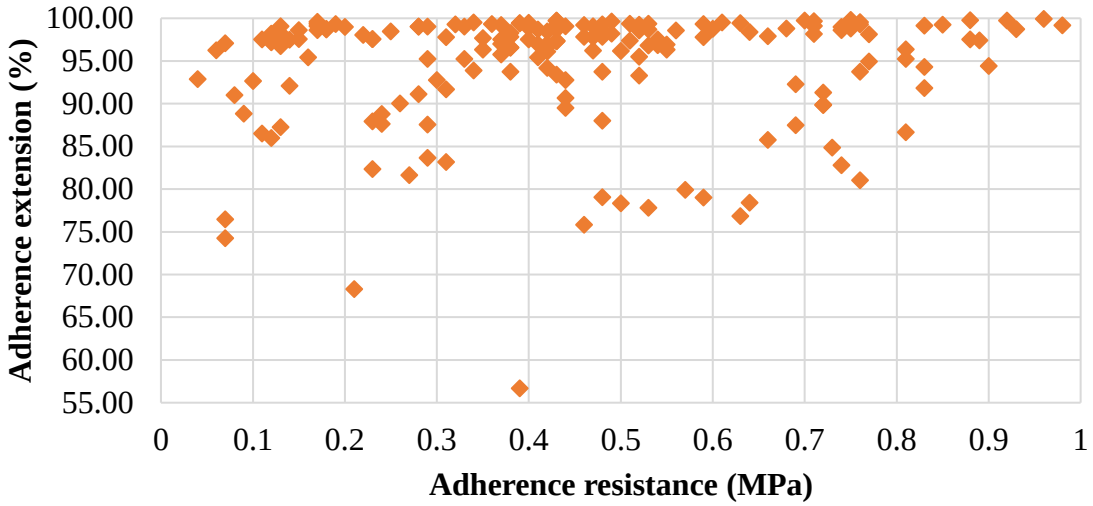

Figure 7. Adherence extension x adherence resistance.

The influence of the open time of the mortar (time between the mixing of the mortar with water and its usage) in the adherence resistance and extension of the ceramic tiles was evaluated for type AC II and AC III adhesive mortars and was shown to be significant. An open time of 5 and 20 minutes was used. The adherence resistance decreased close to 10% and the adherence extension decreased between 40 and 50%, as can be seen in Figure 8.

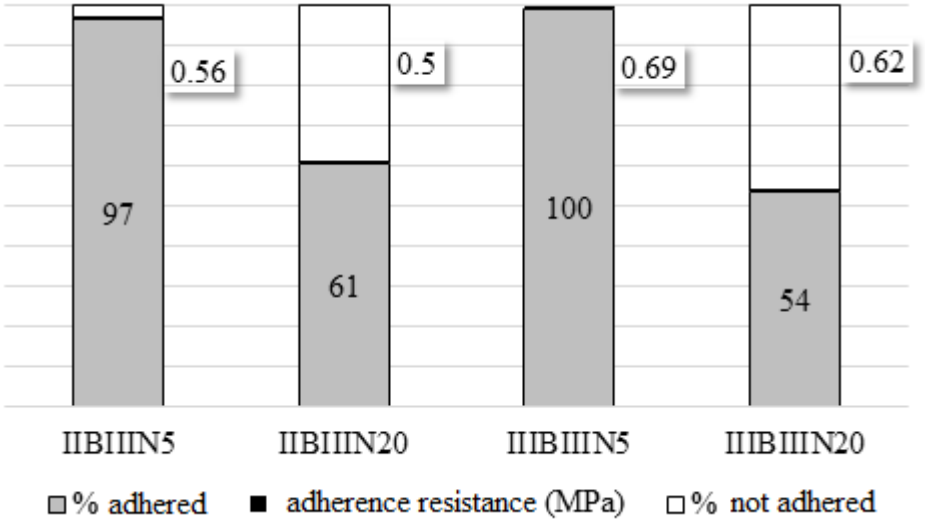

Figure 8. Adherence extension in terms of the open time of the mortars.

Figure 9 shows the adherence extension loss typical of the application of the ceramic tile after an excessive wait time, resulting in the loss of adherence extension and a decrease of the adherence resistance to traction. The phenomenon occurs due to the increase in the rigidness of the borders of the mortar, which hinders its distribution during the setting of the ceramic tile.

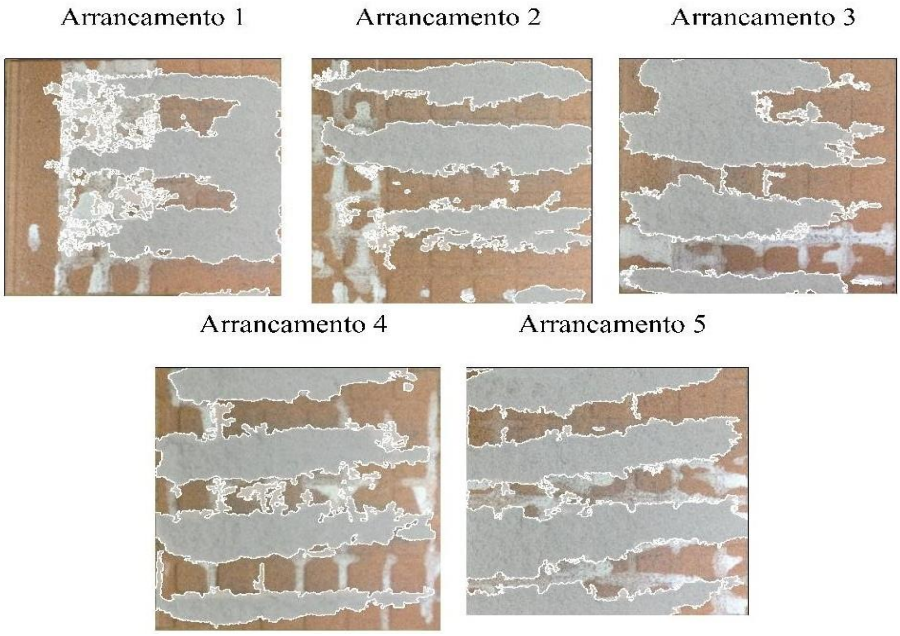

Figure 9. Adherence extension typical of the setting of the ceramic plate after an excessive wait time.

4. FINAL CONSIDERATIONS

Through the analysis of the results of the tests carried out, it can be observed that:

- For all the adhesive mortars used, all of which are Portland cement based, the curing condition is the most significant variable in the results for adherence resistance to traction, followed by the type of mortar. This highlights the curing differences typical of the application process of ceramic tiles in facades, where the pieces are subjected to significant differences in temperature and humidity, as well as the eventual wetting due to precipitation during the curing period. Normal curing (laboratory environment with a temperature of 23 ± 2ºC and relative humidity of 60 ± 5%) showed the best results, and it was the only curing condition in which the studied mortars were approved in the sets of tests provided for in the Standards;
- In a shared analysis of all the results, the characteristics of the ceramic tile, in terms of permeability, did not influence significantly in the adherence resistance of the system. Whereas considering a determined type of adhesive mortar and a specific curing condition, the increase in the water absorption of the ceramic tile implies a decrease in the adherence resistance;
- There is no statistically significant relation between the adherence extension and the adherence resistance of the ceramic tiles;
- The wait time between the mixture of the mortar with water and its use exercises great influence in the adherence extension of the ceramic tile and decreases its adherence resistance. This fact warns of the need for the specification of maximum times for the application of mortars, which ought to be controlled during the application;
- Considering the materials used, the only groups that reached the minimum adherence resistance to traction stipulated by the NBR 14.0891-1 (ABNT, 2012) were IIBIIaN, IIBIIbN, and IIBIIIN, all of which used the same adhesive mortar (AC II) and were subjected to the same type of curing (Normal).

5. REFERENCES

Abreu, M., Leitão, V., Lucas, J. C. (2004), *"Modeling the Behavior of Ceramic Tile Coverings"*, VIII World Congress on Ceramic Tile Quality – Qualicer, Castellón: (España), p. 3.

Antunes, G. R. (2010), *"Estudo de manifestaciones patológicas em revestimiento de fachada em Brasília - sistematizacción da incidência de casos"*. Dissertação de Mestrado, Universidade de Brasília, p. 48.

Associacción Brasileira de Normas Técnicas. *NBR 9.778* (2005), *"Argamassa e concreto endurecidos – Determinación da absorción de agua, índice de vazios e massa específica"*, Rio de Janeiro, pp. 1-4.

Barros, M. M. S. B.; Sabbatini, F. H. (2001), *"Produção de revestimientos cerámicos para paredes de vedacción em alvenaria: diretrizes básicas", (*São Paulo, Brasil: EPUSP), p. 27.

Bauer, R. (1995), *"Despegados em revestimientos cerámicos, análises e recomendações"*, in: Simpósio brasileiro de tecnologia de morteros. ANTAC, Goiânia (Brasil), pp. 193-201.

British Standards Institution (BSI). (2015), *"Wall and floor tiling – Part2: Design and installation of external ceramic, natural stone and mosaic wall tiling in normal conditions"*, Code of practice – BS5385-2**.** London, p. 36.

Campante, E.D.; Baía, L.L. M. (2008), "*Proyecto e execução de revêstimento cerámico",* (São Paulo, Brasil: O Nome da Rosa), pp. 87-90.

Cnew, M. Y. L. (1992), *"The Study of Adhesion Failure of Wall Tiles"*, Building and Environment, v 27, nº4, pp. 493-499.

Consoli, O. J. (2006), *"Análise da Durabilidad dos Componentes das Fachadas de Edificios, Sob a Ótica do Proyecto Arquitetônico",* Dissertacción de Mestrado, Universidade Federal de Santa Catarina, p. 96.

Goldberg, R. P. (1998), *"Direct adhered ceramic tile, stone and thin brick facades"*, Technical design manual. (USA: Laticrete International), p. 117.

Mansur, A. A. P. (2007), *"Mecanismos Físico-Químicos de Adherencia na Interface Argamassa Modificada com Polímeros/Cerámica de Revestimiento",* Tese de Doutorado, Universidade Federal de Minas Gerais, p. 3.

Mansur, A. A. P.; Do Nascemento, O. L.; Mansur, H. S. (2012), "*Mapeamento de Patologias em Sistemas de Revestimiento Cerámico de Fachadas*", Construindo, v. 4, n. 01, p. 64.

Moura, C.B. (2007), *"Adherencia de revestimientos externos de morteros em sustratos de concreto: influência das condiciones de temperatura e ventilacción na cura do chapisco",* Dissertacción de Mestrado, Universidade Federal do Rio Grande do Sul, p. 29.

NBR 13.276 (2005), *"Argamassa para asentamiento e revestimiento de paredes e tetos – Preparo da mistura e Determinación do índice de consistência",* Rio de Janeiro, pp. 1-3.

NBR 13.277 (2005), *"Argamassa para asentamiento e revestimiento de paredes e tetos – Determinación da retenção de agua"*, Rio de Janeiro, pp. 1-3.

NBR 13.279 (2005), *"Argamassa para asentamiento e revestimiento de paredes e tetos – Determinación da resistencia a tracción na flexão e a compressão"*, Rio de Janeiro, pp. 1-9.

NBR 13.817 (1997), *"Placas cerámicas para revestimiento – Clasificación"*, Rio de Janeiro, pp. 1-2.

NBR 13.818 (1997), *"Placas cerámicas para revestimiento – Especificación e métodos de ensayo"*, Rio de Janeiro, pp. 11-13.

NBR 14.081-1 (2012), *"Argamassa colante industrializada para asentamiento de placas cerámicas – Parte 1: Requisitos"*, Rio de Janeiro, pp. 1-5.

NBR 14.081-2 (2012), *"Argamassa colante industrializada para asentamiento de placas cerámicas – Parte 2: Execução do substrato-patrón e aplicación da argamassa para ensayos"*, Rio de Janeiro, pp. 1-9.

NBR 14.081-3 (2012), *"Argamassa colante industrializada para asentamiento de placas cerámicas – Parte 3: Determinación do tiempo em abierto",* Rio de Janeiro, pp. 1-6.

NBR 14.081-4 (2012), *"Argamassa colante industrializada para asentamiento de placas cerámicas – Parte 4: Determinación da resistencia de adherencia a tracción"*, Rio de Janeiro, pp. 1-7.
NBR 14.081-5 (2012), *"Argamassa colante industrializada para asentamiento de placas cerámicas – Parte 5: Determinación do deslizamento"*, Rio de Janeiro, pp. 1-6.
NBR 14.086 (2004), *"Argamassa colante industrializada para asentamiento de placas cerámicas – Determinación da densidade de massa aparente"*, Rio de Janeiro, pp. 1-2.
NBR 15.259 (2005), *"Argamassa para asentamiento e revestimiento de paredes e tetos – Determinación da absorción de agua por capilaridad e do coeficiente de capilaridad"*, Rio de Janeiro, pp. 1-3.
NBR 15.261 (2005), *"Argamassa para asentamiento e revestimiento de paredes e tetos – Determinación da variación dimensional (retracción ou expansión linear) "*, Rio de Janeiro, pp. 1-6.
Pagnussat, D. T. (2013), *"Efeito da temperatura de queima de blocos cerámicos sobre a resistencia de adherencia a tracción de revestimientos de argamassa",* Tese de Doutorado, Universidade Federal do Rio Grande do Sul, p. 161.
Ribeiro, F. A. (2006), *"Especificación de Juntas de Movimentacción em Revestimientos Cerámicos de Fachadas de Edificios: Levantamento do Estado da Arte",* Dissertacción de Mestrado, Escola Politécnica da Universidade de São Paulo, pp. 43-45.
RILEM Technical Committees. RILEM TC 116 PCD (1999), "*Permeability of concrete as a criterion of its durability*", Materials and Structures, v. 32, pp. 174-179.
Saraiva, A. G.; Bauer, E.; Bezerra, L. M. (2001), *"Análise das tensiones entre argamassa colante e placas cerámicas submetidas a esfuerzos de natureza térmica",* Revista Ambiente Construído, v. 2, n. 2, pp. 47-56.

ALCONPAT Journal, Volume 6, Issue 2, may – august 2016, Pages 129 – 144

ALCONPAT Journal

www.revistaalconpat.org

eISSN 2007-6835

Journal of the Latin-American Association of Quality Control, Pathology and Recovery of Construction

Influence of the thickness of the coating of the elements of reinforced concrete exposed to corrosion processes and subjected to external loads

R. S. Meneses[1], J. M. Moro[1], R. R. Aveldaño[1], N. F. Ortega[1]

[1] Engineering Department, Universidad Nacional del Sur, Bahía Blanca, Argentina.

Article information
DOI:
http://dx.doi.org/10.21041/ra.v6i2.134
Article received on February 02th 2016, reviewed under publishing policies of ALCONPAT journal and accepted on April 11th 2016. Any discussion, including the replica of the authors, shall be published in the first number of the year 2017 as long as the information is received prior to the closing of the third number of the year 2016.

Legal Information

ALCONPAT Journal, Year 6, No. 2, May – August 2016, is a quarterly publication of the Latin American Association of Quality Control, Pathology and Construction Recovery, International, A.C., Km. 6, Old Highway to Progreso, Mérida, Yucatán, Zip Code 97310, Tel. +52 1 (999) 738-5893, alconpat.int@gmail.com, Website: www.alconpat.org
Responsible Editor: Dr. Pedro Castro Borges. All rights reserved for exclusive use, No. 04-2013-011717330300-203, eISSN 2007-6835, both granted by the National Institute of Copyright. Responsible for the last update of this number, Informatics Unit ALCONPAT, Elizabeth Sabido Maldonado, Km. 6, Old Highway to Progreso, Mérida, Yucatán, Zip Code 97310, publication date: May 30, 2016.

ABSTRACT

When carrying out corrosion studies on reinforced concrete, it is important to consider the action of external loads in the tests, as this situation is the most frequent in the structures. In this work, we show the results obtained from exposing beams of reinforced concrete subjected to flexional effects, materialized with loads that generate equal tensile stress on the corroded reinforcement, to an accelerated corrosion process. The beams were manufactured with different coating thicknesses on the reinforcement and with a concrete of 25 MPa characteristic resistance. This study evidences the influence of the coating thickness of the reinforcement on the corrosion process and its external manifestation (cracking of the coating), compared with the same mechanical requests.

Keywords: corrosion of tensile reinforcement; coating; cracking.

RESUMEN

Al realizar estudios sobre corrosión en hormigón armado, es importante considerar en los ensayos, la acción de cargas externas, pues esta situación es la más frecuente en las estructuras. En este trabajo, se presentan los resultados obtenidos al exponer a un proceso de corrosión acelerada, a vigas de hormigón armado sometidas a esfuerzos flexionales, materializados con cargas, que generan iguales tensiones de tracción en las armaduras corroídas. Las vigas se fabricaron con diferentes espesores de recubrimiento de las armaduras y con un hormigón de resistencia característica 25 MPa. Este estudio pone en evidencia la influencia del espesor de recubrimiento de las armaduras, sobre el proceso de corrosión y su manifestación externa (fisuración del recubrimiento), frente a las mismas solicitaciones mecánicas.

Palabras claves: corrosión de armaduras traccionadas; recubrimiento; fisuración.

RESUMO

Ao realizar estudos sobre corrosão em concreto armado, é importante considerar nos ensaios a ação de cargas externas, pois esta situação é mais frequente nas estruturas. Neste artigo apresentam-se os resultados obtidos ao expor vigas de concreto armado a um processo de corrosão acelerada, submetidas a esforços de flexão materializados com cargas que geram tensões constantes de tração nas armaduras corroídas. As vigas foram elaboradas com diferentes espessuras de cobrimento das armaduras e com um concreto de resistência característica de 25MPa. Este estudo coloca em evidência a influência da espessura de cobrimento das armaduras, sobre o processo de corrosão e sua manifestação externa (fissuração do cobrimento), frente às mesmas solicitações mecânicas.

Palavras-chave: corrosão de armaduras tracionadas, cobrimento, fissuração.

Corresponding author: Romina S. Meneses (romina.meneses@uns.edu.ar)

1. INTRODUCTION

Concrete is the material most used in construction worldwide. The structures built with this material have a certain useful life, where the processes that cause its degradation affect the aesthetic and, mainly, its functionality—which becomes apparent with the appearance of stains, cracks, chipping of the coating, etc.

One of the most common pathologies that manifest in reinforced or pre-stressed concrete is the corrosion of its metallic reinforcement. The steel of the reinforcement is protected from corrosion by a passive layer of cement hydration products, comprising an alkaline environment. In marine environments, however, the chloride ions accumulate in the surface of the concrete and slowly penetrate towards its interior, until reaching the metallic reinforcement so that, after a certain concentration, they dissolve the layer that protects the steel and thus a corrosion process is initiated. These products of corrosion have a much higher volume than that of the steel from which they originate; at first, they are housed in the pore structure of the concrete, but once this is filled, internal stress begins to build up (Peralta, 2009), which in turn ends up generating cracks in the coating (Alonso, 1996; Andrade, 1993).

This cracking of the coating favors the advance of the deterioration of the affected structures, as it allows the entry of external agents (chloride, water, and oxygen) towards the reinforcement, causing a decrease of the steel section and affecting the adherence between both materials (Al-Sulaimani, 1990; Almusallam, 1996; Rodríguez, 1993). In this manner, as the deterioration advances, the section modulus of the affected structural element decreases, having negative consequences on the bearing capacity and useful life of the affected structure (Melchers, 2001; Rodríguez, 1996; Rodríguez, 1998; Torres-Acosta, 2007).

There is a series of factors that control the cracking process of the coating (Alonso, 1998), among them, the following stand out: the environment to which the structure is exposed (Aveldaño, 2011) and the properties of the concrete, in terms of the mechanical structure of the coating (Rodríguez, 1998), as well as by the need to have a pore structure to provide tightness. Therefore, within the properties of the concrete, capillary absorption (related to the pore structure) plays a rather important role, which has led to various countries dictating standards that stablish maximum values for it (Instituto Argentino de Normalización y Certificación, 2005). In previous works with beams developed with different concretes and free of external loads, carried out in the laboratory where these investigations materialized (Schierloh, 2001; Schierloh, 2003), it was established that the capillary absorption influences in the appearance of the first cracks caused by corrosion and the evolution of the corrosion potentials; during the time of the accelerated corrosion tests, no significant correlations were found between the cracking frame produced by the corrosion with the electrochemical behavior registered during the tests. Other factors to be considered in the corrosive process and its effects, are related to the manner in which the reinforcement of the structure is distributed (Aveldaño, 2009; Hariche, 2012) and the mechanical requests to which the reinforcement in the corrosion process is subjected, which are inevitably associated to the stressed state of the concrete that surrounds it (Aveldaño, 2013).

Regarding the stress state of the reinforcement, it could be said that it introduces a certain uncertainty in the corrosive processes and their consequences. Despite the importance of the topic, which in the case of the reinforcement subject to tensile stress could cause the phenomenon known as “corrosion under stress”, research on concrete structures is scarce. However, there have been some works in recent years (Calabrese, 2013; Elfergani, 2012; Fumin, 2011; Ortega, 2011). Although the reinforced concrete structures in service normally corrode under static and/or dynamic loads (for example, bridges), there have been few studies in this regard in comparison with those that analyze structures undergoing corrosion without external loads.

The expected behavior of a structure subject to the effects of corrosion and at the same time under the effects of external loads (both static and dynamic), is different from the evolution of corrosion when there are no such loads; therefore, some research was directed to the study of this topic. (Hariche et al., 2012) studied reinforced concrete beams exposed to accelerated corrosion, where the main parameters that varied in their investigations were the arrangement of the reinforcement and the magnitude of the external loads (Hariche et al., 2012; Yu et al., 2015). They analyzed the evolution of the corrosion and the cracking in beams cracked under the constant effect of external loads and exposed in a saline chamber, carrying out two sets of beams with differing casting directions, in relation to the tensile reinforcement. (Linwen, 2015 and Malumbela et al., 2009) studied beams under accelerated corrosion with applied loads well under the breaking point, where they monitored the variation of the depth of the neutral axis, the curvature, and the moment of inertia.

In this work, we present the results of tests carried out on reinforced concrete beams with different coating thicknesses, subjected to a process of accelerated corrosion and under the effect of static external loads. Said tests were meant to evaluate the behavior of the same, from the point of view of the corrosion of its reinforcement and its external (cracking of the coating of the concrete) and internal (corrosion potentials) effects. Regarding this issue, there has been a lot of work done on beams without external loads, but we found no analogous work to the one presented in this paper.

2. EXPERIMENTAL PROCEDURE

2.1 Materials used

The materials used in the cement mixture were the following:

- Cement: Ordinary Portland Cement (OPC40) was used, which came from a factory located in the Province of Buenos Aires (the central zone of Argentina).
- Fine aggregate: composed of natural silica sand that came from a deposit located to the south of the Province of Buenos Aires, which complies with the quality specifications stablished by Standard IRAM 1627 (Instituto Argentino de Normalización y Certificación, 1997).
- Coarse aggregate: composed of pebbles whose Maximum Nominal Size was of 25 mm, which complies with the granulometric limits establish in Standard IRAM 1627 (Instituto Argentino de Normalización y Certificación, 1997).

The cement was elaborated with a water/cement (w/c) ratio of 0.50, a value adopted by the Argentinian standard (Instituto Argentino de Normalización y Certificación, 2005) for resistant structures that are more than 1 Km from the coast, in a zone influenced by winds with sea salt. Details on the dosage used are shown in Table 1.

Table 1. Composition and characteristics of the cement

Constituent materials	Kg/m^3 of cement
Ordinary Portland Cement	350
Fine aggregate (natural silica sand)	895
Coarse aggregate (pebbles)	920
Drinking tap water	190
Water/cement ratio	0.50

2.2 Elaboration of the samples

Four reinforced cement beams in which the coating/diameter of the bars relation varied were manufactured in order to simulate different degrees of protection of the reinforcement; in addition, cylindrical test pieces were molded with the objective of characterizing their mechanical (compression and tension) and physical (capillary absorption test) behavior.

The beams had a 8 x 16 cm section and a longitude of 220 cm, the longitudinal reinforcements were corrugated steel bars of natural hardness (ADN 420, IRAM-IAS U 500-528) (Instituto Argentino de Normalización y Certificación, 1989), which is the steel used for construction in Argentina—with a diameter of 4.2 mm (two bars in the upper face and two in the lower one), and closed smooth steel abutments of: 2.1 mm in diameter, separated every 10 cm, with a coating that varied between 10 mm and 25 mm. It must be made clear that the selection of the diameters used in the tests was due to wanting to maintain the geometrical likeness of the laboratory beams (to 1/3 the size of the real structure) to the means used in real structures, therefore, bars commercially available in the country in question were used. Table 2 shows the characteristics of the reinforcement.

Table 2. Characteristics of the reinforcement

	Type of steel	**Diameter (mm)**	**Elastic limit (MPa)**	**Breaking strain (MPa)**
Longitudinal reinforcement	Natural hardness	4 x 4.2	680	690
Abutments	Smooth	2.1	640	640

The concrete was sieved in the caissons and mechanically vibrated, moistening it during the first 7 days. Subsequently, the curing continued in a laboratory environment (temperature ≈ 20ºC, relative humidity ≈ 50%) for approximately 60 days. Cylindrical concrete test pieces (15 x 30 cm) were also elaborated, which were used in the physical capacity and capillary suction speed tests (IRAM 1871) (Instituto Argentino de Normalización y Certificación, 2005), as well as in mechanical tests: resistance to compression (IRAM 1546) (Instituto Argentino de Normalización y Certificación, 1992) and indirect tension (IRAM 1658) (Instituto Argentino de Normalización y Certificación, 1992). They were molded and cured in accordance with the standard IRAM 1534 (Instituto Argentino de Normalización y Certificación, 1985).

2.3 Accelerated corrosion process

In order to obtain the tensile stress of the superior reinforcement (which would be the one that would have been subsequently subjected to a process of accelerated corrosion), loads were placed at the extremes of the beams, adopting an intermediate area as the area to be corroded, and leaving overhangs on the two lateral sides. Figure 1 shows the adopted structural outline. The area between the supports possesses an almost constant bending stress, therefore, the entire area of the bars affected by the corrosion is subject to a stress that is practically equal in intensity, by being subjected in each case to its own weight plus the effect of various loads that varied from 90 kg to 100 kg.

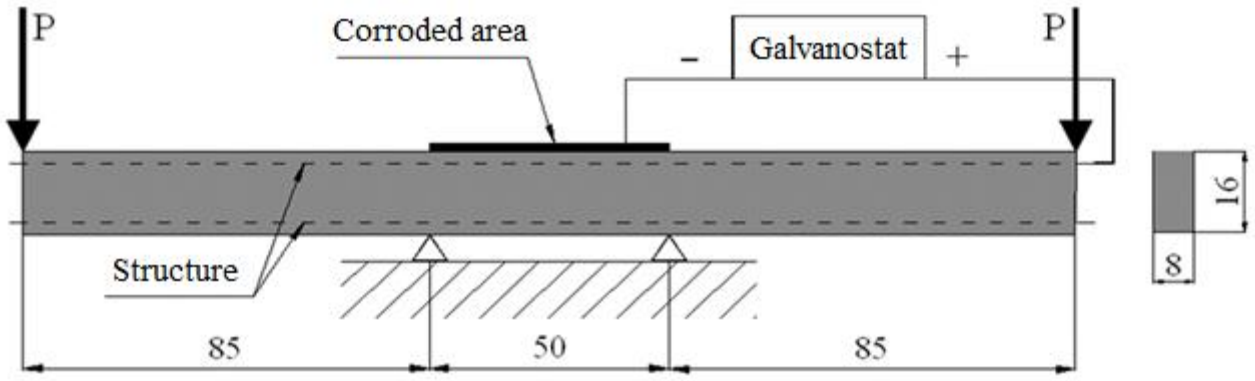

Figure 1. Outline of the Test

The elements were subjected to accelerated corrosion for approximately 160 days through the application of an external printed current, provided by a galvanostat connected between an exposed end of the upper reinforcement (anode) and a contra-electrode (cathode) comprised of a stainless-steel mesh (of 50 cm in length and of the same width as the beam), located in its upper face. A sponge (of equal dimensions) was placed on it, which was kept moist with a controlled quantity of an aqueous solution with 0.3% (in weight) of sodium chloride (NaCl) (3 g NaCl / litter of water). Prior to connecting the galvanostat, the moistening of the central area began for 2 days in order to ensure that the entire coating had the necessary humidity to allow the circulation of the current. In order to have a controlled moistening (reducing evaporation), an acrylic plate followed by a nylon canvas were placed. The density of the applied current was of 100 μA/cm^2, which is around ten times the measure in highly corroded reinforced concrete structures (Rodríguez, 1993); it was chosen for having been adopted by various groups for their research in the issue (Acosta, 1998; Alonso, 1994; Alonso, 1998; Aveldaño, 2011) with the purpose that when the process in study was finalized, results of corrosion penetrations greater than 0.30 mm in the bars were obtained within a reasonable time.

It is worth clarifying that to achieve an accelerated corrosion with this method, the corrosion process is started simultaneously in all the beams by connecting them to the galvanostat, regardless of the coating they have. Therefore, what is being studied in this work is the corrosion process and the symptoms it generates from the implementation of the exterior current. Logically, in existing structures affected by an environment with chlorides, the reinforcement that has a greater coating takes a longer time to depassivate (the start of corrosion) and this process, which precedes corrosion, is studied by researchers that work in the penetration of chlorides and in carbonation, lines of research different from that of this work. In the analysis presented in this work, we try to represent the period following the initiation (denominated the corrosion propagation period). The two periods mentioned are those studied and defined by Tuutti (Tuutti, 1982), in his well-known diagram of the useful life of reinforced concrete structures in terms of the corrosion of their reinforcement.

It is assumed that the reinforcement affected by corrosion has a surface of 162 cm^2 (determined by the central 50 cm of the bars and by the 6 abutments that are located in this area, assuming that the corrosion extends up to a longitude in the vertical branch of the 1 cm abutments). In order to provide a current density of 100 μA/cm^2, the galvanostats provided a current intensity of 16.2 mA. At the end of the test the reinforcement was uncovered, observing a non-uniform attack and showing pitting (which indicates that the chlorides act on the surface of the bars); it was established that in the longitudinal reinforcement, the corrosion had surpassed the central 50 cm by a couple of centimeters on each side of this area (up to

where the humidity reached the coating), with a small corrosion depth (the corrugate of the bars was clearly visible) and, to a lesser extent, something similar occurred with the abutments.

Table 3 identifies the beams tested in accordance to the relation of the thickness of the coating / diameter of the reinforcement adopted for each beam (r/ϕ) and the applied load (P), the magnitude of which varied so as to produce the same stress in the tensile reinforcement for all cases. The analyses were carried out using this ratio, as is the case for much of the bibliography on the subject and not just with the coating, in order to generalize the results obtained. On the other hand, it is worth remembering that regardless of the coating used, so long as the same r/ϕ ratio is maintained, the cracking process shall be practically identical. In (Peralta M.H. et al., 2006), a numeric study can be observed in which the evolution of the stress in various places of the cement coating, prior to cracking, is established; thus, determining the pertinence of carrying out the analysis using this ratio.

Table 3. Denomination of the beams

Denomination	**Coating/diameter ratio (r/ϕ)**	**Applied load (P) (Kg)**
V90	6.0	90
V93	4.8	93
V96	3.6	96
V100	2.4	100

2.4 Determinations carried out during the tests

First of all, the beams were loaded and the initial cracking by flexion was measured prior to moistening. The follow-up of the surface of the beams was done by observing them daily and recording the moment the first stains and cracks appeared due to corrosion. From the emergence of these first cracks, the periodical measure of the width (by comparison with a graduated Vernier, with a minimum division of 0.05 mm (see Figure 2)) and length of the same (with a graduated ruler that possess a millimeter precision) was performed. This task was carried out in order to find the maximum crack widths and the cracking areas, which are obtained as the sum of the lengths of each crack, multiplied by their respective width.

At the same time, the corrosion potentials were recorded in order to carry out an electrochemical follow-up of the corrosion processes (Figure 3), in accordance with a standardized procedure (American Society for Testing and Materials, 1980). These were measured with a CANIN (PROCEQ) brand voltmeter, utilizing a Copper – Copper Sulfate (CSC) reference electrode especially built to carry out measures in concrete structures. The corrosion potentials in the central 50 cm of the central area affected by corrosion were determined in 5 equidistance points, averaging the values of the same.

Figure 2. Measurement of the width of a crack generated by accelerated corrosion.

Before taking the measurements, it was moistened for 2 days with the aforementioned NaCl 0.3% solution in weight, until reaching constant moisture; subsequently, a constant current density was applied through a galvanostat for the duration of the test. Under these conditions, the evolution of the corrosion potential was followed-up at various characteristic points of the beam (on the dry and humid areas, coinciding or not with the abutments). All the measurements were carried out by previously disconnecting the galvanostat, and the cement was moistened in the areas where the determinations would be subsequently carried out, such that the measurements of the potentials would stabilize quickly. This moistening process normally lasted a couple of hours.
The theoretical penetration of the attack on the bars was determined using the Faraday law (Alonso, 1998), assuming a uniform corrosion of the reinforcement; therefore, it could be said that the determined penetration is an average value and could be estimated through the following expression:

$$x = 0.0116\, i_{corr}\, t \qquad (1)$$

Where: x: depth of the attack [mm];
0.0116: conversion factor of the units;
i_{corr}: density of the corrosion current [$\mu A/cm^2$];
t: duration of the attack [years].

This average depth of attack on the bars is obtained through the corrosion speed represented by i_{corr}, which is kept constant by the galvanostat.

3. RESULTS AND DISCUSSION

3.1 Characterization

Table 4 shows details on the results obtained from the characterization tests of the properties of the concrete.

Table 4. Characteristics of the concrete used on the tested beams

Compression (MPa)	Indirect tension (MPa)	Capillary suction capacity (g/m^2)	Capillary suction speed ($g/m^2.s^{1/2}$)
27.0	2.5	2.773	3.45

According to the experimentally obtained results, the capillary suction speed is below 4 g/m^2 s$^{1/2}$, the maximum value for the capillary suction speed allowed by the Argentinian standard (Instituto Argentino de Normalización y Certificación, 2005); thus, the concrete is adequate for the structures located in environments with the presence of chlorides.

3.2 Electrochemical follow-up

Figure 3 shows the electrochemical behavior of the reinforcement, where the evolution of the corrosion potentials was graphed, representing the average of the measurements obtained on 5 points located in the central area affected by corrosion on each of the 4 tested beams. There are two scales on the abscissa axis, one represented by the time passed since starting the test and, in the upper part of this figure, the theoretical penetration of the attack, which is an average value fixed with the Faraday law (Equation (1)), applied to the material losses in the reinforcement located in the central area of the beams.

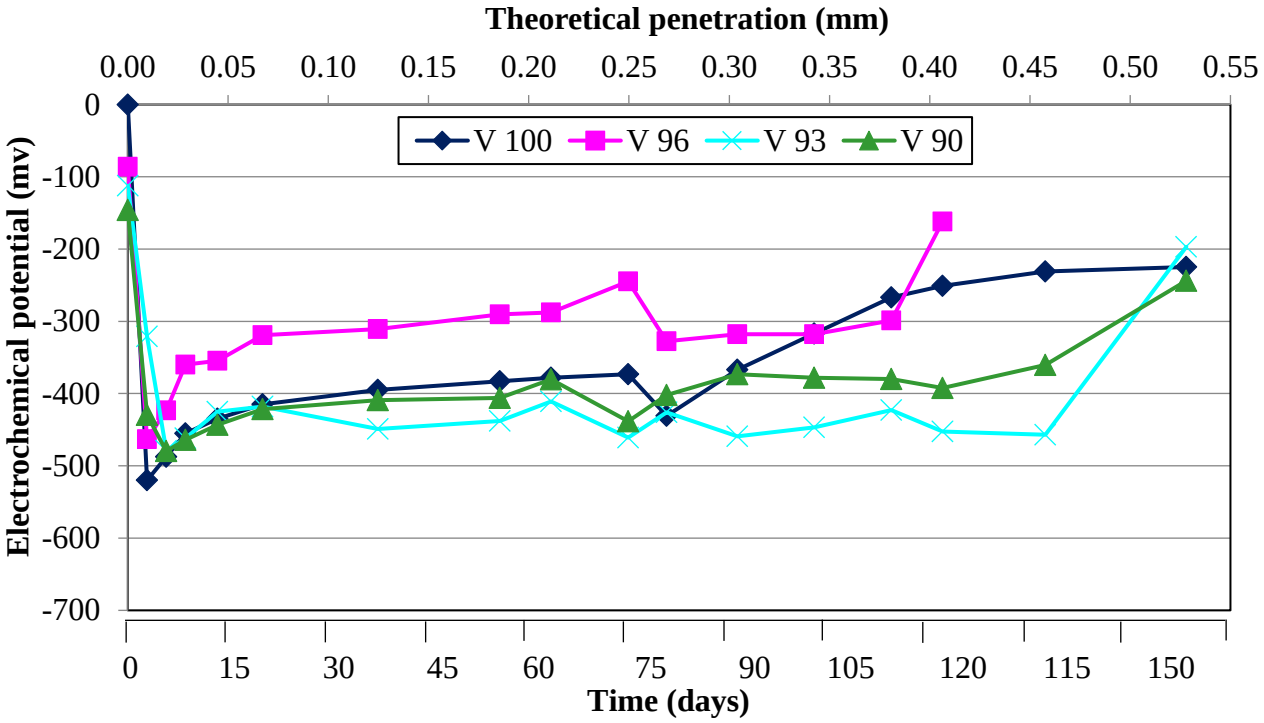

Figure 3. Average corrosion potentials (moistened area), in terms of the theoretical penetration and time

It is worth noting that while the test was prolonged for approximately 160 days, when reaching 140 days, beam V96 reached the point of collapse (Figure 4) due to a significant reduction of the cross-section of its reinforcement, produced by the depth of the pitting caused by the corrosion. Whereas beam V100 broke at 160 days, at which time the tests were finalized. This indicates that the corrosive process as is known, affects the residual life of the structural element affected, but that pitting, in particular, can decrease it even more.

Figure 4. Beam V96 after collapse

The electrochemical behavior analyzed in the four beams, through the follow-up of their corrosion potentials, showed that in the course of the first 5 days, since connecting the accelerated corrosion process, the minimum potential value was reached; the beams with less coating (V96 and V100) were the ones that completed their activation period first (with minimum potentials between -478 and -531 mV). Subsequently, an increase of these potentials can be observed that could be considered as a pseudo-passivation process that is accompanied by the generalization of cracking (see Figure 5), which was similar on all the beams. Although the potentials of the two beams with lower coating / reinforcement diameter ratio are somewhat higher than the other two, it could be said that these are more passivated due to allowing an easier entry for oxygen from the exterior. This process was also found in previous works carried out in this laboratory (Aveldaño, 2011; Aveldaño, 2013; Schierloh, 2001).

3.3 Follow-up of the cracking areas

It is known that in reinforced concrete structures subjected to flexion, when the stress in the tension area surpasses the resistance of the concrete, cracks are formed, this is denominated “flexural cracking”, and which are identifiable by their cross-section direction to the main reinforcement of the beam. This is inevitable, whether or not there are corrosion problems. Furthermore, if the reinforcement are undergoing corrosion the cracking area is aggravated, as when both effects are present there is cracking due to flexion and corrosion.

Due to the fact that the products of corrosion possess a greater volume than the material from which they are derived, they generate internal pressure that cause part of these products to fill the pores of the concrete and to exit to the exterior through the flexural cracks (if there are any). As the corrosion advances and with the saturation of the pores, the oxides produce tensions that, when they surpass the rupture tensile stress of the concrete, it cracks in a longitudinal direction. These are known as “cracks by corrosion”. It is necessary to clarify that the division between cracking by flexion and by corrosion is not a very well defined concept, given that as the corrosion process evolves the progress of both of them becomes interrelated—possibly mutually strengthening each other. This difference in the direction of the cracks is what allows them to be classified in such a fashion.

The presence of flexural cracks (when the load is of a sufficient magnitude as to create them) accelerates the penetration of oxygen, water, and chlorides towards the reinforcement, thus favoring the corrosion process of the same (contributing to the increase of the cracking areas due to corrosion). On the other hand, by decreasing the section of the bars due to corrosion, the internal balance of the section causes an increase in the number of flexural cracks. Furthermore, with the flexural cracks being an exit to the exterior, a part of the corrosion products can grow in thickness and longitude which could increase even

more the areas with flexural cracks. That is to say, the total growth of cracking implies a decrease of the resistant section of the beam (due to the section decline of the reinforcement and of the mechanically useful section of the concrete), so that, in the case of there being loads close to the breaking loads of the element, it could lead to the collapse of the structure as was the case with beam V96 at 140 days into the test.

The cracks were measured from the moment the external loads were placed. Figure 5 shows the evolution of the total cracking areas in each beam; that is to say, those obtained from the sum of the flex cracking areas, plus the areas of cracking by corrosion (in the same direction as the main reinforcement of the beam). It is worth remembering that the so-called cracking area is the sum of the products of the longitude by the width of each crack.

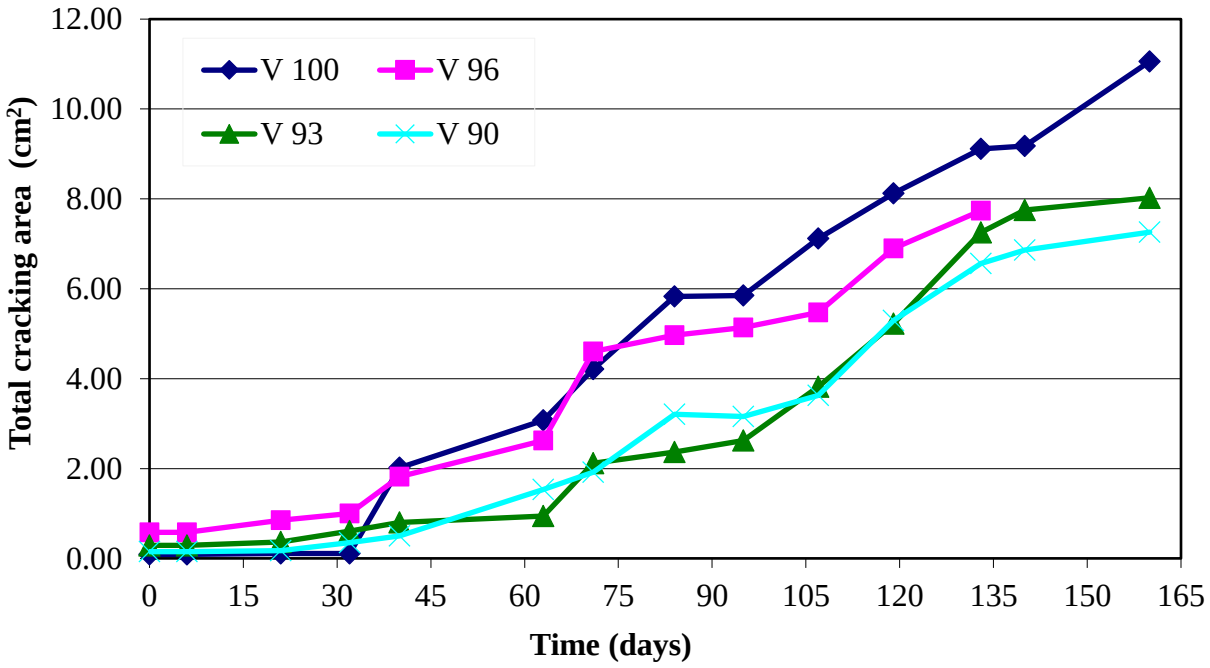

Figure 5. Total cracking area in terms of time

As predicted, the start of the cracking by corrosion manifested later on the beams with greater coating. Beams V90 and V93 had a similar evolution of the total cracking area throughout the duration of the test, taking into account the degree of dispersion that normally appears in most experimental works; whereas beams V96 and V100 showed a differentiated behavior, with total cracking areas greater than those of the remaining beams, this is due to having a lower r/ϕ ratio of the reinforcement. However, if the flexural cracking area is analyzed separately (Figure 6), it can be observed that beam V96 showed higher values than the rest. This can be clearly observed with the state this beam reached, in which the deterioration by corruption presented itself to a greater extent in the area of the flexural cracks, whereas the rest of the beams showed a more generalized cracking. Evidently, this greater initial cracking due to flexion was a significant means of entry for the chlorides that reached all the way to the reinforcement, with beam V96 showing the largest total cracking area s (Figure 5) during the first 30 days of the test, after which their behavior was within the expected.

This behavior observed in beam V96 explains its collapse prior to that of beam V100. However, this evidences the influence of the lesser r/ϕ ratio of beam V100, which, having the least flexural cracking

during almost the entirety of the test, presented greater cracking by corrosion than the rest; as well as the importance that flexural cracking has in the deterioration of a structure subjected to corrosion, as is the case of beam V96.

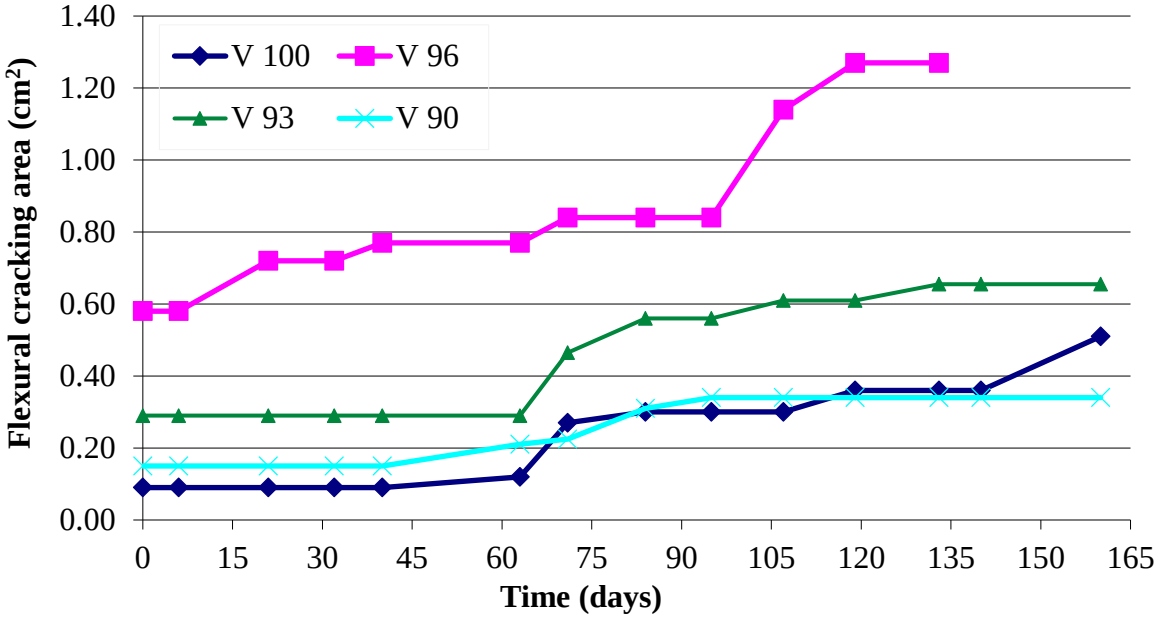

Figure 6. Flexural cracking area in terms of time

In this work, we analyze the behavior of beams with a different r/ϕ ratio of their reinforcement, which are subjected to the same stress generated by external loads, in light of a corrosion process. A comparison can be made on the observed evolution of the cracking of the coating, with that obtained in other works carried out by the same research group (Moro, 2012) on beams made with concretes of similar qualities as the ones in this work, elaborated with or without recycled concrete aggregates and subjected to the same corrosive process, but without the application of external loads. In this case, the standard beam (without recycled aggregate) has a r/ϕ ratio of 2.4 and is, therefore, comparable with beam V100 of this work. By carrying out a regression analysis of the total cracking areas in both beams, it can be observed that the slope is greater in V100 (y = 0.074 x -0.9502) than in the standard beam without external loads (y = 0.068 x -0.7688). This is due to the fact that the tensile stress in the bars of V100 causes flexural cracks, which facilitate the entry of aggressive agents from the exterior, causing an acceleration of the corrosion process.

It can be observed in Figure 7 that the appearance of the first visible cracks due to corrosion is delayed (the average depth of the attack is proportional to the time, expression (1)) as the thickness of the coating increases (greater r/ϕ ratio). The increase in the thickness of the coating causes a delay in the appearance of the first cracks due to corrosion (Figure 7), as well as slowing their evolution (see Figure 5) due to the fact that the aggressive external elements (chlorides, oxygen, and water) take longer to reach the reinforcement. This situation, in the case of the tensile reinforcement with lower r/ϕ ratios, is worrying due to the fact that this greater depth of attack on the bars, with less external symptoms (cracking), encloses a significant risk because it decreases the warning time in case of a structural collapse—more worrying still if there are chlorides that cause pitting. In Figure 7, a point corresponding to the standard beam (without external loads and a r/ϕ ratio = 2.4) of the aforementioned work (Moro, 2012) was incorporated, where it can be observed that a greater depth of attack is necessary for the appearance of the first visible cracks.

The equation in Figure 7 obtained through a regression analysis (y = a + b x) can be compared with the one obtained in other researches (Alonso, 1998) where concretes made with water/cement ratios between 0.52 and 0.65 were used, while the rest of the test conditions are similar, among which the following stand out: a slightly broader variance range of the coating/diameter ratio than the one adopted in this paper, in both works the abutments were placed, and the same current intensity was utilized. The results achieved in the cited work were: a = 7.53 and b = 9.32, with R^2 = 0.92. The slope of this line is much lower than the one obtained in this work (a= 13.71), therefore, it could be said that in structures subjected to external laws, the degradation generated by the corrosion of its reinforcement is accelerated, even for cements made with a water/cement ratio somewhat lower to that of the reference.

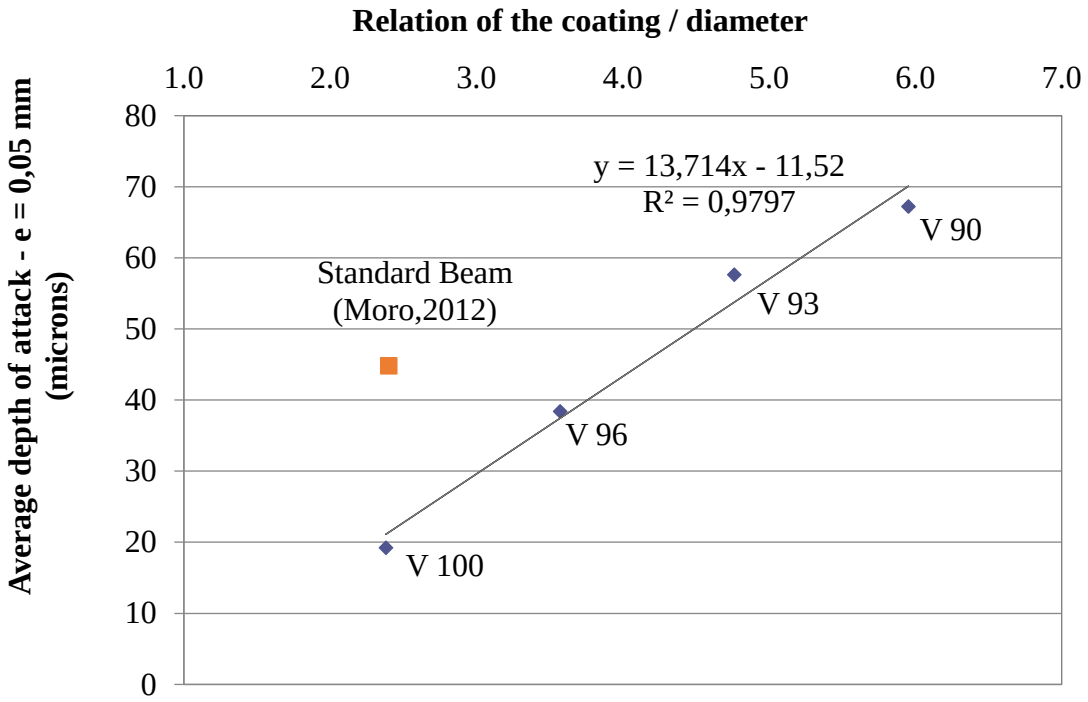

Figure 7. Relation between the average depth of attack on the reinforcement that produced the first visible crack (e = 0.05 mm) due to corrosion, and the relation of the coating / diameter of the bar.

Once the test was finalized, the reinforcement was uncovered by removing the coating. In the visual inspection of the same, it could be observed that, due to the action of the chlorides (in spite of the low concentration adopted), the corrosion on the bars was, in general, not uniform. Rather, some areas of localized corrosion (pitting) could be observed, with no particular pattern. However, in some cases more pitting was found in areas close to the flexural cracks, as was the case of beam V96, in which the collapse section coincided with a flexural crack.

3.4 Follow-up of the maximum cracking width

Figure 8 shows the variation of the maximum cracking width in terms of time. It can be observed that the maximum cracking width, during the greater part of the test, was superior on beam V96 due to the influence of the flexural cracking. No great differences were observed in the evolution of the rest of the beams, which was due to the fact that the distribution of the cracking was developed differently on each beam, whether in a more generalized or localized manner, without generating evident differences between the different samples tested.

If the evolution of the maximum cracking width is compared with that of the cracking areas (Figure 5), it can be observed that the latter are a more representative indicator of the general evolution of the deterioration, due to the fact that it is common for the maximum width to vary in its location on the beam throughout the corrosion process. Furthermore, it tends to evolve in jumps in terms of the emergence of new cracks that cause the redistribution of the internal stress in the coating. For example, Figure 8 shows that beam V90 has the most cracking between days 40 and 90, when in reality it ought to be the one with the lesser values. This situation was also found in other works (Aveldaño, 2009; Aveldaño, 2013). Nevertheless, this figure is included due to the fact that it is common to introduce limitations on the maximum width of the cracks in the standards, and therefore it is used as a reference in many international bibliographies. It is worth noting that it would be necessary to carry out research to standardize the cracking area, so that valid comparisons between various deteriorated beams could be carried out, for example, in terms of the length of the affected element or the length of the corroded area, to later establish representative deterioration indicators and then limit it.

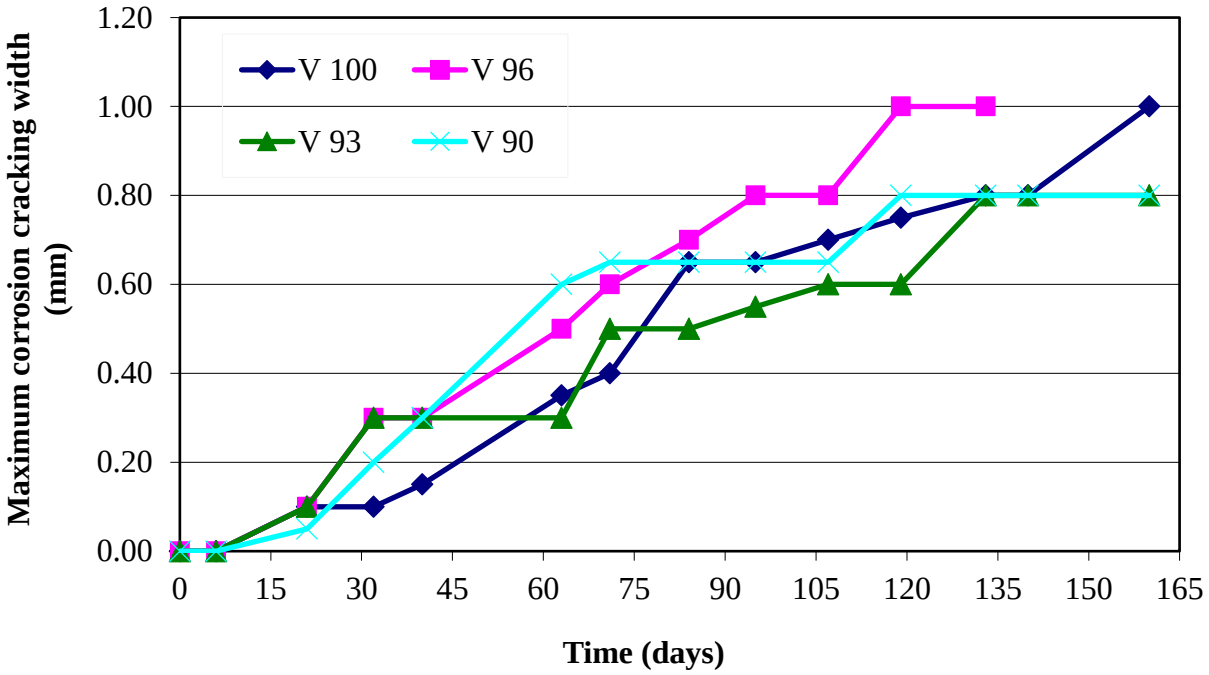

Figure 8. Maximum cracking width in terms of time

4. CONCLUSIONS

In this experimental work, it was found that the deterioration of beams exposed to external loads, due to the corrosion of its reinforcement, was greater than if said loads were not present and that the thickness of the coating influences this process; all of which affects the residual life and the bearing capacity of the affected structure. In particular, it was proven that:

– In loaded beams with tensile reinforcement affected by accelerated corrosion, as the concrete coating / diameter of the reinforcement increases the longer it took for the first cracks to appear due to corrosion and their evolution became slower, evidencing the total cracking areas. The protection effect generated by greater coating makes the aggressive elements that come from the exterior (chlorides, oxygen, water) to require more time to reach the reinforcement, reducing the speed of the process;

- The cracks of the concrete coating, caused by the flexion produced by external loads, favored the increase of cracking due to the corrosion of the reinforcement, thus increasing the total cracking and, therefore, influencing the subsequent degradation of the structure.

From a practical point of view, the aforementioned conclusions allow us to determine that in loaded reinforced concrete structures located in aggressive environments, it is worth it to decrease flexural cracking caused by the service loads as much as possible; as well as increase the ratio of the coating / diameter of the reinforcement in order to decrease the effects of corrosion in the same.

5. ACKNOWLEDGEMENTS

The authors would like to thank Ph.D. Carla Priano, engineer Lilia Señas, and the technicians J.P. Gorordo of the Laboratory of Structural Models and D. Smith of the Laboratory of Material Study and Testing, U.N.S., for their collaboration in the development of the tests. Furthermore, we thank the General Ministry of Science and Technology and the Engineering department of the Universidad Nacional del Sur for their financial and institutional support in the realization of these researches.

6. REFERENCES

Almusallam, A. A., Al-Gahtani, A. S., Aziz, A. R. (1996), "*Effect of reinforcement corrosion on bond strength*", Construction and Building Materials, V. 10, No. 2, pp. 123-129.

Alonso, M. C., Andrade, C., Rodríguez, J., Diez, J. M. (1998), "*Factors controlling cracking in concrete affected by reinforcement corrosion*", Materials and Structures, Nr. 31, pp. 435-445.

Alonso, M. C., Andrade, M. C., Rodríguez, J., Casal, J., García, M. (1994), "*Evaluación experimental de la fisuración del hormigón producida por la corrosión de las armaduras*", Hormigón y Acero, No. 194, pp. 29-42.

Al-Sulaimani, J., Kaleemullah, M., Basunbul, I. A., Rasheeduzafar (1990), "*Influence on corrosion and cracking on bond behaviour and strength of reinforced concrete members*", ACI Structural Journal, V. 87, Nr 2, pp. 220-231.

American Society for Testing and Materials: ASTM C876, "*Standard test method for half cell potential of reinforcing steel in concrete*", Philadelphia, U.S.A, (1980).

Andrade, M. C., Alonso, M. C., Molina, F. J. (1993), "*Cover cracking as a function of bar corrosion: Part I – Experimental test*", Materials and Structures, Nr. 26, pp. 453-464.

Aveldaño, R. R., Ortega, N. F. (2009), "*Influence of reinforcement distribution in the corrosive process of reinforced concrete beams*", Magazine of Concrete Research, Thomas Telford, V. 61, Nr. 3, pp. 213-220.

Aveldaño, R. R., Ortega, N. F. (2011), "*Characterization of Concrete Cracking due to Corrosion of Reinforcements in Different Environments*", Construction and Building Materials, V.25, pp.630-37.

Aveldaño, R. R., Ortega, N. F. (2013), "*Behavior of concrete elements subjected to corrosion in their compressed or tensed reinforcement*", Construction and Building Materials, Nr. 38, pp. 822–828.

Calabrese, L., Campanella, G., Proverbio, E. (2013), "*Identification of corrosion mechanisms by univariate and multivariate statistical analysis during long term acoustic emission monitoring on a pre-stressed concrete beam*", Corrosion Science, V. 73, pp. 161-171.

Elfergani, H. A., Rhys, P., Holford, K. M. (2013), "*Damage assessment of corrosion in prestressed concrete by acoustic emission*", Construction and Building Materials, V. 40, pp. 925–933.

Fumin, L., Yingshu, Y., Chun-Qing, L. (2011), "*Corrosion propagation of prestressing steel strands in concrete subject to chloride attack*", Construction and Building Materials, V. 25, Nr.

10, pp. 3878-3885.

Hariche, L., Ballim, Y., Bouhicha, M. Kenai, S. (2012), "*Effects of reinforcement configuration and sustained load on the behaviour of reinforced concrete beams affected by reinforcing steel corrosion*", Cement and Concrete Composites, V. 34, Nr. 10, pp. 1202–1209.

Instituto Argentino de Normalización y Certificación IRAM 1627: "*Agregados. Granulometría de los agregados para hormigón*", Buenos Aires, (1997).

Instituto Argentino de Racionalización de Materiales – Instituto Argentino de Siderurgia, Norma U 500-528: "*Barras de acero conformadas de dureza natural, para armadura en estructuras de hormigón*", Buenos Aires, (1989).

Instituto Argentino de Normalización y Certificación IRAM 1871: "*Método de ensayo para determinar la capacidad y la velocidad de succión capilar de agua del hormigón endurecido*", Buenos Aires, (2005).

Instituto Argentino de Normalización y Certificación IRAM 1546: "*Hormigón de cemento portland. Método de ensayo de compresión*", Buenos Aires, (1992).

Instituto Argentino de Normalización y Certificación IRAM 1658: Hormigón. "*Método de ensayo de tracción simple por compresión diametral*", Buenos Aires, (1995).

Instituto Argentino de Normalización y Certificación IRAM 1534: "*Hormigón de cemento portland. Preparación y curado de probetas para ensayos en laboratorio*", Buenos Aires, (1985).

Malumbela, G., Moyo, P., Alexander, M., (2009), "*Behaviour of RC beams under sustained service loads*", Construction and Building Materials, V. 23, Nr. 11, pp. 3346–3351.

Melchers, R. (2001), "*Assessment of existing structures, approaches and research needs*", Journal of Structural Engineering, ASCE, pp. 406-411.

Moro, J. M., Meneses, R. S., Ortega, N. F., Aveldaño, R.R., Señas, L., Priano C. V. (2012), "*Corrosión de Armaduras en Estructuras de Hormigón Reciclado con Tratamientos Previos*", CINPAR 2012, VIII Congreso Internacional sobre Patología y Recuperación de Estructuras, 11 páginas.

Ortega, N. F., Alonso, M. C., Andrade, M. C., López, C. (2001), "*Análisis de la fisuración ocasionada por la corrosión de las armaduras activas de elementos pretensados*", Coloquia, Madrid.

Peralta, M. H., Rivas, I. E., Ortega, N. F. (2006), "*Análisis Numérico de la Fisuración Superficial de Estructuras de Hormigón Armado por Efecto de la Corrosión*", Informes de la Construcción, V. 58, No. 501, pp. 51-58.

Rodríguez, J., Ortega, L. M., Casal, J., Vidal, M. A. (1993), "*Disminución de la adherencia entre hormigón y barras corrugadas debido a la corrosión*", Hormigón y Acero, No 189, pp. 49-65.

Rodríguez, J., Ortega, L. M., García, A. M. (1993), "*Medida de la velocidad de corrosión de las armaduras en estructuras de hormigón, mediante un equipo desarrollado dentro del proyecto Eureka EU* 401", Hormigón y Acero, No. 189, pp. 79-91.

Rodríguez, J., Ortega Basagoiti, L. M., Casal, J., Diez, J. M. (1996), "*Comportamiento estructural de vigas de hormigón con armaduras corroídas*", Hormigón y Acero, No. 200, pp.113-131.

Rodríguez, J., Ortega Basagoiti, L. M., Casal, J., Diez, J. M. (1998), "*La corrosión de armaduras y la vida residual de las estructuras de hormigón*", Hormigón y Acero, No. 208, pp. 63-78.

Schierloh M. I. (2003)., "Corrosión de armaduras. Características que debe tener el hormigón para aumentar la protección", Tesis de Magíster en Ingeniería, Departamento de Ingeniería, Universidad Nacional del Sur, Director de Tesis: Ortega N.F.

Schierloh M. I., Ortega N. F., Señas L. N. (2001), "*Relación entre Algunas Propiedades del Hormigón del Recubrimiento y el Proceso Corrosivo de las Armaduras*", 14° Reunión de Asociación Argentina de Tecnología del Hormigón, pp. 125-132.

Torres-Acosta, A. A., Navarro-Gutierrez, S., Terán-Guillén, J. (2007), "*Residual flexure capacity of corroded reinforced concrete beams*", Engineering Structures, V. 29, Nr. 6, pp. 1145-1152.

Tuutti K. (1982); "*Corrosion of steel in concrete*", Swedish Cement and Concrete Institute (CIB) pp. 4-82, Stockholm, Sweden

Yu, L., François, R., Dang, V. H., L'Hostis, V., Gagné, R., "*Development of chloride-induced corrosion in pre-cracked RC beams under sustained loading: Effect of load-induced cracks, concrete cover, and exposure conditions*", Cement & Concrete Research, Nº67, 2015, pp.246-258.

ALCONPAT Journal, Volume 6, Issue 2, may – august 2016, Pages 145 – 156

ALCONPAT Journal

www.revistaalconpat.org

eISSN 2007-6835

Journal of the Latin-American Association of Quality Control, Pathology and Recovery of Construction

Evaluation of pathological manifestations in buildings in terms of geographical orientation

W. Mazer[1], L. M. R. Silva[2], E. Lucas[3], F. C. M. Santos[4].

[1] Profesor do Departamento Académico de Construcción Civil da UTFPR – Campus Curitiba.
[2] Arquitecta da Estruktor Patología das Construcciones.
[3] Tecnóloga en Concreto.
[4] Tecnóloga en Concreto da Estruktor Patología das Construcciones.

Article information
DOI:
http://dx.doi.org/10.21041/ra.v6i2.135
Article received on December 16th 2016, reviewed under publishing policies of ALCONPAT journal and accepted on April 12th 2016. Any discussion, including the replica of the authors, shall be published in the first number of the year 2017 as long as the information is received prior to the closing of the third number of the year 2016.

Legal Information

ALCONPAT Journal, Year 6, No. 2, May – August 2016, is a quarterly publication of the Latin American Association of Quality Control, Pathology and Construction Recovery, International, A.C., Km. 6, Old Highway to Progreso, Mérida, Yucatán, Zip Code 97310, Tel. +52 1 (999) 738-5893, alconpat.int@gmail.com, Website: www.alconpat.org
Responsible Editor: Dr. Pedro Castro Borges. No. 04-2013-011717330300-203, eISSN 2007-6835, both granted by the National Institute of Copyright. Responsible for the last update of this number, Informatics Unit ALCONPAT, Elizabeth Sabido Maldonado, Km. 6, Old Highway to Progreso, Mérida, Yucatán, Zip Code 97310, publication date: May 30, 2016.

ABSTRACT

In order to evaluate the incidence of pathological manifestations on the facades of buildings, correlated with the geographical location, 52 buildings for residential and commercial use were analyzed in this study; these were distributed in different parts of the city of Curitiba, Brazil. It was observed that all the buildings evaluated had some type of pathological manifestation, and 25 of these were present on the facades of the buildings. It was found that the pathological manifestations on the facades show up in different amounts and locations, having identified a relation with the variation of temperature and the direction of the wind in terms of geographical orientation.

Keywords: durability; facade; geographical location; pathological manifestation.

RESUMEN

Con el propósito de evaluar la incidencia de manifestaciones patológicas en fachadas de edificios, correlacionadas con la dirección geográfica, se analizaron en este estudio 52 edificios de uso residencial y comercial distribuidos en varias partes de la ciudad de Curitiba – Brasil. Se observó que todos los edificios evaluados tuvieron algún tipo de manifestación patológica, y 25 de éstas en las fachadas. Se encontró que las manifestaciones patológicas en fachadas aparecen en diferentes cantidades y direcciones, habiéndose identificado una relación con la variación de la temperatura y la dirección del viento en función de la orientación geográfica.

Palabras clave: durabilidad; fachada; dirección geográfica; manifestación patológica.

RESUMO

Com a finalidade de avaliar a incidência de manifestações patológicas em fachadas de edifícios, correlacionando com as direções geográficas, neste trabalho foram analisados 52 edifícios de uso residencial e comercial distribuídos em diversas regiões da cidade de Curitiba – Brasil. Foi observado que todos os edifícios vistoriados apresentaram algum tipo de manifestação patológica, sendo que 25 apresentaram problemas nas fachadas. Verificou-se que as manifestações patológicas nas fachadas aparecem em quantidades diferentes nas diferentes direções, tendo sido identificada uma relação com a variação de temperatura e com a direção dos ventos, conforme a direção geográfica.

Palavras chave: durabilidade; fachadas; direção geográfica; manifestações patológicas.

Corresponding author: Wellington Mazer (wmazer@utfpr.edu.br)

1. INTRODUCTION

Civil construction interacts with the occurrence of pathological manifestations in its projects, which is due to a variety of reasons. According to the Evaluation method indicated by the ASTM E632-82 (1996), which analyzes the durability of the constructions, there are different factors that influence the buildings and which can be divided in five different groups, according to their nature: atmospheric, biological, load, incompatibility, and use factors, as can be seen in Figure 1.

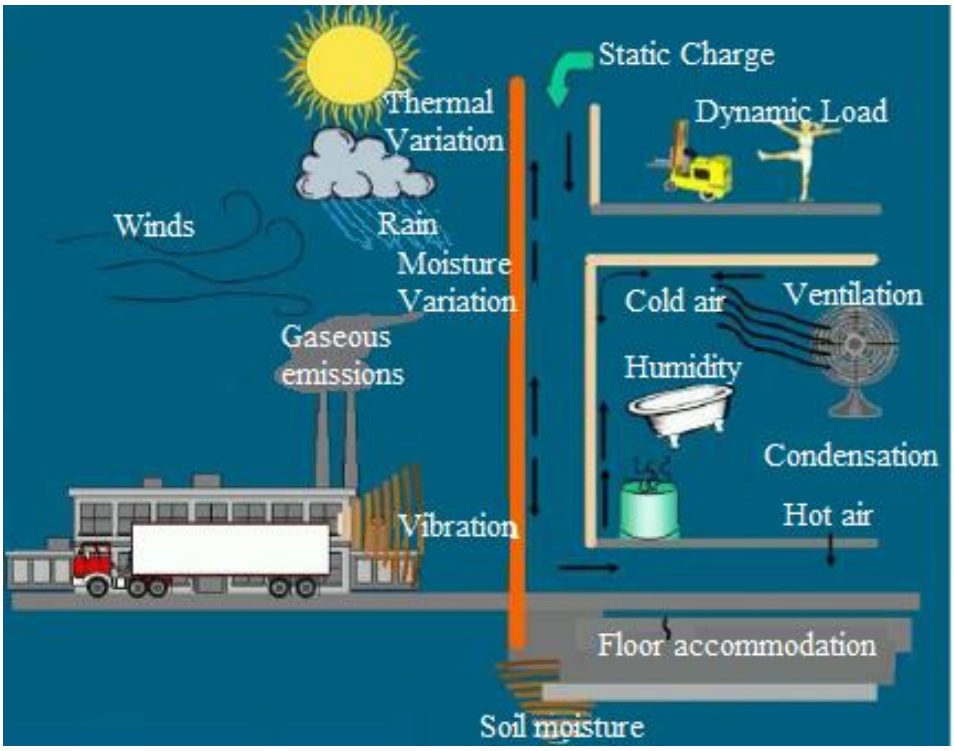

Figure 1. Degradation factors that have an impact on the facades (Source: Antunes, 2010).

The atmospheric factors are defined as the group of factors associated to the environment, which include the temperature, solar radiation, air pollutants, and the humidity caused by rain, snow or ice. Such factors always act on the edifications and could present a series of variations with regard to the seasons of the year and the geographical location of the development. The variation of the temperature can cause a dimensional variation on the material (dilation or contraction) (Resende, Barros and Campos, 2001).
The biological agents are characterized mainly by mushrooms or small types of vegetation that need special conditions to develop, such as: temperatures between 10°C and 35°C, elevated relative humidity, the presence of nitrogen, phosphorus, carbon and in less amounts, iron, calcium, chlorine, magnesium, among other chemical components (Shirakawa, 1995). This confirms that the presence of water, in any state, is fundamental for the development of these organisms and makes the facades of building as one of the most ideal locations for their emergence.
The load factors can be represented by the physical action of rain and wind on the facade of the buildings.
The incompatibility factors can present themselves due to a type of chemical or physical divergence; the chemistry may happen due to differences in the chemical composition of base and coating materials, or due to the erroneous addition of a material such as gypsum in the mortar and the physics when a coating provides unsustainable loads to the base or substrate, causing displacements.

Finally, the factors of use are determined by the direct influence of the users of the edification on the materials that comprise the building during the entire useful life of the project, execution, use, operation, and maintenance. (Resende, Barros and Campos, 2001).

According to Barros and Sabbatini (2001), the most frequent pathological problems are: the formation of humidity stains, with the development of mold, splintering and displacement between layers of frieze and the gypsum, and the formation of fissures and cracks.

One of the widely researched factors is the atmospheric action on the facades. Romero et al. (2011) studied the *Torre Colpatria*, in Colombia, and observed the existence of cracking, carbonation, and the attack of sulphates on the facades of the building being studied, relating the damages observed to factors such as the height at which the damage happened, the geographical orientation of the facade, and the predominant direction of the wind and rain. Lembo (2011) studied three building in the region of the Basilicata, where he verified the influence of the relief around the construction and the predominant direction of the wind, having confirmed, mainly, problems of infiltration and ventilation.

Melo and Carasek (2014) verified the existence of a relation between the predominant direction of the rain and the stains that showed on the facade of historical buildings. The authors also verified the existence of stains due to microbiological action, influenced by solar radiation.

Among the different pathological manifestations found on the facades of buildings, Galletto and Andrello (2013) observed that the main incidences are fissures, followed by stains and the separation of the ceramic coatings, both in new and old buildings. The authors believe that the fissures that are present in the system of joints, caused by thermal and humidity variations, could have had an influence on the emergence of the other damages. These same damages were observed by Abreu et al. (2013), who studied facades that were coated with ceramic elements and paint.

The splintering of the coatings was studied by Japiassú et al. (2014), who analyzed the interface between mortar and ceramic on the facades of buildings from the 19th and 20th centuries. They confirmed that the adherence between these materials directly influences the splintering of these, having a great relation between the diameter of the aggregates and the ceramic pieces.

Several authors (Melo and Carasek, 2014; Galletto and Andrello, 2013) verified the influence of some environmental parameters such a solar radiation, the direction of rain, thermal and humidity variations on the incidence of pathological manifestations, as these factors may vary in intensity according to the geographical location of the facade of a building, generating a greater incidence of damage on some facades.

In this context, the objective of this work is to verify the main pathological manifestations on facades of residential and commercial buildings on Curitiba/Paraná and to correlate them with their geographical location.

2. METHODOLOGICAL PROCEDURES

The development of this research took place in the city of Curitiba, situated on the first plateau of the state of Paraná, at an approximate altitude of 950 m and at 100 km from the coast, and was divided in two stages. The first stage comprised a sample of 52 buildings from the city with locations that are indicated in Figure 2, with ages between 1 and 50 years of construction. The height of the buildings varied between 4 and 23 floors, understanding that 31 of the buildings have 1 basement, 5 have 2 basements, and the other 16 do not have basements. The buildings are mostly located on the central region of the city and in urban developments, where there is a high concentration of buildings.

The evaluation of all the buildings used in this research was due to the wish of a company that specializes in the elaboration of inspection reports. In this stage, the main existing pathological manifestations in the buildings were identified. The inspections were carried out in the common areas of the buildings, notably in the basements, first floor, water tanks, roofs, and on the four facades of each building. Visual

inspections were done in the common areas, with photographic records and the measurements of the thickness of the cracks; on the facades, a visual inspection was done, using preemption techniques on the critical regions with safety covers or slings to be able to go around the facade, detecting cracks, coating displacements, efflorescence, and filtrations.

Figure 2. Location of the buildings inspected.

In the second stage, the 25 facades of the buildings of the initial sample that presented pathological manifestations were inspected, relating the facades of the buildings with the geographical position in order to verify if there was any relation between the pathological manifestations and the geographical position. These 25 buildings have heights that vary from 9 to 22 floors. The buildings that do not have problems on the facades were ruled out during this stage. The regions used in the second stage of the investigations are indicated in Figure 3, where the buildings that do present failures on their facades are located.

a) Central region of the city.

b) Region of the urban areas of Bigorrilho and Mercês.

c) Region of the urban area of Água Verde.

Figure 3. Location of the regions from the second stage of the study.

From the data observed in the inspections of the buildings, the objective was to verify the greater incidences of anomalies and the possibility to associate the pathological manifestations of the facades of the buildings with the geographical location.

3. RESULTS AND ANALYSIS

In the 52 buildings initially inspected, according to the abovementioned procedures, the main pathological manifestations observed are indicated in Figure 4:

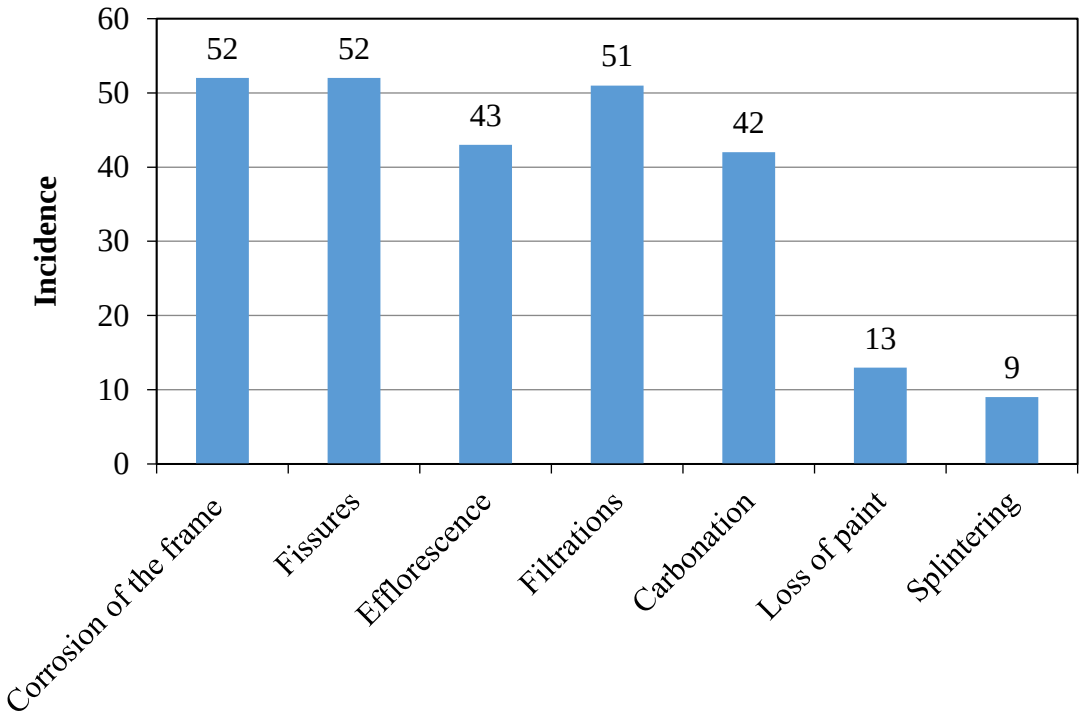

Figure 4. Occurrence of pathological manifestations.

With an incidence of 100% on the condominiums inspected, the corrosion of the frame is the pathological manifestation of higher frequency in terms of having several causative agents, such as filtrations, a lack of coating on the frame, exposure to environments heavy in chlorides (water tanks), among other causes. The second anomaly with higher incidence were the fissures, which also represent a manifestation that is caused by different factors such as: thermal dilation, lack of supports, lintels or beams, caused by corrosion, among others. After fissures, the third anomaly with greater incidence is filtration, followed by the efflorescence and carbonation of the structures. From the failures that were analyzed, the ones with a greater incidence are those that exist on the facades of the buildings, such as the loss of paint, generally considered as splintering.

In Figure 5, it is possible to verify the incidence of anomalies related to the constructive region of the building and that, in this case, anomalies on the facade of approximatery 50% of the buildings evaluated were observed, indicating that it is not only splintering that is related to this problem, as can be seen below:

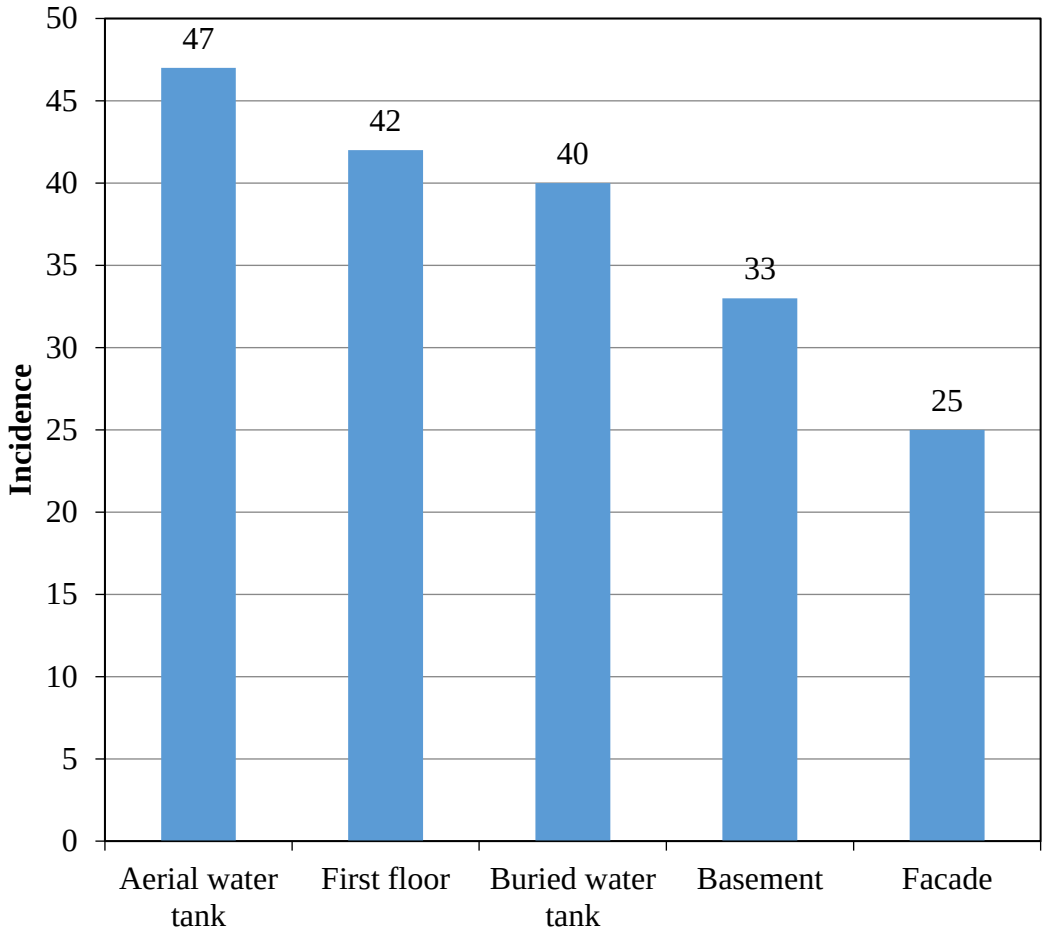

Figure 5. Location of the pathological manifestations.

It can be observed in Figure 5 that the facades of the buildings have a lower incidence of pathological manifestations, occurring in 48% of the buildings that were inspected, that is, in 25 buildings. Despite the lower incidence, the pathological manifestations may be observed on the facades and they are presented in Table 1.

Table 1 – Incidence of pathological manifestations on facades.

Pathological manifestation	**Number of incidents on the facade.**
Fissures	25
Efflorescence	14
Splintering	22
Filtrations	7

The incidence percentages of pathological manifestations on the facades of the buildings that were inspected are presented in Table 2, divided according to the geographical location in which they were observed.

Table 2 – Incidence percentages of manifestations in each geographical location.

Geographical Location	Fissures	Efflorescence	Splintering	Filtrations
North	40.0	28.6	31.8	0.0
South	16.0	14.3	22.7	14.3
East	16.0	28.6	18.2	57.1
West	28.0	28.6	27.3	28.6

In Table 1 we can appreciate that in all buildings that presented pathological manifestations on their facades, the incidence of fissures was also present; it was seen that the largest portion of the fissures, as indicated in Table 2, happen on the facades that face North, which, in Curitiba, receives the most solar incidence, and which can suffer a variation in temperature of up to 10°C in the same day, as indicated in Figure 7. Some examples of these incidences are shown in Figure 6. Most of the time, splintering also occurs in the same facades as the variation in temperature, in addition to failures in the execution of the building, also have an influence on this type of damage.

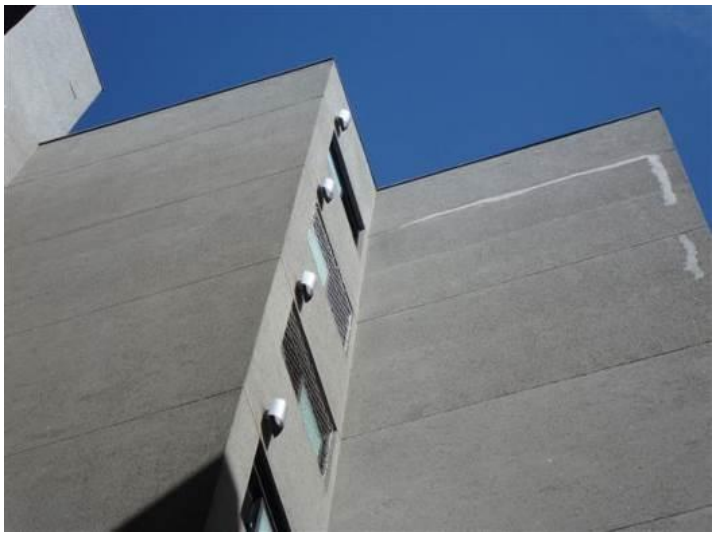

a) Thermal variation fissures.

b) Structure movement fissures.

Figure 6. Fissures on the facade.

The efflorescence presented in 56% of the buildings with pathological manifestations in the facades, appear in less amounts in the southern region, which possesses a lower incidence of wind and rain. In the other geographical regions, the percentage of incidences was the same making it impossible to establish a correlation between this manifestation and the geographical location.

The filtrations, which are present in 28% of the buildings, appear in lower amounts on the east face of the buildings, which is a direction with a great incidence of wind and rain. In Figure 8, we show a map of the predominant direction of the winds in the region, showing that the East region is the one with the most incidences, conducting the rain to this direction as well and thus justifying the higher incidence of filtrations in this region.

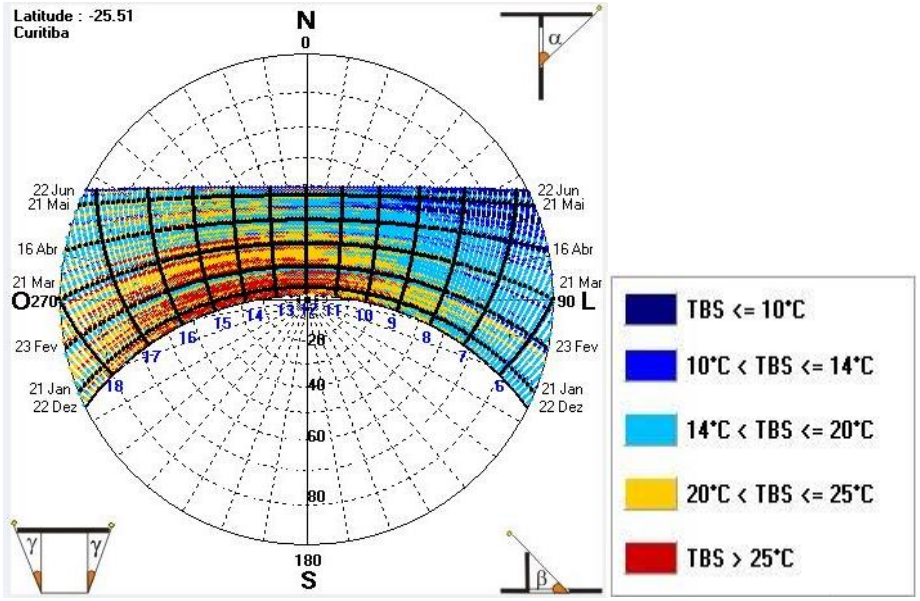

a) Temperatures from december to june.

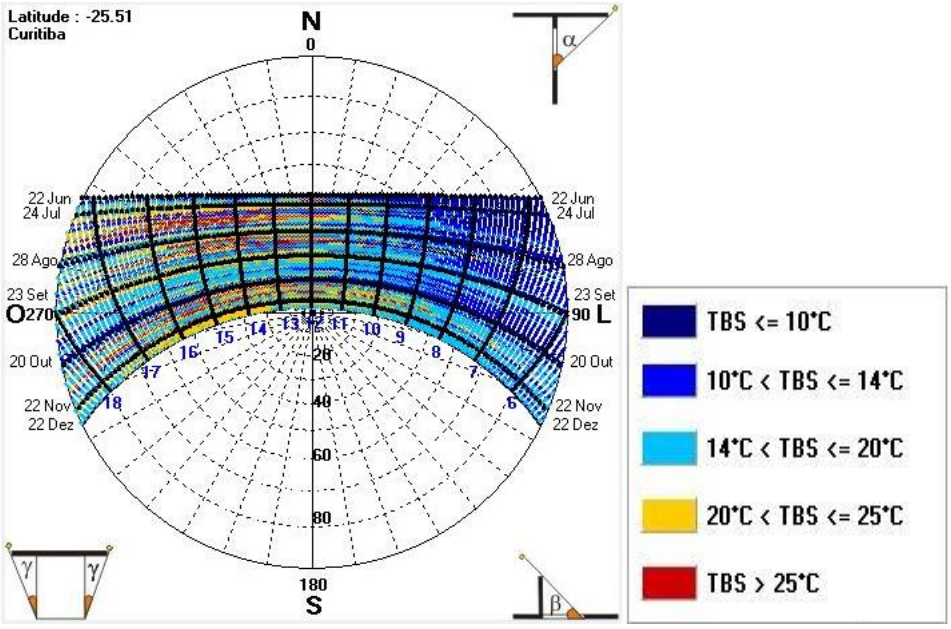

b) Temperatures from june to december.

Figure 7. Average temperatures in Curitiba.

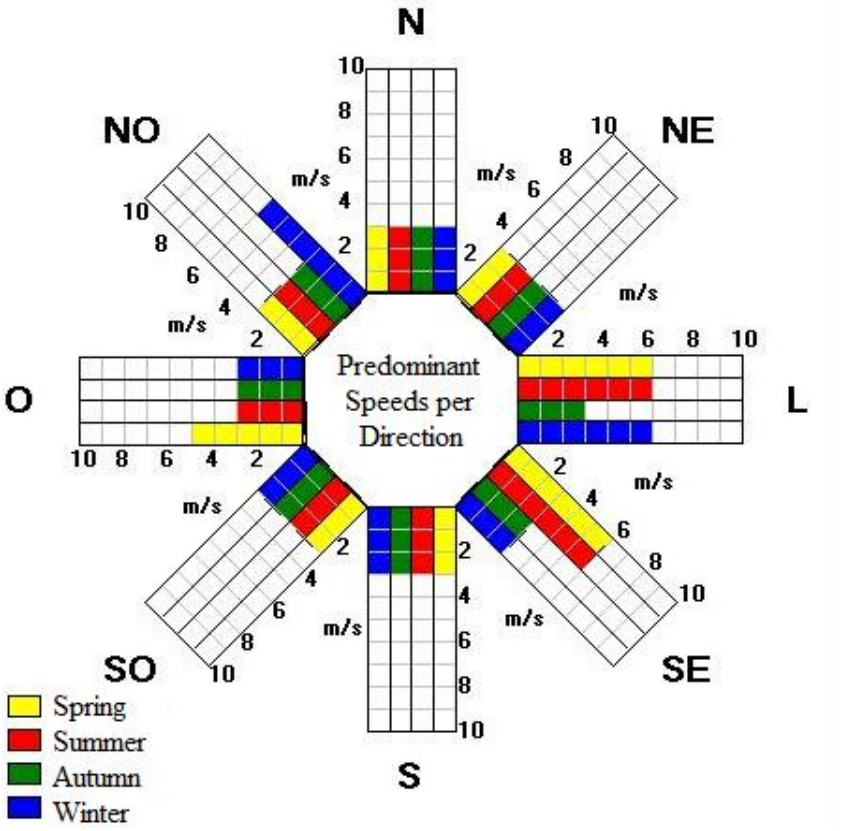

a) Wind speed.

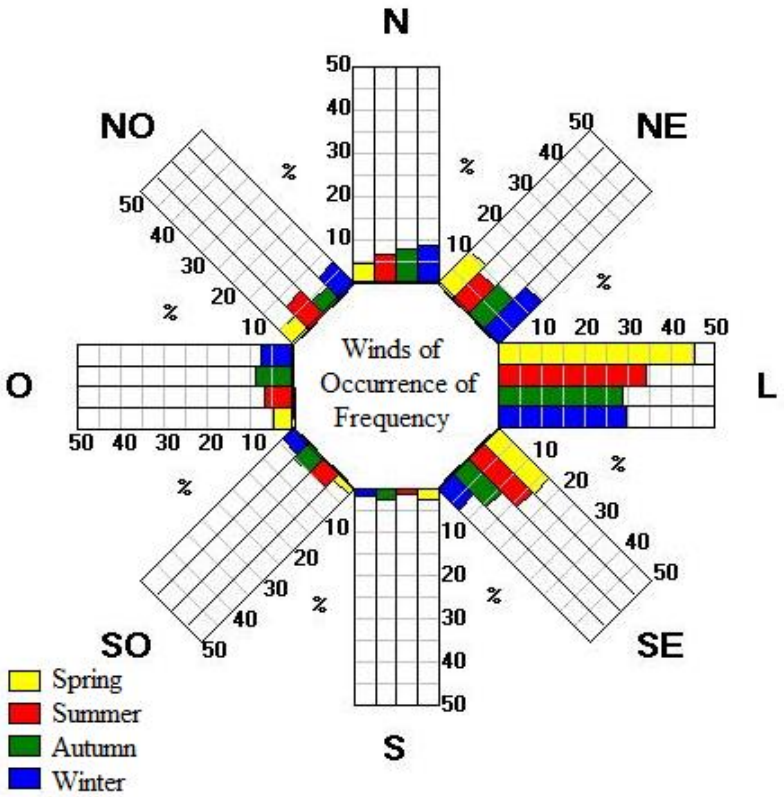

b) Frequency of the winds.

Figure 8. Incidence of winds in Curitiba.

In Figure 7, the numbering from 6 to 18 represents the hours of the day in which the solar incidence occurs on a facade that faces North, and the data is sometimes from random days chosen to be cited on the solar chart. For example, in Figure 6a, we can observe that the temperature at 6:00h in the morning of december 22nd appears to be between 14°C and 20°C and at 13:00h, the temperature is above 25°C. In Figure 8, the speed and percentage of incidences of the wind in the different geographical directions and seasons of the year are indicated.
From the flaws observed on the buildings, the ones that stand out the most are the corrosion of the frames that appeared in 100% of the buildings analyzed and the fissures that are also present in 100% of the buildings that have this problem on their facades.

4. CONCLUSIONS

From the 52 cases that were analyzed, it was observed that the main pathological manifestations were corrosion on the frames and fissures on all of them, in addition to filtrations in 98% of the buildings, efflorescence in 83%, and carbonation in 81%. The loss of paint and splintering on the facades appeared with a lower incidence of 25% and 17%, respectively.
Pathological manifestations on facades show up on 25 of the 52 buildings that were inspected, observing fissures on 25 of the facades, a loss of paint or splintering on 22 facades, efflorescence on 14, and filtrations on 7 facades of the buildings.
The geographical location with the highest solar incidence presented the most pathological manifestations, with fissures and splintering as the most common; this indicates a probable relation between this geographical location and the types of damages.
The greatest presence of filtrations is seen on the facades that face towards the geographical direction with a higher wind speed and incidence, indicating a probable relation between these factors and the incidence of filtrations.
In spite of the existing indications between the geographical locations and the incidence of pathological manifestations, it is necessary to consider the environmental factors such as solar incidence, variations in temperature, and the predominant directions of the wind and rain in order to establish correlations between geographical location and pathological manifestations.

5. ACKNOWLEDGEMENTS

The authors would like to thank the Estruktor Patología das Construcciones Ltda company for carrying out the inspections and providing the information necessary for the elaboration of this study.

6. REFERENCES

Abreu, D. W. M., Lins, A. M. T., Silva, M. S., Farias, M. B. S. (2013), "*Patologias no revestimento de fachadas dos edifícios históricos da cidade de Campina Grande*", In: 5º. EnPAC, Campina Grande (PB).
American Society for Testing and Materials. ASTM – E 632-81. *Standard recommended practice for developing short-term accelerated test for prediction of the service life of building components and materials,* Philadelphia, 1996.
Antunes, G. R. (2010), "*Estudo de manifestações patológicas de fachadas em Brasília – Sistematização da incidência de casos*", Dissertação de mestrado. UNB.
Barros, M. M. S. B.; Sabbatini, F. H. (2001), "*Produção de revestimentos cerâmicos para paredes de vedação em alvenaria: Diretrizes básicas*", (São Paulo, Brasil: EPUSP).

Galletto, A., Andrello, J. M. (2013), "*Patologia em fachadas com revestimentos cerâmicos*", In: CINPAR – IX Congresso Internacional sobre patología y recuperación de estruturas, João Pessoa (Brasil).

Japiassú, J., Carasek, H., Cascudo, O., Velosa, A. L. (2014), "*Caracterização da interface azulejo/argamassa de fachadas históricas*", Revista ALCONPAT, V. 4, No. 1, pp. 55-76.

Lembo, F. (2011), "*Pathologies of industrialized building made by bearing precast concrete panels. The case study of intervention with the same building system at Chiaromonte, Francavilla in Sinni and Lagonegro*", In: XII DBMC – International Conference on durability of Building Materials and Components, Porto (Portugal).

Melo, C. M., Carasek, H. (2014), "*Relationship between the deterioration of multi-story building facades and driving rain*", Revista de la Construcción, V. 13, No. 1, pp. 64-73.

Resende, M. M.; Barros, M. M. S. B.; Campos, J. S. (2001), "*A influência da manutenção na durabilidade dos revestimentos de fachada de edifícios*", In: Workdur - II Workshop sobre durabilidade das construcciones, São José dos Campos (Brasil), pp. 144-154.

Romero, N., Dupuy, C., Quiñones, J. (2011), "*Influencia de la contaminación atmosférica en la fachada de rascacielos, caso Torre Colpatria*", Revista ALCONPAT, V. 1, No. 3, pp. 228-235.

Shirakawa, M. A. (1995), "*Identificação de fungos em revestimentos de argamassa com bolor evidente*", In: I Simpósio Brasileiro de Tecnologia das Argamassas, Goiânia (Brasil), pp.402-10.

ALCONPAT Journal, Volume 6, Issue 2, may – august 2016, Pages 157 – 172

ALCONPAT Journal

www.revistaalconpat.org

eISSN 2007-6835

Journal of the Latin-American Association of Quality Control, Pathology and Recovery of Construction

Fire resistance of pultruded profiles of glass fiber reinforced polymer (GFRP) for rehabilitation applications: experimental, numeric, and analytical study

T. Morgado[1], J. R. Correia[2], N. Silvestre[3], F. Branco[2]

[1] CERIS, Instituto Superior Técnico, Universidad de Lisboa, Portugal.
[2] CERIS, Instituto Superior Técnico, Universidad de Lisboa, Portugal.
[3] LAETA, Instituto Superior Técnico, Universidad de Lisboa, Portugal.

Article information
DOI:
http://dx.doi.org/10.21041/ra.v6i2.136
Article received on December 29th 2015, reviewed under publishing policies of ALCONPAT journal and accepted on April 01st 2016. Any discussion, including the replica of the authors, shall be published in the first number of the year 2017 as long as the information is received prior to the closing of the third number of the year 2016.

Legal Information

ALCONPAT Journal, Year 6, No. 2, May – August 2016, is a quarterly publication of the Latin American Association of Quality Control, Pathology and Construction Recovery, International, A.C., Km. 6, Old Highway to Progreso, Mérida, Yucatán, Zip Code 97310, Tel. +52 1 (999) 738-5893, alconpat.int@gmail.com, Website: www.alconpat.org
Responsible Editor: Dr. Pedro Castro Borges. Responsible for the last update of this number, Informatics Unit ALCONPAT, Elizabeth Sabido Maldonado, Km. 6, Old Highway to Progreso, Mérida, Yucatán, Zip Code 97310, publication date: May 30, 2016.

ABSTRACT

This paper presents a study about the fire behaviour of glass fibre reinforced polymer (GFRP) pultruded beams. Fire resistance tests were carried out in beams with a span of 1.3 m, exposed to fire according to the time-temperature curve defined in the ISO 834 standard. In these tests the effects of different types of fire exposure (one and three sides) and load levels, as well as the efficacy of different fire protection systems were evaluated. In order to study the evolution of temperature distributions during the fire resistance tests, a two-dimensional numerical model was developed using the commercial software *ANSYS FLUENT*. Also an analytical model was developed to estimate the mechanical response of the beams during fire exposure.
Keywords: composite materials; fire behaviour; experimental campaign; numerical simulation; analytical model.

RESUMEN

El presente artículo presenta un estudio sobre la resistencia al fuego de vigas fabricadas con perfiles pultrusionados de polímero reforzado con fibra de vidrio (GFRP). Se realizaron ensayos de resistencia al fuego en vigas con un vano de 1.3 m, expuestas a la acción del fuego según la norma ISO 834. En estos ensayos, se evaluó el efecto de diferentes tipos de exposición al fuego y los niveles de carga aplicados, así como la eficacia de diferentes sistemas de protección. Se desarrolló un modelo numérico en el software *ANSYS FLUENT* para simular la evolución del campo de temperaturas en la sección transversal y un modelo analítico para determinar la evolución de la deformación de las vigas.
Palabras clave: materiales compuestos; resistencia al fuego; campaña experimental; simulación numérica; modelo analítico.

RESUMO

Neste artigo é apresentado um estudo sobre a resistência ao fogo de vigas em perfis pultrudidos de polímero reforçado com fibras de vidro (GFRP). Foram realizados ensaios de resistência ao fogo em vigas com um vão de 1.3 m, expostas ao fogo de acordo com a curva temperatura-tempo da norma ISO 834. Nestes ensaios, avaliou-se o efeito de diferentes tipos de exposição ao fogo (em uma e três faces) e níveis de carga aplicados, bem como a eficácia de diferentes sistemas de proteção. Foi desenvolvido um modelo numérico térmico bidimensional no *software ANSYS FLUENT* para simular a evolução das distribuições de temperatura na secção transversal. Foi ainda desenvolvido um modelo analítico para determinar a evolução das deformações das vigas.
Palavras-chave: materiais compósitos; resistência ao fogo; campanha experimental; simulação numérica; modelo analítico.

Corresponding author: Tiago Morgado (tiago.m.r.morgado@ist.utl.pt)

1. INTRODUCTION

The use of Fiber Reinforced Polymers (FRP) is increasing each day for applications in civil engineering as they bring along different advantages in relation to the materials that are traditionally used in this sector, among which are the reduced weight, high resistance, good thermal isolation properties, reduced maintenance fees, and excellent durability. Despite having a fragile behavior and a high deformability, these composite materials present a deficient behavior to fire, which considerably limits their practical application, especially in buildings (Correia, 2012).

When the FRP are exposed to moderately high temperatures (100-200 ºC), they soften and their mechanical properties (rigidity and resistance) are considerably reduced. When the materials are exposed to high temperatures (300-500 ºC), the polymeric matrix decomposes, releasing heat, smoke, soot, and toxic volatile gases (Correia, 2004). Presently, type-E glass fibers are most commonly used for the reinforcement of FRP (80-90% of commercial products) (Samanta *et al.*, 2004). These fibers start softening and become viscous at temperatures close to 830 ºC, presenting a melting point of around 1070 ºC (Mouritz *et al.*, 2006). In this manner, the polymeric matrix is what essentially conditions the behavior of the FRP at high temperatures.

The mechanical properties (rigidity and resistance) in the compression and cutting of the GFRP material (more dependent on the matrix) are more affected by the increase of temperature than the traction properties (which are more dependent on the fibers) (Correia *et al.*, 2013), which results in the collapse of beams with GFRP to occur usually due to compression and/or cutting and not due to traction. Regarding the behavior of beams with GRFP to fire, Ludwig *et al.* (2008) carried out fire resistance tests on beams with an I-section (IPE 120 and IPE 160 profiles) exposed to fire in four stages. Similarly, Correia *et al.* (2010) evaluated the performance of GFRP beams with a tubular square section for an exposure to fire of just one stage. In both studies, the composite beams were comprised by a polymeric matrix with a polyester resin and by type-E glass fibers, which were exposed to fire according to the fire curve pattern defined in the ISO 834 (1999) standard. In both experimental procedures, different systems of fire protection were studied.

In this article, we present a study on the behavior to fire on beams with pultruded profiles of GFRP. The main objective of the experimental program that was developed was to evaluate the resistance to fire of the GFRP beams in terms of the type of exposure to fire and the two levels of load that are applied, evaluating the efficiency of different protection systems. With the objective to simulate the evolution of the temperatures in the GFRP section that is subject to a fire situation, a bi-dimensional model was developed using the commercial *software ANSYS FLUENT* (ANSYS, 2012), in which the changes in heat by conduction, radiation, and convection were considered accounting for the air in the interior of the cavity of the section. Simultaneously, an analytical model was also developed, through which the evolution of the arrow in the middle of the span of a GFRP beam was estimated throughout the study.

2. EXPERIMENTAL STUDY

2.1 Experimental procedure

In the fire resistance tests, the pultruded GFRP, with a square tubular section (100×100×8 mm), produced by the *Fiberline* company, was evaluated. This material is comprised by rovings of type-E glass fibers in the central zone of the laminations and by two layers of continuous stand mats positioned randomly, which surround that central layer of the lamination. The compound is comprised of 69% inorganic material and the glass fibers are embedded by a polyester resin matrix. Dynamic Mechanical Analysis (DMA) tests were done on the GFRP material, which showed that its vitreous transition temperature (T_g, determined through the mean point of the curve of the storage module) is of 140 ºC. Differential Scanning

Calorimetry and thermogravimetric analysis (DSC/TGA) tests were done, where the decomposition temperature (T_d) of the material at approximately 370 ºC was determined (Morgado *et al.*, 2013).
To increase the fire resistance of the GFRP beams analyzed, six different protection systems were implemented. The protection materials used in this experimental procedure were the following: plates of cork agglomerate (CA), from the *Robcork* company (25 mm in thickness); Plates of Rock Wool (RW), facilitated by the *Rockwool* company (25 mm in thickness); plates of calcium silicate (CS), manufactured by the *Promatec* company (H type, 25 mm in thickness); absorbent blanket (MI), delivered by *Technical Fibre Products* (Tecnofire 60853A, 2 mm in thickness); and absorbent dye (TI), from *CIN* (C-THERM HB, 2 mm in thickness). An active protection system through water cooling (AA) was also used, which consists on sheet of water 8 mm thick on the lower part, with a flow rate of 0.4 m^3/h. The protection plans applied are shown in Figure 1.

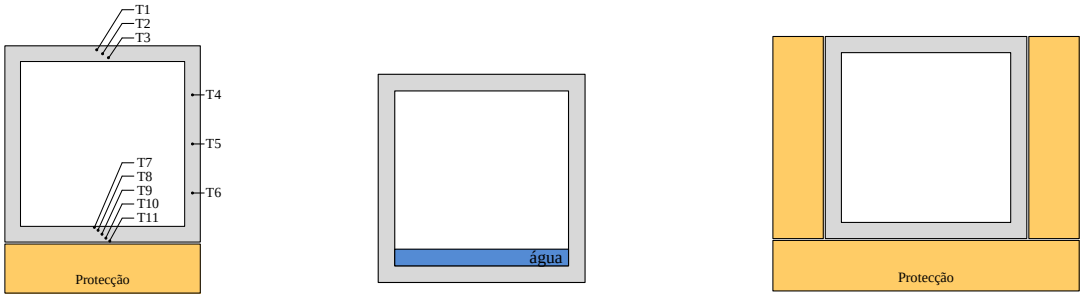

Figure 1. (a) Beams with passive protection exposed to one face (indicating the position of the thermocouples); (b) beams with active protection exposed to a third of the face(s); and (c) beam with passive protection exposed on the three faces.

In this experimental procedure, 12 beams with a square tubular section were tested; they were grouped into three experimental series. In the S1series, the beams were exposed to fire on just one face (E1F) and subject to a service load equivalent to one arrow in the middle of the span of L/400 (room temperature). In the S2 series, the beams were exposed to fire on the three faces (E3F) and were subject to a load that was equal to that of the first series. In the S3 series, the beams were also exposed to the fire on just one face, being subject to a load equivalent to one arrow in the middle of the span of L/250 (also the room temperature). It is also important to point out that a non-protected (NP) beam was tested in each of the series, as presented on Table 1.

Table 1. Experimental Procedure.

Series	Number of beams	Designation of the beams	Exposure to fire	Applied Strength [kN]
S1	7	NP-S1, AC-S1, LR-S1, SC-S1, MI-S1, TI-S1, AA-S1	E1F	11.7
S2	3	NP-S2, SC-S2, AA-S2	E3F	11.7
S3	2	NP-S3, SC-S3	E1F	18.7

The fire resistance tests were done in a vertical gas furnace (Figure 2a), with external dimensions of 1.35×1.20×2.10 m (length × width × height), that has an open space on top allowing the test of horizontal elements. These tests were done by adopting the fire curve pattern defined on the standard ISO 834 (1999), presented in Figure 3c. In the S1 and S3 series, the GFRP beams were exposed to fire on only one face, whereas in the series S2, the beams were exposed to fire on three faces, as illustrated in Figure

1b. The different types of exposure to fire were obtained through a system of covers, comprised of different modules that allow the exposure to fire on one or three faces. The beams were tested in terms of flexion on four points with the free span between supports of 1.3 m, applying different loads in accordance with the experimental series. As illustrated in Figure 2a, the weights used for loading the beams were materialized through concrete elements and cement bags.

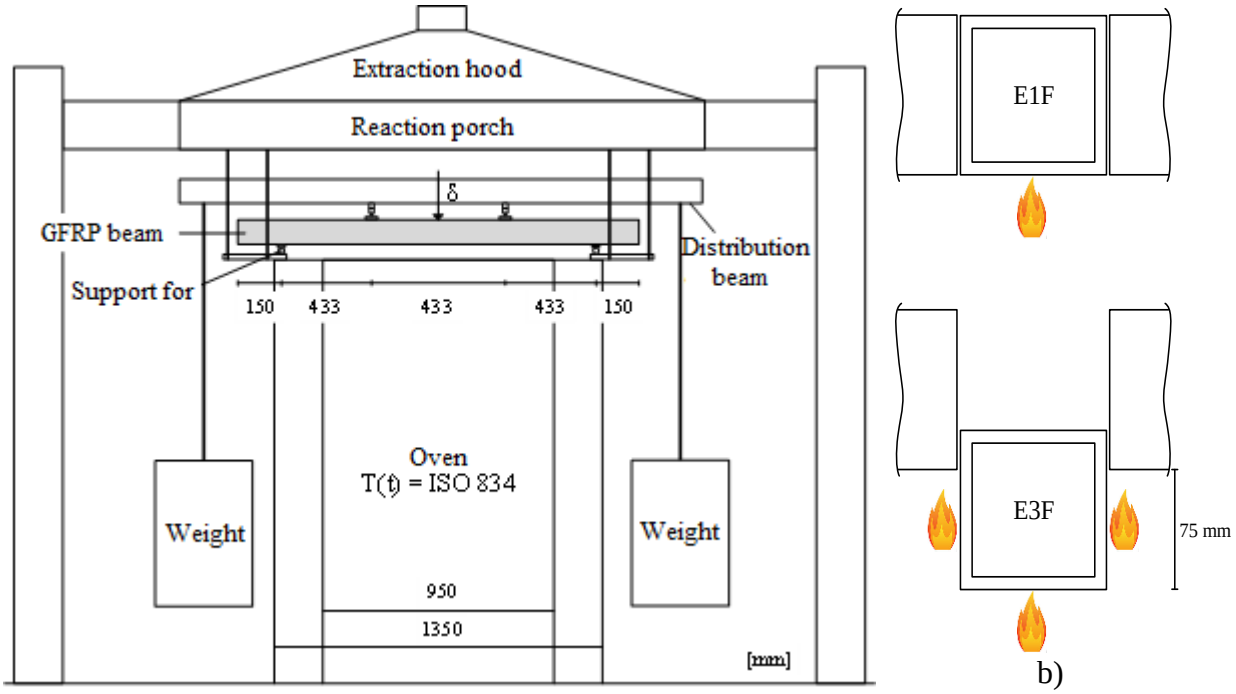

Figure 2. (a) E-test plan and (b) types of expositions tested, on one face (on) and on the three faces (below).

The GFRP beams were instrumented with type K thermocouples, through which it was possible to register the temperatures in the cross-section in the middle of the span, installing three thermocouples on the above face (T1-T3), three thermocouples in the web (T4-T6), and five thermocouples on the face (T7-T11). The positioning of the thermocouples installed on the upper and lower faces was done to obtain the evolution of the temperatures along the length of the width of the walls. As for the position of the thermocouples that were installed on the webs, they were placed to allowed the evaluation of the temperatures throughout the web as illustrated in Figure 1a. After the placement of the thermocouples in the planned positions, the corresponding protection systems were implemented. In the middle of the span of the GFRP beams, a thread deflectometer of the *TML* brand (model CDP-500) was fixed, through which the evolution of the arrows of the beams was monitored.

2.2 Results and discussion

To evaluate the temperatures observed in the different fire resistance tests, the temperatures at medium height of the upper face (T2), of the web (T5), and of the lower face (T9) were observed. Figure 3 shows the evolution of the temperatures registered on the beams of the S1 series. As expected, the implementation of fire protection allowed the improvement of the thermal performance of the GFRP beams, *i.e.*, it helped delay the heating of the cross-section. In fact, the implementation of protections helped significantly reduce the temperatures in comparison to the non-protected beam (NP-S1); the efficiency of cork, rock wool, and calcium silicate agglomerate protections, as well as cooling with water stand out, with this last system being the most efficient in protecting the web and the upper face. It is

important to point out that, in the S1 series, the collapse of the beams took place when the average temperature of the upper face was close to the vitreous transition temperature (T_g) of the GFRP material (Figure 3a).

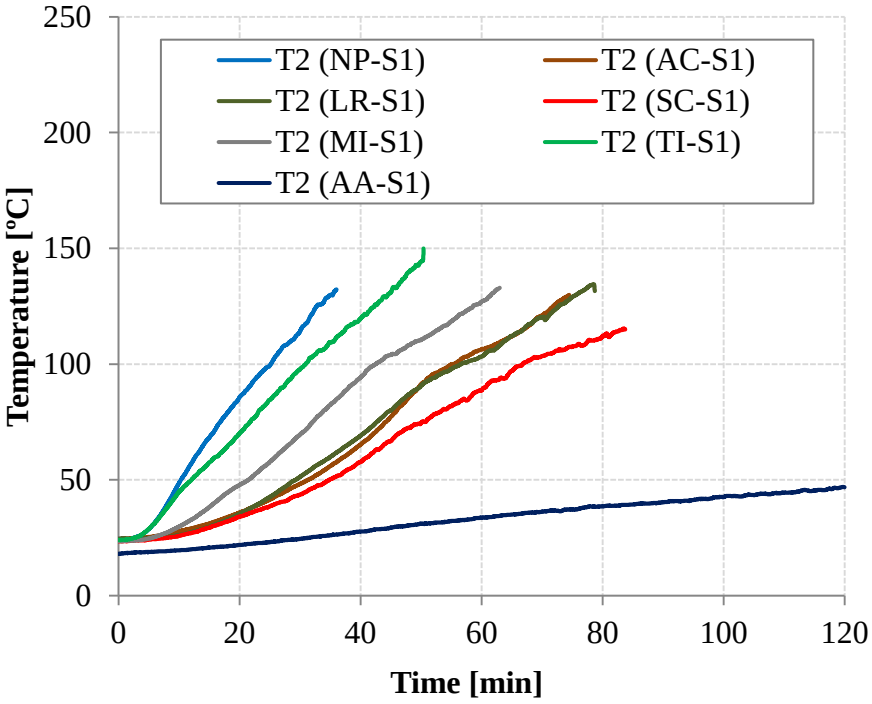

(a) In the middle of the lower face

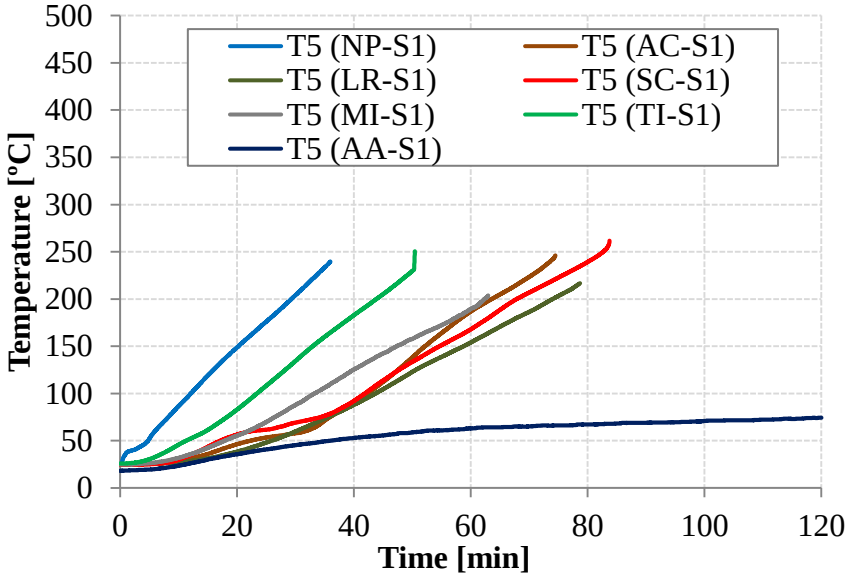

(b) At mid-height of the web

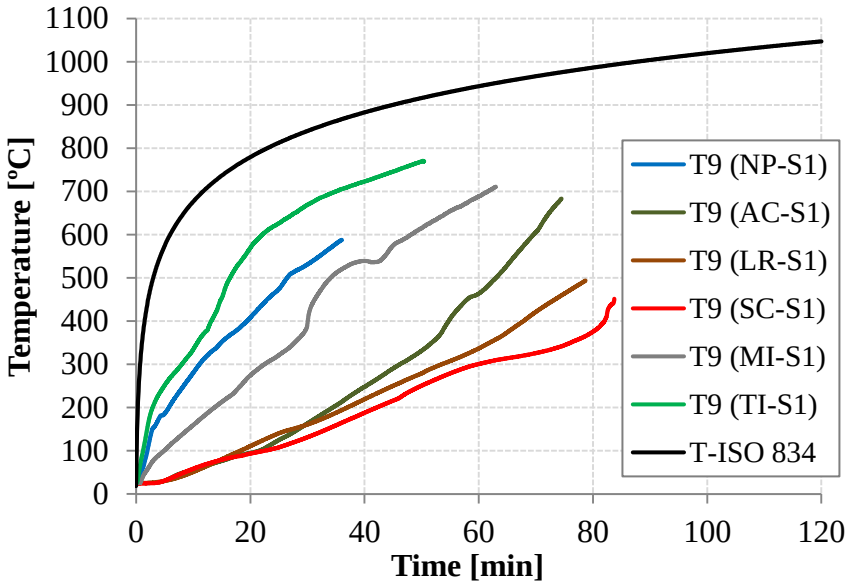

(c) In the middle of the lower face of the beams of the S1 series

Figure 3. Thermal response: temperatures.

Figure 4 presents the comparison of the evolution of the temperatures on the non-protected and protected beams with calcium silicate of the S1 and S2 series (in the case of NP beams, the values presented were measured in auxiliary profiles, not subject to any load; the temperatures measured on the AA-S2 beam are not presented, as the duration of this test was too short). In the case of the beams of the S2 series, the fact of the temperature evolution curves of the webs and that the lower faces are so similar stands out, which is consistent with the type of fire exposure of these beams (three faces). As in the S1 series, the passive protection with calcium silicate allowed reducing the temperatures in a significant manner. In the beams of the S3 series, as expected, the evolution of the temperatures was very similar to the one recorded in the S1 series, which was due to the thermal exposure being identical (one face).

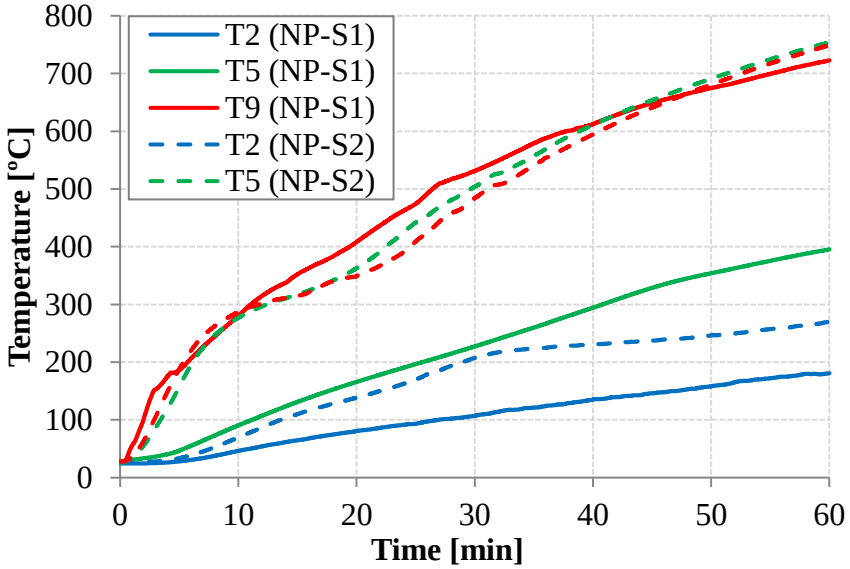

(a) In the NP-S1 and NP-S2 beams.

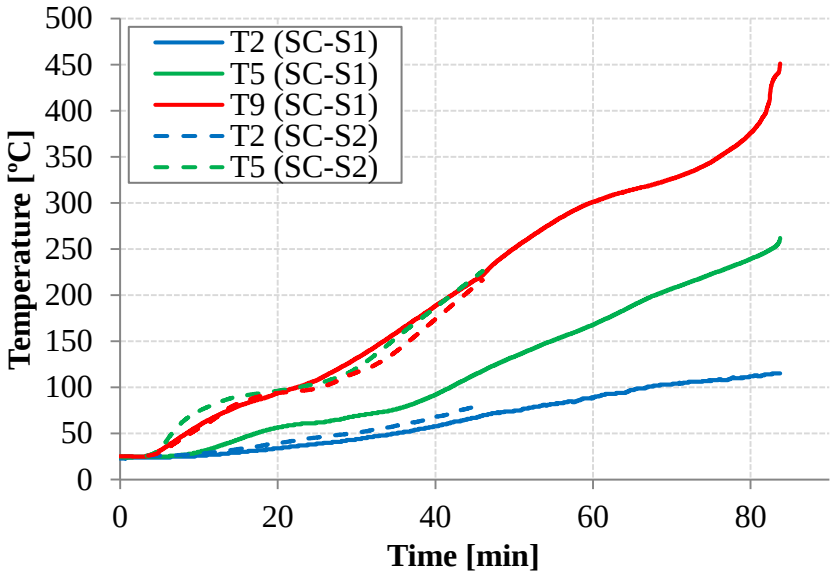

(b) In the SC-S1 and SC-S2 beams.

Figure 4. Thermal response: temperatures recorded.

Figure 5a shows the variation on the displacements in the middle of the span of the beams of the S1 series, in terms of the test duration. In the beams without passive protection, a rapid increase of the arrow in the middle of the span was seen during the initial instants; which is be related to the fast degradation of the mechanical properties of the lower face. After this initial phase, the range of deformation in these beams decreased, staying reasonably constant until the end of the test—a height at which it increased again in an increasing tendency. In the beams with passive protection, the increase of deformation with time (which varies for the different protections) was less marked, which is naturally associated to a slow and gradual heating of the cross-section and, consequently, resulting in a lower reduction of the mechanical properties of the GFRP material. In the case of the beam with active protection, despite the initial increase of deformation being relatively fast (which is associated to the fact that the lower face does not have any protection), after a certain height, a estabilization of the evolution of the arrow in the middle of the span was verified, which presented a very reduced growth rate until the end of the exposure to fire. Figure 5b shows the comparison between the variation of the displacements in the middle of the span of the beams of the S1 series with the S2 and S3 series. As expected for the same type beams, the exposure to three faces (S2 series) and the increase of the load (S3 series),caused greater increases in the deformations.

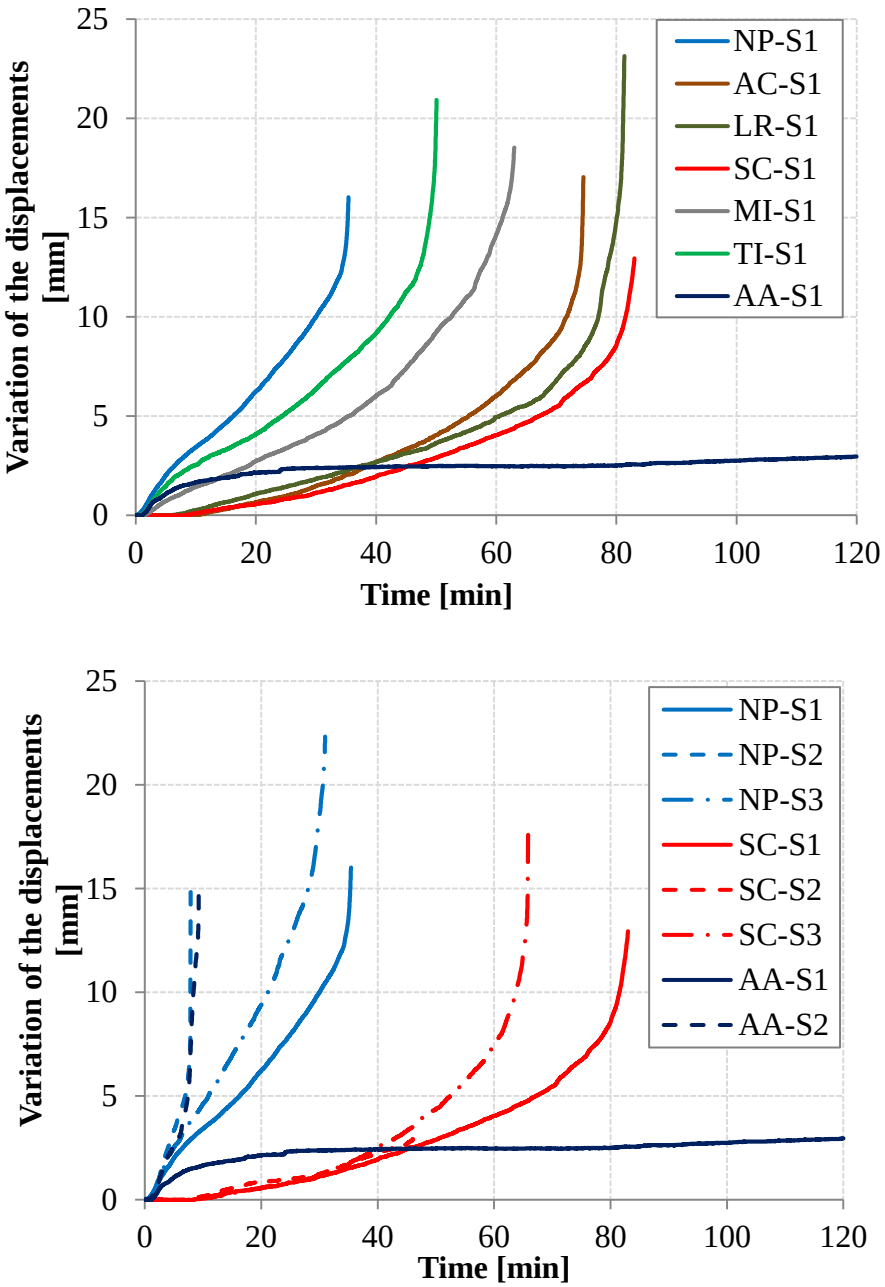

Figure 5. Mechanical response: variation of the displacements recorded in the middle of the span of the beams (a) of the S1 series and (b) of the S1, S2, and S3 series, non-protected (NP), with calcium silicate (CS) and cooled with water (AA).

In relation to the manner of breakage, all beams collapsed in a fragile manner and without any signs of pre-breaking. The general portions of the beams collapsed due to the longitudinal compression of the upper part in the central zone and/or due to transversal compression and the cutting of the webs over one of the load application points, as illustrated in Figure 6. The beams of the S2 series (exposed to fire on three faces), non-protected and cooled with water, seem to have collapsed due to the cutting/instability of the webs, which presented a very significant arching throughout their entire height. In addition, it is indicated that the beam cooled with water and exposed to fire on the lower face (AA-S1) did not collapse for 120 minutes, point at which the test was interrupted. In Figure 7, a comparison between the fire resistance times of the different beams is presented, highlighting (i) the efficiency of the different

protection systems and the reduction of the fire resistance caused (ii) by the exposure on three faces, and especially for the system cooled with water (the efficiency of which is drastically decreased), and (iii) by the increase of the load.

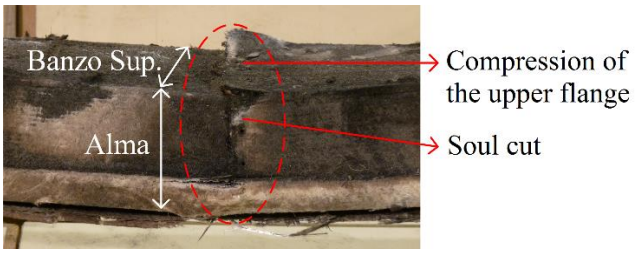

Figure 6. Typical manner of breakage in the tested beams.

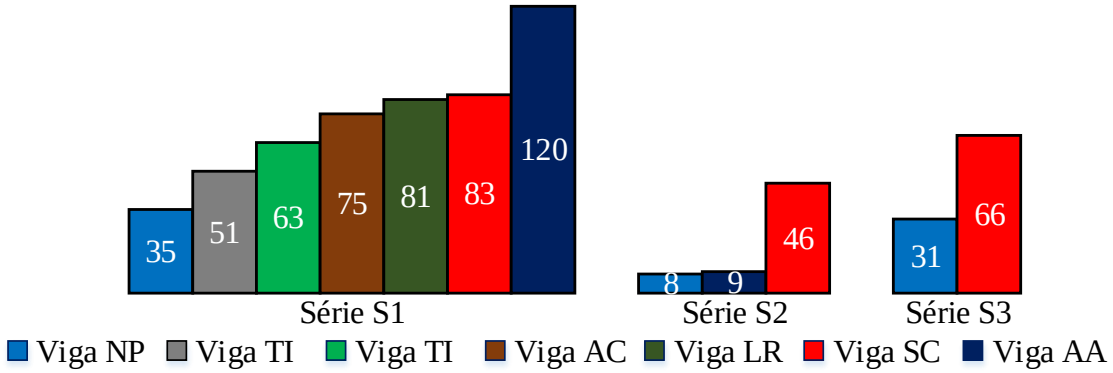

Figure 7. fire resistance (in minutes) of the tested beams.

3. NUMERIC STUDY

3.1 Numeric model

With the intention of simulating the fire resistance tests that were carried out, a bi-dimensional thermal model was developed, using the commercial *software ANSYS FLUENT* (ANSYS, 2012), to simulate the evolution of the temperatures on the exposed tubular section beam exposed to fire on one face and not protected (NP-S1 beam). In the model developed (Figure 8a) the following hypotheses were considered: (i) the furnace transfers heat to the lower part of the profile through radiation ($\varepsilon = 0.70$) and convection ($h = 25$ W/m^2); (ii) the transfer of heat in the profile occurs through conduction in the GFRP material, as well as through internal radiation ($\varepsilon = 0.75$) between the faces of the cavity of the profile and through the convection of the air contained; (iii) the webs are adiabatic surfaces; and (iv) the upper part transfers the heat to the external atmosphere through convection ($h = 10$ W/m^2) and radiation ($\varepsilon = 0.75$).

For the net used discretize the 100×100×8 mm cross-section, quadrangular elements (*Quad_4*) with a side of 1 mm (for the solid material and the air flow) were used, as illustrated in Figure 8b, which resulted in a net with 10 000 elements and 10 201. For the thermal properties (Table 2), the following hypotheses were considered: (i) for air, it was considered that the density, specific heat, thermal conductivity, and cinematic viscosity vary with temperature (Engineering Toolbox, 2015); (ii) for the GFRP material, it was assumed that the density, specific heat, and thermal conductivity vary with temperature, according to Bai *et al.* (2007). An analysis with a total duration of 3600 s was carried out with a time step of 1 s.

In addition to the abovementioned simulation of the evolution of the temperatures for a non-protected beam and exposed to fire on one face (E1F), the thermal response was also estimated for a beam protected with calcium silicate (CS) for E1F. For this, it was barely necessary to alter the geometry of the model

and add a new material, as the exchanges of heat between the protection with CS and the GFRP profile happen through conduction. According to the information obtained through the facilitator of the material, the thermal properties of the CS (density, specific heat, and conductivity) were considered as variable with the temperature.

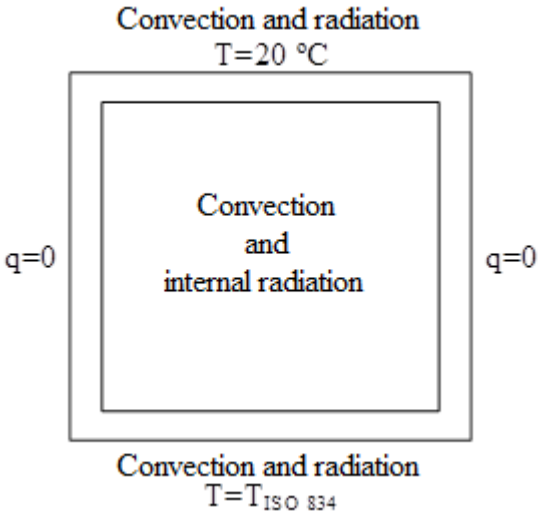

Figure 8. Boundary conditions in the numeric model.

Table 2. Thermal properties considered.

Properties	GFRP[4] (20-1000 ºC)	Ar[5] (20-1000 ºC)
Density [kg/m^3]	1890-1351	1.21-0.28
Specific heat [J/kg.ºC]	1053-877	1005-1185
Conductivity [W/m.ºC]	0.35-0.10	0.03-0.08
Viscosity [kg/m.s]	-	1.85-4.79 (×10^{-5})

4 (Engineering Toolbox, 2015), [5] (Morgado *et al.*, 2013)

3.2 Numeric *vs.* Experimental results

Figure 9 presents, in an illustrative manner, the numeric distribution of temperatures in the cross-section of the NP-S1 beam after and during 30 minutes of exposure to fire. Figure 10 shows the comparison of the experimental temperatures measured in the NP-S1 beam with the corresponding values obtained through the numeric model. It is confirmed that, globally, the numeric curves are consistent with the ones obtained experimentally, particularly on the upper (T2) and lower (T9) parts. The considerably higher values of experimental temperatures measured in the web (T4, T5, and T6), especially in their lower zone (T5 and T6), could be associated to an eventual isolation lateral deficit of the lower part of the webs, which may not have been completely efficient.

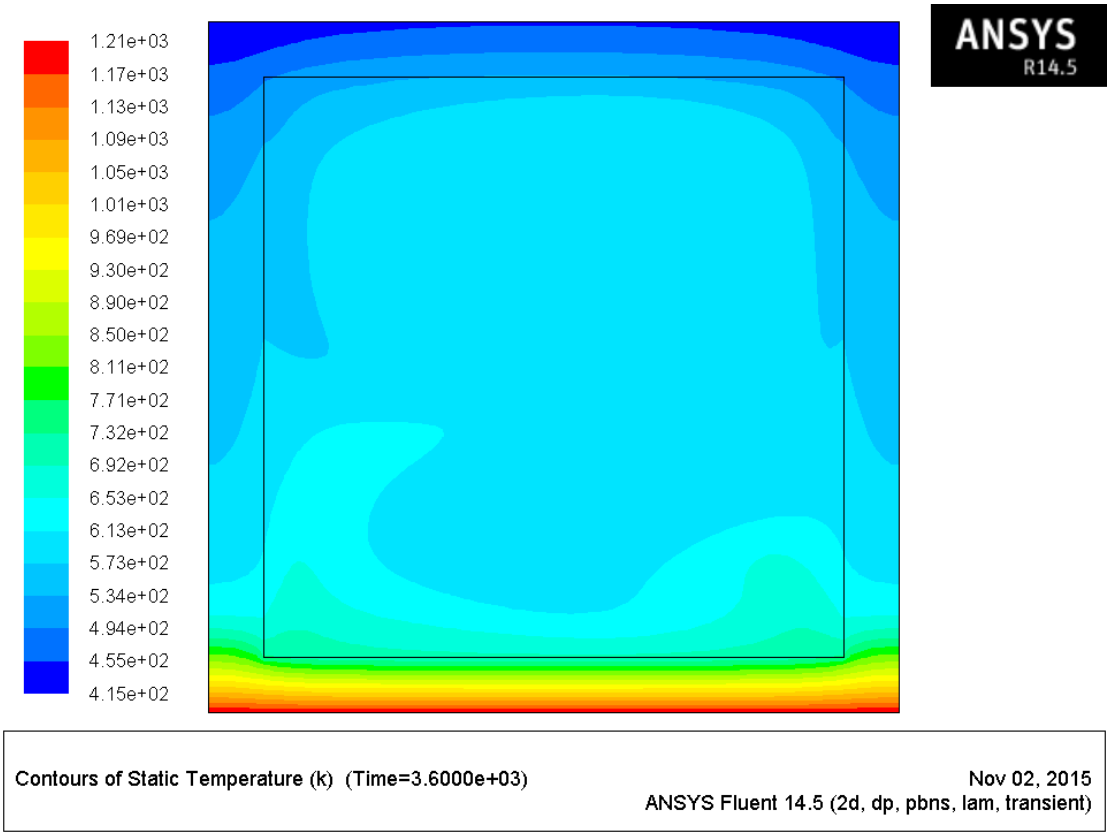

Figure 9. Numeric distribution of the temperatures of the NP-S1 beam (t=60 minutes).

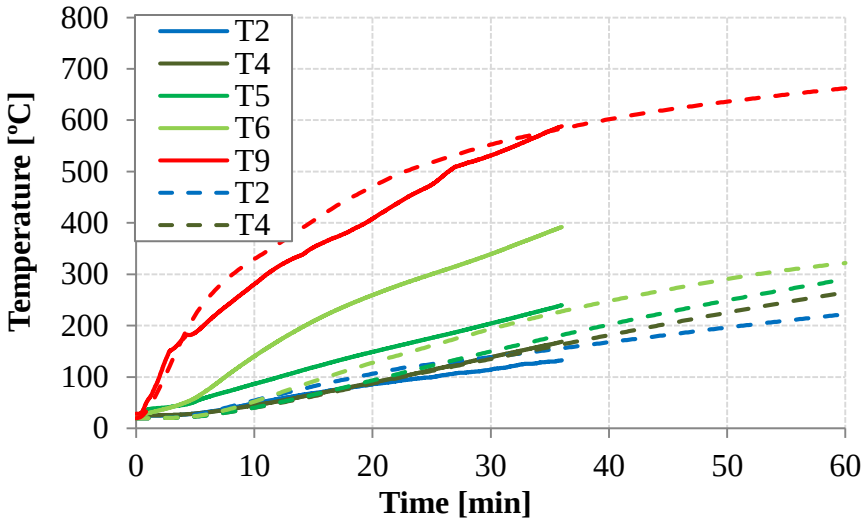

Figure 10. Thermal response of the NP-S1 beam: experimental (solid) and numeric (dotted).

For the beam protected with SC, the temperature distribution in the section is presented in Figure 11. Comparing the temperatures experimentally obtained with the ones numerically obtained, it was observed that the numeric temperatures in the web (T4-T6) were, once more, inferior to the experimental ones, as illustrated in Figure 12; this could be related to an eventual deficient lateral isolation of the profile. The evolution of the numeric temperatures in the upper frame face (T2) was comparable to the experimental ones. However, in the lower face (T9), despite the numeric and experimental temperatures presenting a similar magnitude, it is possible to observe some differences regarding the increase

tendencies of the temperature (increase rate throughout the test). This seems to be related to the thermal properties considered for the CS (provided by the manufacturer), which may not reproduce the real behavior of the material with enough precision.

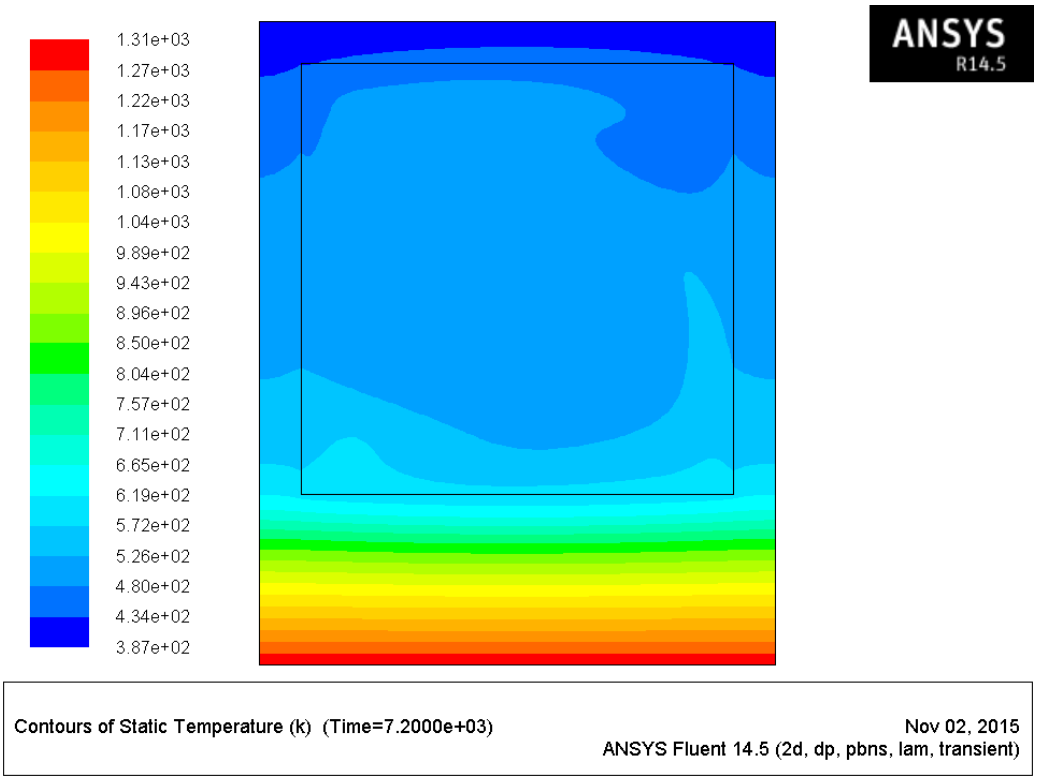

Figure 11. Numeric distribution of the temperatures of the SC-S1 beam (t=60 minutes).

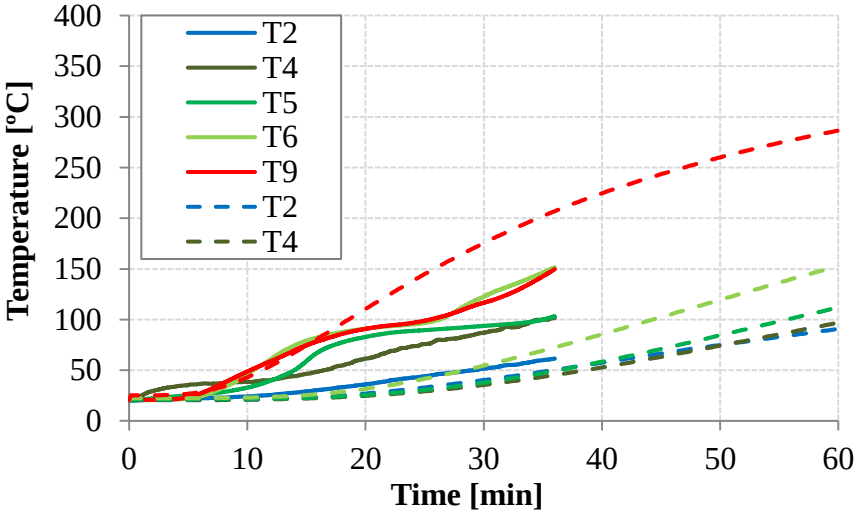

Figure 12. Thermal response of the SC-S1 beam: experimental (solid) and numeric (dotted).

4. ANALYTICAL STUDY

4.1 Analytical model

In the analytical study, a model was developed to simulate the mechanical response registered in the fire resistance tests, particularly to determine the evolution of the displacements in the middle of the span of the beams in relation to the time of exposure to fire. The analytical model developed is based (i) on an analysis of the section through the slice method, which, for each instant of time, is considered the variation of the mechanical properties of the GFRP material with the temperature, and (ii) at the beginning of the virtual works, applying the Timoshenko beam theory (Bank, 2006), that is, taking into consideration the deformability through flexion and the deformability through cutting.

As with the Mouritz study (2003), the cross-section of the GFRP beam was divided into several layers as illustrated in Figure 13. Subsequently, a temperature was attributed to each one of the layers for each instant of time, this attribution can be done through the experimental tests or through the thermal numeric model described in the previous section. Based on the temperature of each layer, the corresponding modules of elasticity and compression (E_C), the traction (E_T), and the distortion module (G) were determined. The variation of these mechanical properties in relation to the temperature was estimated based on the tests carried out at the *Instituto Superior Técnico* (Correia et al., 2013). It is important to note that the position of the neutral axis (x_{LN}) was calculated for each instant of time, through which the flexural rigidity of equivalent flexion (EI_{eq}) of the section was calculated. To determine the rigidity of the cut (G_mA_v), a mean distortion module (G_m) was calculated for each instant of time. Otherwise, G_m was calculated through a ponderation between the distortion module on each slice and the areas of the same ($G_m=\sum G_iA_i/\sum A_i$). Regarding the cut area (A_v), it was considered that the same is constant ($A_v= k\times A$, A being the area of the section and k the cut coefficient). Once the parameters EI_{eq} and G_mA_v have been estimated, the displacement (δ) in the middle of the span of the beam is obtained through the principle of virtual works, using equation (1) which takes into consideration the parcels of deformation by flexion and deformation by cutting:

$$\delta(t) = \int \frac{M\overline{M}}{EI_{eq}(t)}dx + \int \frac{V\overline{V}}{G_mA_v(t)}dx \qquad (1)$$

4.2 Analytical *vs.* Experimental results

The aforementioned model was implemented to estimate the evolution of the displacements in the middle of the span of the NP-S1 beam, with a tubular section and exposed to fire on one face. Figure 14 shows a comparison between the variation of the displacements in the middle of the span measured in the resistance to fire tests and the corresponding values obtained through the analytical model, considering the temperatures that were experimentally measured (model 1) and the ones calculated numerically (model 2). It can be observed that, globally, the analytical model developed offered a good approximation to the experimental results, considering the temperatures measured experimentally (mod. 1 curve) and the numerically calculated temperatures (mod. 2 curve). In both cases, despite the model having offered variations of displacements that are slightly inferior to the ones experimentally measured during the initial part of the thermal exposure, the same was able to reproduce the progressive increase of the arrow in the middle of the span before the collapse and also presented relatively precise estimations (given the complexity of the phenomena that intervenes) in the experimental fire resistance (35 minutes) of the beam – 30 minutes (model 1) and 31 minutes (model 2). It is worth pointing out that the analytical curves represented in Figure 14 show a less regular development than the experimental one, especially in model 1. This is due (i) to the finite number of layers considered and, overall (ii) to the variations of the different

mechanical properties of the GFRP material with the temperature considered in the models, which represent constant values for certain intervals of temperature (Correia *et al*. 2013). In the case of model 1, it emphasizes the fact of having considered a smaller number of temperatures than in model 2.

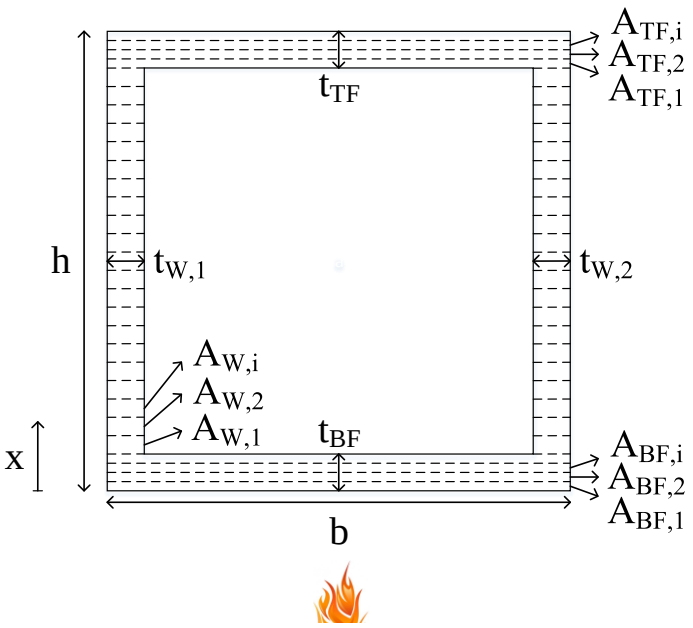

Figure 13. Analytical model: discretization of the section in layers.

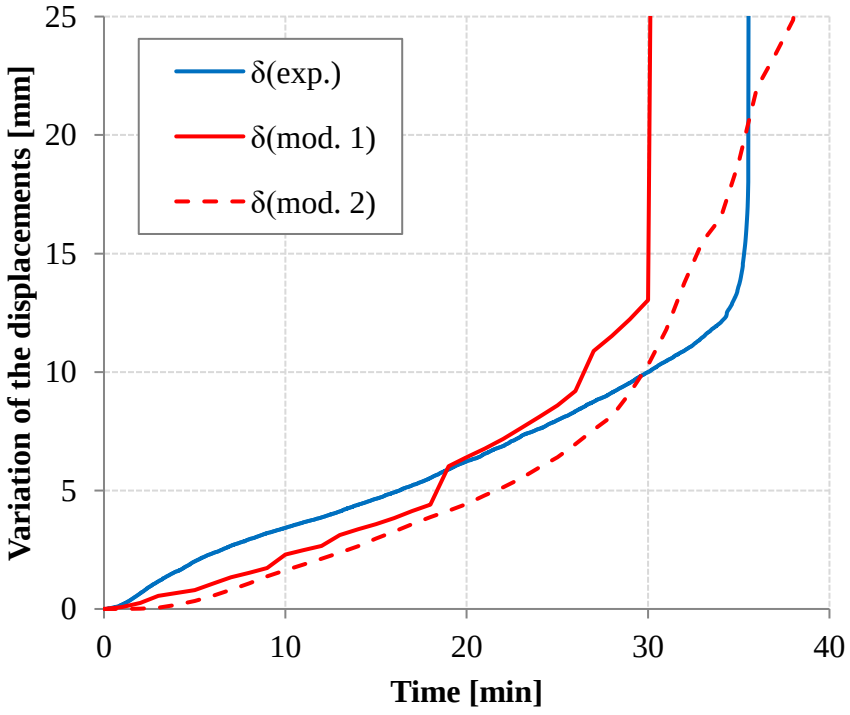

Figure 14. Mechanical response: experimental and analytical results of the NP-S1 beam.

5. CONCLUSIONS

The experimental procedure showed that the different protection systems allowed for the considerable improvement of the behavior to fire of the GFRP beams. It was observed that the most efficient protection materials were the cork agglomerate, rock wool, and calcium silicate. It is important to point out that, for the exposure on one face, the cooling solution using water was clearly the most efficient, making the fire resistance time greater than 120 minutes. It was also seen that the exposure of three faces and the increase of the service load caused significant reductions on the fire resistance time. The experimental tests carried out also helped to confirm that the pultruded profiles of GFRP, when exposed to high temperatures, are more vulnerable to compression and cutting than to traction. In fact, for most of the tests, the collapse of the beams happened due to the longitudinal compression of the upper face and/or due to the compression or cutting of the webs. The beams exposed to fire on three faces without passive protection presented a collapse mechanism by cutting with the arching of the web.

The thermal numeric model (bi-dimensional) developed using the commercial *software ANSYS FLUENT,* made it possible to evaluate the distribution of temperatures on the beams exposed to fire on one face, both non-protected and protected with CS. In this model, both the heat exchange between the solid (GFRP and CS) and the external environment (by radiation and convection) and the heat exchange between the solid and the air (fluid) in the interior of the cavity by convection, as well as by radiation between the internal walls of the section, were considered. A reasonable consistency between the experimental and the numeric curves regarding the temperature of the upper and lower faces was obtained. The webs registered relatively significant differences, which could be explained by a deficient lateral isolation between the GFRP profile and the covers of the furnace.

The analytical model developed made it possible to estimate the evolution of the displacements in the middle of the span of the non-protected beam exposed to fire on one face. In this model, the cross-section of the beam was divided into layers, which were attributed to different temperatures corresponding to the times of exposure to fire and, consequently, to different mechanical properties regarding traction, compression, and cutting. For each instance of time, the arrows in the middle of the span were calculated through the Timoshenko beam theory. A good consistency was obtained between the variation of the displacements with the time and relatively precise estimations of the fire resistance times.

6. ACKNOWLEDGEMENTS

The authors would like to thank FCT (PTDC/ECM/100779/2008 project) and the ICIST for financing the investigation. The first author is grateful to FCT for the doctorate scholarship that was granted to him SFRH/BD/94907/2013.

7. REFERENCES

Correia, J. R. (2012), "*Materiais compósitos de matriz polimérica*", em Ciência e Engenharia dos Materiais de Construção, IST Press, Lisboa.

Correia, J. R. (2004), "*Perfis pultruidos de polímero reforzado com fibras de vidrio (GFRP). Aplicação de vigas mistas GFRP betão na construção*", Dissertação de Mestrado em Construção, Instituto Superior Técnico, Universidade Técnica de Lisboa.

Samanta, A. *et al.* (2004), "*Thermo mechanical assessment of polymer composites subjected to fire*", The Robert Gordon University, Aberdeen.

Mouritz, A. P., Gibson, A. G. (2006), "*Fire properties of polymer composite materials*", Springer, Dordrecht.

Correia, J. R. *et al.* (2013), "*Mechanical behaviour of pultruded glass fibre reinforced polymer composites at elevated temperature: Experiments and model assessment*", Composites Structures, V. 98, pp. 303-313.
Ludwig, C. *et al*. (2008), "*Thermal and Thermo mechanical Investigation of Polyester based Composite Beams*", Fouth International Conference on FRP Composites in Civil Engineering, Zurich.
Correia, J. R. *et al.* (2010), "*Fire protection system for building floors made of pultruded GFRP profiles. Part 1: Experimental investigations*", Composites: Part B, V. 41, pp. 617-629.
ISO 834-1 (1999), "*Fire resistance tests. Elements of building construction - Part 1: General requirements*", International Standards Organization, Genève.
Software comercial *ANSYS FLUENT*, ANSYS, inc, versão 14.2, (2012).
Morgado, T. *et al.* (2013), "*Comportamento ao fogo de vigas de compósito de GFRP*", Revista Internacional Construlink, n.º 32, pp. 4-19.
Website, http://www.engineeringtoolbox.com/dry-air-properties-d_973.html, (2015).
Bai, Y., Vallé, T., Keller, T. (2007), "*Modeling of thermos physical properties for FRP composites under elevated and high temperature*", Composites Science and Technology, V. 67, pp. 3098-3109.
Bank, L. C. (2006), "*Composites for construction: Structural design with FRP materials*", Wiley, Hoboken.
Mouritz, A. (2003), "*Simple models for determining the mechanical properties of burnt FRP composites*", Materials and Engineering, V. 359, pp. 237-246.

ALCONPAT Journal, Volume 6, Issue 2, may – august 2016, Pages 173 – 189

ALCONPAT Journal

www.revistaalconpat.org

eISSN 2007-6835

Journal of the Latin-American Association of Quality Control, Pathology and Recovery of Construction

A new model for the design of rectangular combined boundary footings with two restricted opposite sides

A. Luévanos Rojas1

[1]Engineering Department, Science and Architecture. Universidad Juárez del Estado de Durango, Gómez Palacio, Durango, México.

Article information
DOI:
http://dx.doi.org/10.21041/ra.v6i2.137
Article received on November 28th 2015, reviewed under publishing policies of ALCONPAT journal and accepted on March 13th 2016. Any discussion, including the replica of the authors, shall be published in the first number of the year 2017 as long as the information is received prior to the closing of the third number of the year 2016.

Legal Information

ALCONPAT Journal, Year 6, No. 2, May – August 2016, is a quarterly publication of the Latin American Association of Quality Control, Pathology and Construction Recovery, International, A.C., Km. 6, Old Highway to Progreso, Mérida, Yucatán, Zip Code 97310, Tel. +52 1 (999) 738-5893, alconpat.int@gmail.com, Website: www.alconpat.org
Responsible Editor: Dr. Pedro Castro Borges. All rights reserved for exclusive use, No. 04-2013-011717330300-203, eISSN 2007-6835, both granted by the National Institute of Copyright. Responsible for the last update of this number, Informatics Unit ALCONPAT, Elizabeth Sabido Maldonado, Km. 6, Old Highway to Progreso, Mérida, Yucatán, Zip Code 97310, publication date: May 30, 2016.

ABSTRACT

This document presents a new model for the design of rectangular combined boundary footings with two restricted opposite sides, taking into consideration the real pressure of the ground on the contact surface of the footing in order to obtain: the moments around the longitudinal axes parallel to axis "Y-Y"; the moments around the transversal axes parallel to the "X-X" axis; the unidirectional shear force (Flexural shearing); and the bi-directional shear force (penetration shearing) for the two columns. The real pressure of the ground is presented in terms of the mechanical elements that act on each column (P, M_x, and M_y). The mathematical approach suggested in this work gives results with a tangible preciseness in order to find the most economical solution.

Keywords: footing design; rectangular combined boundary footings; moments; unidirectional shearing force (flexural shearing); bi-directional shearing force (penetration shearing).

RESUMEN

Este documento presenta un nuevo modelo para diseño de zapatas combinadas rectangulares de lindero con dos lados opuestos restringidos tomando en cuenta la presión real del suelo sobre la superficie de contacto de la zapata para obtener: Los momentos alrededor de ejes longitudinales paralelos al eje "Y-Y"; Los momentos alrededor de ejes transversales paralelos al eje "X-X"; La fuerza cortante unidireccional (Cortante por flexión); La fuerza cortante bidireccional (cortante por penetración) para las dos columnas. La presión real del suelo se presenta en función de los elementos mecánicos que actúan en cada columna (P, M_x, y M_y). El enfoque matemático sugerido en este trabajo produce resultados que tienen una exactitud tangible para encontrar la solución más económica.

Palabras clave: diseño de zapatas; zapatas combinadas rectangulares de lindero; momentos; fuerza cortante unidireccional (cortante por flexión); fuerza cortante bidireccional (cortante por penetración).

RESUMO

Este trabalho apresenta um novo modelo a design de footings combinadas retangulares de fronteira com dois lados opostos restringidas, tendo em conta a pressão real do solo na superfície de contato do o footing para obter: Os momentos em torno eixos longitudinais paralelos ao eixo "Y-Y"; Os momentos em torno eixos transversais paralelos ao eixo "X-X"; A força ao cisalhante em um endereço (corte em flexão); A força ao cisalhante em dois endereços (punçoamento) para as duas colunas. A pressão real do solo é apresentada em termos de elementos mecânicos que actuam em cada coluna (P, M_x, e M_y). A abordagem matemática sugerido neste trabalho produz resultados que têm uma precisão tangível para encontrar a solução mais econômica.

Palavras-chave: design de footings; footings combinadas retangulares de fronteira; momentos; força ao cisalhante em um endereço (corte em flexão); força ao cisalhante em dois endereços (punçoamento).

Corresponding author: Arnulfo Luévanos Rojas (arnulfol_2007@hotmail.com)

1. INTRODUCTION

The substructure or foundation is the part of the structure that is generally placed underneath the surface of the plot of land and which transfers the loads to the ground or to the subjacent rock. Each construction requires solving a foundation problem. Foundations are classified as shallow or deep, which represent the important differences in accordance with their geometry, in terms of the behavior of the ground, their structural use, and their constructive systems (Bowles, 1996; Nilson, 1999; Das et al., 2006).
Shallow foundations, whose constructive systems generally do not present major difficulties, can be of different types depending on their use: isolated footing, combined footing, strip footing, or foundation slab (Bowles, 1996; Das et al., 2006).
The normal work of the structural analysis is normally done with the hypothesis that the structure of the buildings is embedded on the floor, i.e., it is supported by an un-deformable material (Calavera-Ruiz, 2000; Tomlinson, 2008).
The distribution of the pressure of the ground under a footing is a function of the type of soil, the relative rigidity of the soil and the foundation, and the depth of the foundation at the contact level between the footing and the ground. One concrete footing resting on thick granular soils (sandy soils) will have a similar pressure distribution as the one shown in Figure 1(a). When a rigid footing is resting on sandy soil, the sand near the borders of the footing tends to move laterally when the footing is loaded, this tends to decrease the pressure of the soil near the borders while the soil far from the borders of the footing is relatively confined. In contrast, the distribution of pressure under one footing that lies on fine-grained soils (clay soil) is similar to Figure 1(b); when the footing is loaded, the soil under the footing is deviated in a bowl-shaped depression, relieving the pressure under the center of the footing. For design purposes, it is common to assume that the pressure of the soil is lineally distributed. The distribution of the pressure will be uniform if the center of the footing coincides with that resulting from the applied loads, as shown in Figure 1(c) (Bowles, 1996; Nilson, 1999).

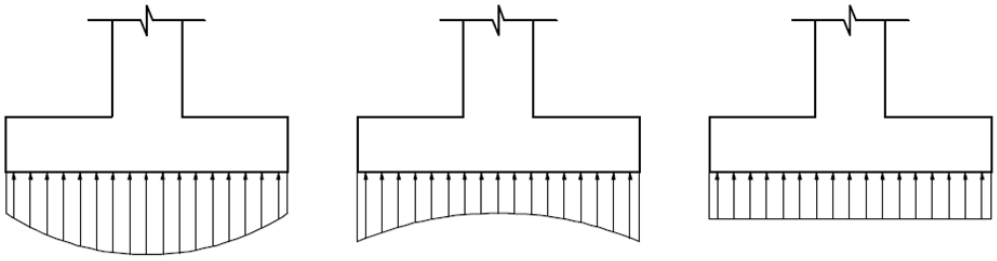

Figure 1. Distribution of the pressure under the footing: (a) Footing on thick granular soils; (b) Footing on fine soils; (c) Uniform equivalent distribution.

A combined footing is a large footing that supports two or more columns in (typically two) one row (Kurian, 2005; Punmia et al., 2007; Varghese, 2009).
Combined footings are used when: 1) The existing relation between loads, permissible capacity of the soil in the foundation, and the distance between adjacent columns make the construction of isolated footings impossible. 2) An external column is so close to the boundary of the property that it is not possible to center an isolated footing underneath it (Nilson, 1999; Kurian, 2005; Punmia et al., 2007; Varghese, 2009).
Combined footings are designed so that the centroid of the area of the footing coincides with that resulting from the loads of the two columns. This produces a uniform contact pressure on the entirety of the area and prevents the tilting tendency of the footing. On a plan view, these footings are rectangular,

trapezoidal or in T-shape, and the details of their shape accommodate themselves so that they coincide with their centroid and that of the resultant (Nilson, 1999; Kurian, 2005; Punmia et al., 2007; Varghese, 2009).

Another resource used when it is not possible to center a simple footing under an external column, consists on placing the footing for the external column in an eccentric manner and connect it to the footing of the closest internal column through a beam or a supporting band. This support beam, when balanced by the load of the internal column, can resist the tilting tendency of the eccentric external footing and matches all the pressures under it. This type of foundations is known as footing with support beams, projected or connected (Nilson, 1999; Kurian, 2005; Punmia et al., 2007; Varghese, 2009).

Another solution for the design of the combined footings under columns subjected to biaxial-flexure is to consider the maximum pressure of the ground, which is considered uniform at all points of contact (Calavera-Ruiz, 2000; Tomlinson, 2008).

Some recently published documents that consider the real pressure of the ground are: Design of rectangular-shaped isolated footings using a new model (Luévanos-Rojas et al, 2013); Design of circular-shaped isolated footings using a new model (Luévanos-Rojas, 2014a); Design of rectangular-shaped combined boundary footings using a new model (Luévanos-Rojas, 2014b), this footing considers only one restricted side.

This document presents a new model for the design of rectangular combined boundary footings with two restricted opposite sides to obtain: 1) The moments around a longitudinal axis (one *a-a* axis with a "b_1" width and a *b-b* axis with a "b_2" width, which are parallel to the "Y-Y" axis; 2) The moments around a transversal axis (one *c-c* axis, one *d-d* axis, and one *e-e* axis that are parallel to the "X-X" axis); 3) The unidirectional shear force (Flexural shearing) on the *f-f*, *g-g*, *h-h*, and *i-i* axes; 4) The bidirectional shear force (Shearing by penetration) on a rectangular section formed by points 5, 6, 7, and 8 for column 1 (left boundary) and the rectangular section formed by points 9, 10, 11, and 12 for column 2 (right boundary). The real pressure of the ground that acts on the contact surface of the footing is different on the four corners, this pressure is presented in terms of the mechanical elements that act on each column (axial load, moment around the "X" axis, and moment around the "Y" axis). The mathematical approach suggested in this work produces results that have a tangible precision for all the problems, which is an essential part of this investigation to find the most economical solution.

2. PROPOSED MODEL

2.1 General considerations

According to the requirements of the Construction Code for Structural Concrete and Comments, the critical sections are: 1) the maximum moment is found on the face of the column, pedestal, or wall for footings that support a concrete column, pedestal, or wall; 2) the flexural shear force is presented at a "*d*" distance (distance from the extreme compressed fiber to the center of the longitudinal reinforcement steel) and will be measured from the face of the column, pedestal, or wall for footings that support a column, pedestal, or on the wall; and 3) the shear force by penetration is located so that the "b_o" perimeter is a minimum, but should not come closed to less than "*d/2*" to: (a) the borders or corners of the columns, the concentrated loads, or reaction zones; and (b) the changes in the thickness of the slab, such as the borders of the capitals, abacus, or cutting cover (ACI, 2013; McCormac y Brown, 2013).

The general equation for any type of footings subject to bidirectional flexion is (González-Cuevas y Robles-Fernández-Villegas, 2005; Punmia et al., 2007; Gere and Goodo, 2009):

$$\sigma = \frac{P}{A} \pm \frac{M_x y}{I_x} \pm \frac{M_y x}{I_y} \quad (1)$$

where:
σ: pressure exercised by the ground on the footing (pressure of the plot of land),
A: contact area of the footing,
P: e axial load applied on the center of gravity of the footing,
M_x: moment around the "X" axis,
M_y: moment around the "Y" axis,
x: distance in the "X" direction measured from the "Y" axis to the fiber in the study,
y: distance in the "Y" direction measured from the "X" axis to the fiber being studied,
I_y: moment of inertia around the "Y" axis,
I_x: moment of inertia around the "X" axis.

2.2. Model for the dimensioning of the footings

Figure 2 shows a rectangular combined boundary footing with two restricted opposite sides supporting two rectangular columns of different dimensions, each column subject to an axial load and moment in two directions (bidirectional flexure).

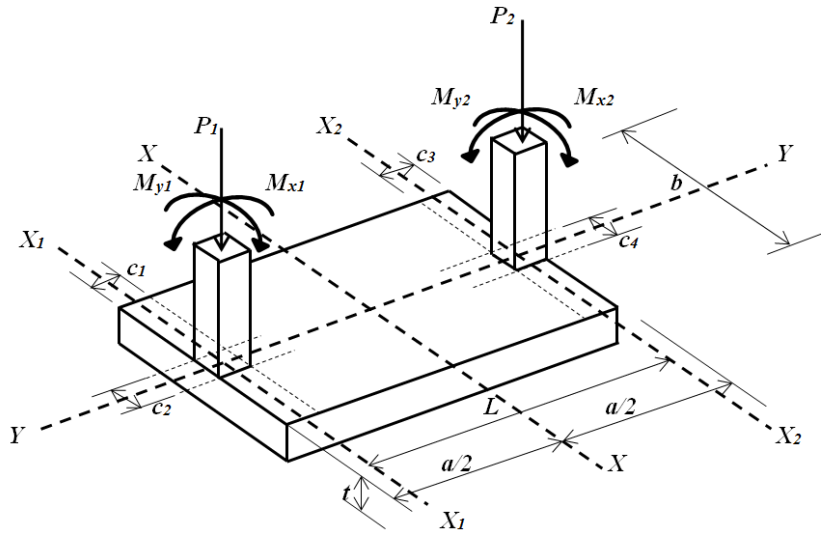

Figure 2. Rectangular combined footing with two opposite restricted sides

The value of "a" is fixed and can be expressed in terms of "L" as follows:

$$a = L + \frac{c_1}{2} + \frac{c_3}{2} \quad (2)$$

where: a is the dimension of the footing parallel to the "Y" axis.
Replacing $A = ab$, $I_x = ba^3/12$, $I_y = ab^3/12$, $y = a/2$, $x = b/2$ in the equation (1) we obtain:

$$\sigma = \frac{R}{ab} \pm \frac{6M_{xT}}{ba^2} \pm \frac{6M_{yT}}{ab^2} \quad (3)$$

where:
b: dimension of the footing parallel to the "X" axis,
$R = P_1+P_2$, $M_{yT} = M_{y1}+M_{y2}$: total moment around the "Y" axis,
$M_{xT} = M_{x1}+M_{x2}+ P_1(a/2–c_1/2)–P_2(a/2–c_3/2)$: total moment around the "X" axis.
Considering that the pressure of the plot of land should be zero, as the soil is not capable of resisting traction, the value of "*b*" is:

$$b = \frac{6M_{yT}a}{Ra - 6M_{xT}} \tag{4}$$

Considering that the pressure of the plot of land should be the permissible load capacity available of the ground "σ_{adm}", the value of "*b*" is:

$$b = \frac{Ra + 6M_{xT} + \sqrt{(Ra + 6M_{xT})^2 + 24\sigma_{adm}M_{yT}a^3}}{2\sigma_{adm}a^2} \tag{5}$$

The permissible load capacity of the ground is obtained in the following manner:

$$\sigma_{adm} = q_a - \gamma_{ppz} - \gamma_{pps} \tag{6}$$

where: q_a is the permissible load of the ground, γ_{ppz} is the weight of the footing, γ_{pps} is the weight of the filling of the ground.

2.3. New model for the design of footings
Figure 3 shows the pressure diagram for rectangular combined boundary footings with two restricted opposite sides subject to an axial load and the moment in two directions (bidirectional flexure) in each column, wherein the pressure is presented differently in the four corners and lineally varying throughout the length of the contact surface.

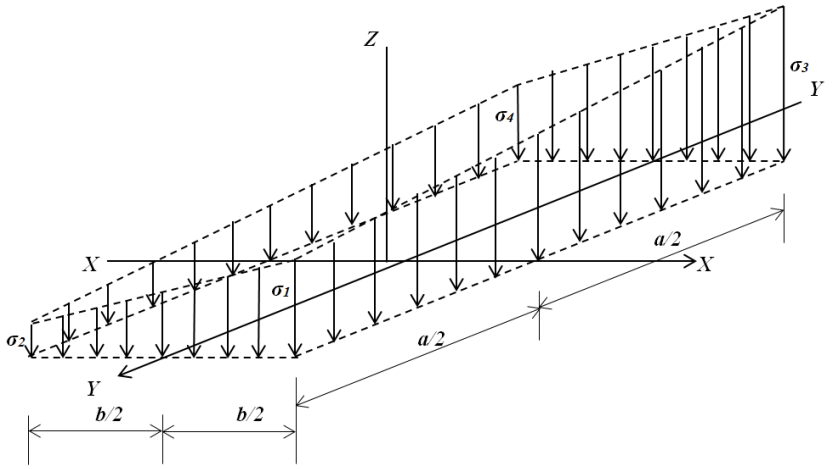

Figure 3. Pressure diagram for the rectangular combined boundary footing with two restricted opposite sides.

Figure 4 shows a couple of rectangular combined boundary footings with two restricted opposite sides to obtain the pressure at any place of the contact surface of the structural member due to the pressure exerted by the ground.

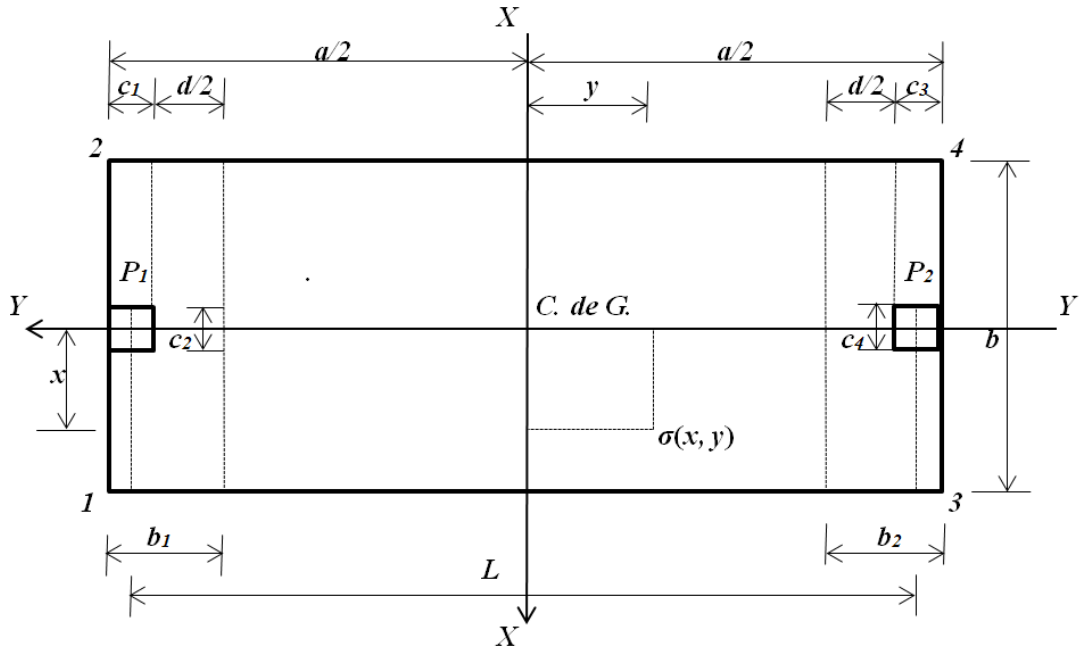

Figure 4. Rectangular combined boundary footing with two restricted opposite sides

The pressure of the plot of land in the transversal direction is:
For column 1 it is:

$$\sigma_{P_1}(x,y) = \frac{P_1}{b_1 b} + \frac{12M_{y1}x}{b_1 b^3} + \frac{12\left[M_{x1} + P_1\left(\frac{b_1}{2} - \frac{c_1}{2}\right)\right]y}{b{b_1}^3} \quad (7)$$

For column 2 it is:

$$\sigma_{P_2}(x,y) = \frac{P_2}{b_2 b} + \frac{12M_{y2}x}{b_2 b^3} + \frac{12\left[M_{x2} + P_2\left(\frac{b_2}{2} - \frac{c_3}{2}\right)\right]y}{b{b_2}^3} \quad (8)$$

The pressure of the plot of land in the longitudinal direction is:

$$\sigma(x,y) = \frac{R}{ab} + \frac{12M_{yT}x}{ab^3} + \frac{12M_{xT}y}{ba^3} \quad (9)$$

where: $b_1 = c_1 + d/2$ is the width of the fault surface under column 1, while $b_2 = c_3 + d/2$ is the width of the fault surface under column 2.

2.3.1. Moments

The critical sections for the moments are shown in Figure 5. These are present in sections *a-a*, *b-b*, *c-c*, *d-d*, and *e-e*.

2.3.1.1. Moments around the "a-a" axis

The resulting force of "F_{Ra}" can be found through the pressure volume of the zone formed by the *a-a* axis with a width of $b_1 = c_1 + d/2$ and the free end of the rectangular footing, where most of the pressure is:

Now the center of gravity "x_{ca}" is obtained:

$$F_{Ra} = \int_{-\frac{b_1}{2}}^{\frac{b_1}{2}} \int_{\frac{c_2}{2}}^{\frac{b}{2}} \sigma_{P_1}(x,y)dxdy = \frac{\left[P_1 b^2 + 3M_{y1}(b + c_2)\right](b - c_2)}{2b^3} \qquad (10)$$

The moment around the "*a-a*" axis can be found through the following equation:

$$x_{ca} = \frac{\int_{-\frac{b_1}{2}}^{\frac{b_1}{2}} \int_{\frac{c_2}{2}}^{\frac{b}{2}} x\sigma_{P_1}(x,y)dxdy}{\int_{-\frac{b_1}{2}}^{\frac{b_1}{2}} \int_{\frac{c_2}{2}}^{\frac{b}{2}} \sigma_{P_1}(x,y)dxdy} = \frac{P_1 b^2(b + c_2) + 4M_{y1}(b^2 + bc_2 + {c_2}^2)}{4\left[P_1 b^2 + 3M_{y1}(b + c_2)\right]} \qquad (11)$$

Replacing equations (10) and (11) in equation (12), we obtain the following:

$$M_{a-a} = F_{Ra}\left(x_{ca} - \frac{c_2}{2}\right) \qquad (12)$$

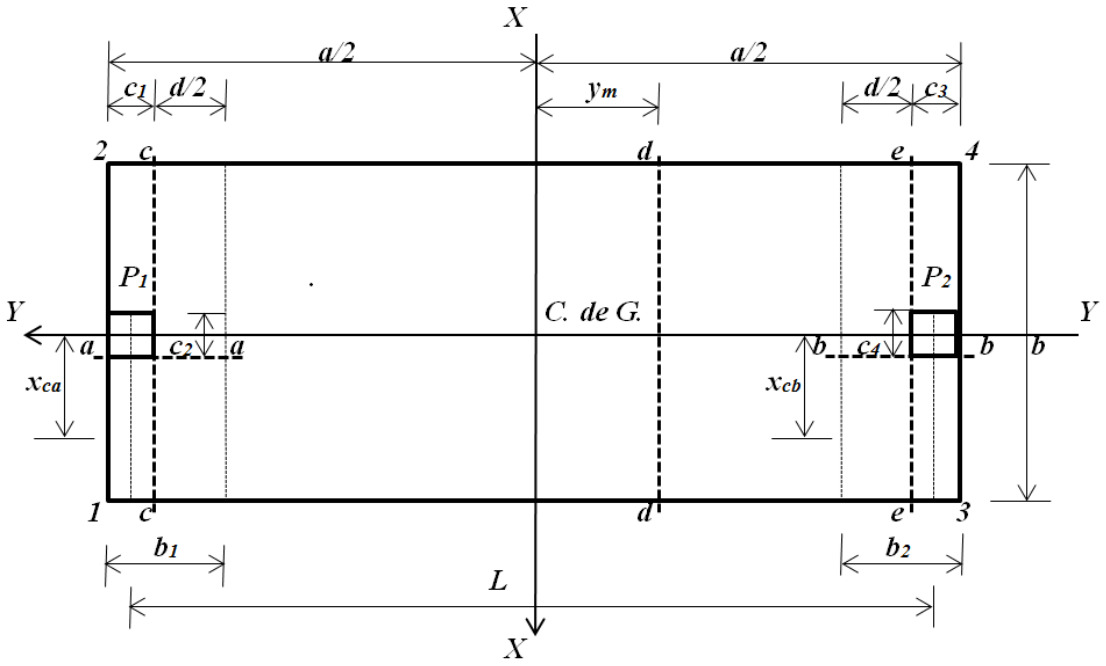

Figure 5. Critical sections for the moments

2.3.1.2. Moments around the "b-b" axis

The resulting "F_{Rb}" force can be found through the volume of pressure of the zone formed by the *b-b* axis with a width of $b_2 = c_3 + d/2$ and the free end of the rectangular footing, where the most pressure is:

$$F_{Rb} = \int_{-\frac{b_2}{2}}^{\frac{b_2}{2}} \int_{\frac{c_4}{2}}^{\frac{b}{2}} \sigma_{P_2}(x,y)dxdy = \frac{\left[P_2 b^2 + 3M_{y2}(b + c_4)\right](b - c_4)}{2b^3} \qquad (14)$$

Now, the gravity center "x_{cb}" is obtained:

$$x_{cb} = \frac{\int_{-b_2/2}^{b_2/2} \int_{c_4/2}^{b/2} x\sigma_{P_2}(x,y)dxdy}{\int_{-b_2/2}^{b_2/2} \int_{c_4/2}^{b/2} \sigma_{P_2}(x,y)dxdy} = \frac{P_2 b^2(b + c_4) + 4M_{y2}(b^2 + bc_4 + {c_4}^2)}{4\left[P_2 b^2 + 3M_{y2}(b + c_4)\right]} \qquad (15)$$

The moment around the "*b-b*" axis can be found through the following equation:

$$M_{b-b} = F_{Rb}\left(x_{cb} - \frac{c_4}{2}\right) \qquad (16)$$

Replacing equations (14) and (15) in equation (16), we obtain the following:

$$M_{b-b} = \frac{\left[P_2 b^2 + 2M_{y2}(2b + c_4)\right](b - c_4)^2}{8b^3} \qquad (17)$$

2.3.1.3. Moments around the "c-c" axis

The resulting "F_{Rc}" is the pressure volume of the area formed by the *c-c* axis and corners 1 and 2, this is presented as follows:

$$F_{Rc} = \int_{\frac{a}{2}-c_1}^{\frac{a}{2}} \int_{-\frac{b}{2}}^{\frac{b}{2}} \sigma(x,y)dxdy = \frac{[Ra^2 + 6M_{xT}(a-c_1)]c_1}{a^3} \quad (18)$$

The center of gravity "y_{cc}" of the pressure volume of the area formed by the *c-c* axis and corners 1 and 2 is obtained as follows:

$$F_{Rc} = \int_{\frac{a}{2}-c_1}^{\frac{a}{2}} \int_{-\frac{b}{2}}^{\frac{b}{2}} \sigma(x,y)dxdy = \frac{[Ra^2 + 6M_{xT}(a-c_1)]c_1}{a^3} \quad (18)$$

The moment around the "*c-c*" axis is found through the following equation:

$$M_{c-c} = F_{Rc}\left[y_{cc} - \left(\frac{a}{2} - c_1\right)\right] - P_1\left(\frac{c_1}{2} + \frac{M_{x1}}{P_1}\right) \quad (20)$$

Replacing equations (18) and (19) in equation (20), we obtain the following:

$$M_{c-c} = -\frac{(P_1c_1 + 2M_{x1})a^3 - [Ra^2 + 2M_{xT}(3a - 2c_1)]{c_1}^2}{2a^3} \quad (21)$$

2.3.1.4. Moments around the "d-d" axis

First of all, the position of the *d-d* axis needs to be located, as it is here where we find the maximum moment. When the shearing force has a value of zero, the moment is at a maximum, thus the shearing force "$V_y = F_{Rd} - P_1$" at a "y_m" distance is shown in the following manner:

$$V_y = \int_{y_m}^{\frac{a}{2}} \int_{-\frac{b}{2}}^{\frac{b}{2}} \sigma(x,y)dxdy - P_1 = \frac{(R-2P_1)a^3 + 3M_{xT}a^2 - 2Ra^2y_m - 12M_{xT}{y_m}^2}{2a^3} \quad (22)$$

The shear force "V_y" becomes zero and the value of "y_m" is obtained:

$$y_m = \frac{a\left[\sqrt{R^2a^2 + 12M_{xT}a(R-2P_1) + 36{M_{xT}}^2} - Ra\right]}{12M_{xT}} \quad (23)$$

The center of gravity "y_{cd}" of the pressure volume of the area formed by the *d-d* axis and corners 1 and 2 is obtained as follows:

$$y_{cd} = \frac{\int_{y_m}^{\frac{a}{2}} \int_{-\frac{b}{2}}^{\frac{b}{2}} y\sigma(x,y)dxdy}{\int_{y_m}^{\frac{a}{2}} \int_{-\frac{b}{2}}^{\frac{b}{2}} \sigma(x,y)dxdy} = \frac{(Ra + 4M_{xT})a^3 - 4(Ra^2 + 8M_{xT}y_m){y_m}^2}{4(Ra + 3M_{xT})a^2 - 8(Ra^2 + 6M_{xT}y_m)y_m} \quad (24)$$

The moment around the "*d-d*" axis can be found through the following equation:

$$M_{d-d} = F_{Rd}(y_{cd} - y_m) - P_1\left(\frac{a}{2} - \frac{c_1}{2} + \frac{M_{x1}}{P_1} - y_m\right) \quad (25)$$

Replacing equations (22) and (24) in equation (25), we obtain the following:

$$M_{d-d} = -\frac{4[P_1(a - c_1 - 2y_m) + 2M_{x1}]a^3 - [Ra^2 + 4M_{xT}(a + y_m)](a - 2y_m)^2}{8a^3} \quad (26)$$

2.3.1.5. Moments around the "e-e" axis

The resulting force "F_{Re}" is the pressure volume of the area formed by the *d-d* axis and corners 1 and 2, this is presented as follows:

$$F_{Re} = \int_{-a/2+c_3}^{a/2} \int_{-b/2}^{b/2} \sigma(x,y)dxdy = \frac{[Ra^2 + 6M_{xT}c_3](a - c_3)}{a^3} \quad (27)$$

The center of gravity "y_{ce}" of the pressure volume of the area formed by the *e-e* axis and corners 1 and 2 is obtained as follows:

$$y_{ce} = \frac{\int_{-\frac{a}{2}+c_3}^{\frac{a}{2}} \int_{-\frac{b}{2}}^{\frac{b}{2}} y\sigma(x,y)dxdy}{\int_{-\frac{a}{2}+c_3}^{\frac{a}{2}} \int_{-\frac{b}{2}}^{\frac{b}{2}} \sigma(x,y)dxdy} = \frac{Ra^2c_3 + 2M_{xT}(a^2 - 2ac_3 + 4{c_3}^2)}{2Ra^2 + 12M_{xT}c_3} \quad (28)$$

The moment around the "*e-e*" axis can be found with the following equation:

$$M_{e-e} = F_{Re}\left[\left(\frac{a}{2} - c_3\right) + y_{ce}\right] - P_1\left(a - \frac{c_1}{2} - c_3 + \frac{M_{x1}}{P_1}\right) \quad (29)$$

Replacing equations (27) and (28) in equation (29), we obtain the following:

$$M_{e-e} = -\frac{[P_1(2a - c_1 - 2c_3) + 2M_{x1}]a^3 - [Ra^2 + 2M_{xT}(a + 2c_3)](a - c_3)^2}{2a^3} \qquad (30)$$

2.3.1.6. Equation of moments between the two columns

To obtain the equation of moments between the two columns, it is known that the derivative of the moment is the shear force and thus it is presented as follows:

$$V_y = \frac{dM_y}{dy} \qquad (31)$$

where: M_y is the moment at a "y" distance, and V_y is the shear force at a "y" distance.
The equation of the shear force is:

$$V_y = \frac{6M_{xT}y^2}{a^3} + \frac{Ry}{a} + \frac{(2P_1 - R)a - 3M_{xT}}{2a} \qquad (32)$$

Replacing equation (32) in equation (31) and developing the integral, we obtain the following:

$$M_y = \frac{2M_{xT}y^3}{a^3} + \frac{Ry^2}{2a} + \frac{[(2P_1 - R)a - 3M_{xT}]y}{2a} + C \qquad (33)$$

To evaluate the integration constant "C", the following are replaced: $y = a/2 - c_1$ and $M_{c\text{-}c}$, which appears in equation (21). The value of the constant is shown as follows:

$$C = \frac{Ra - 4P_1(a - c_1) - 8M_{x1} + 4M_{xT}}{8} \qquad (34)$$

Replacing equation (34) in equation (33), the equation of moments is obtained as follows:

$$M_y = \frac{2M_{xT}y^3}{a^3} + \frac{Ry^2}{2a} + \frac{[(2P_1 - R)a - 3M_{xT}]y}{2a} + \frac{Ra - 4P_1(a - c_1) - 8M_{x1} + 4M_{xT}}{8} \qquad (35)$$

2.3.2. Unidirectional shear force (flexural shearing)

The critical section for the unidirectional shear force is obtained at a distance "d" from the edge of the column, as shown in Figure 6; this is shown for sections *f-f*, *g-g*, *h-h* e *i-i*.

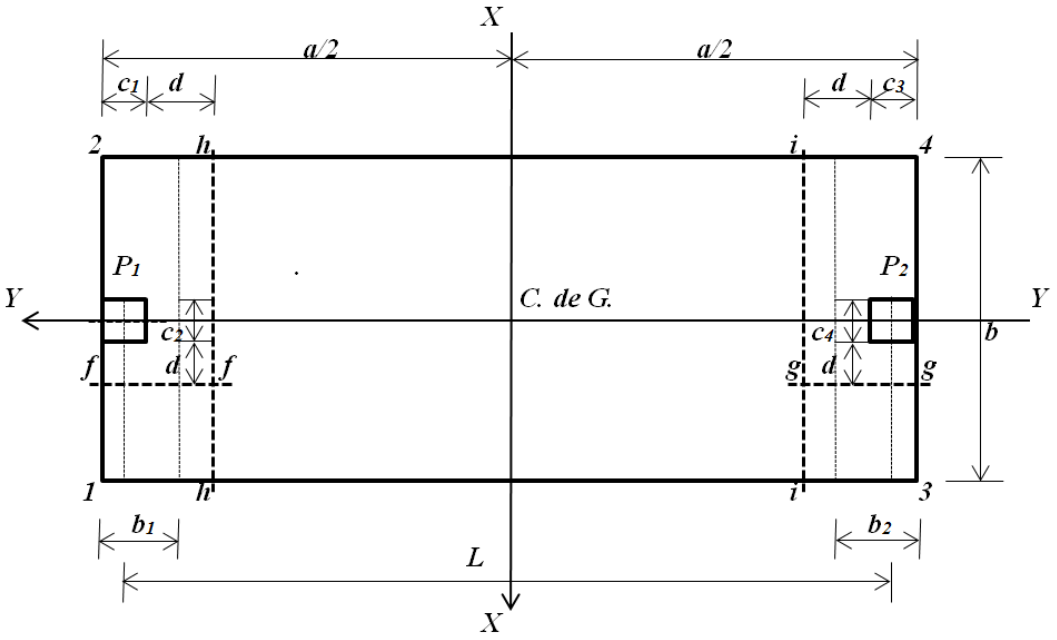

Figure 6. Critical sections for the unidirectional shear forces

2.3.2.1. Shear force on the "f-f" axis

The flexural shear force "$V_{ff\text{-}f}$" that acts on the *f-f* axis of the footing can be found through the pressure volume of the area formed by the *f-f* axis with a width of "$b_1 = c_1 + d/2$" and the free end of the rectangular footing, where most of the pressure is:

$$V_{ff-f} = \int_{-\frac{b_1}{2}}^{\frac{b_1}{2}} \int_{\frac{c_2}{2}+d}^{\frac{b}{2}} \sigma_{P_1}(x,y)dxdy = \frac{\left[P_1 b^2 + 3M_{y1}(b + c_2 + 2d)\right](b - c_2 - 2d)}{2b^3} \qquad (36)$$

2.3.2.2. Shear force on the "g-g" axis

The flexural shear force "$V_{fg\text{-}g}$" that acts on the *g-g* axis of the footing can be found through the pressure volume of the area formed by the *g-g* axis with a width of "$b_2 = c_3 + d/2$" and the free end of the rectangular footing, where most of the pressure is:

$$V_{fg-g} = \int_{-b_2/2}^{b_2/2} \int_{c_4/2+d}^{b/2} \sigma_{P_2}(x,y)dxdy = \frac{\left[P_2 b^2 + 3M_{y2}(b + c_4 + 2d)\right](b - c_4 - 2d)}{2b^3} \qquad (37)$$

2.3.2.3. Shear force on the "h-h" axis

The flexural shear force "$V_{fh\text{-}h}$" that acts on the *h-h* axis of the footing is the "P_1" force that acts on column 1 minus the pressure volume of the area formed by the *h-h* axis and corners 1 and 2 of the footing, and is shown as follows:

$$V_{fh-h} = P_1 - \int_{a/2-c_1-d}^{\frac{a}{2}} \int_{-\frac{b}{2}}^{\frac{b}{2}} \sigma(x,y)dxdy = \frac{P_1 a^3 - [Ra^2 + 6M_{xT}(a - c_1 - d)](c_1 + d)}{a^3} \qquad (38)$$

2.3.2.4. Shear force on the "i-i" axis

The flexural shear force "$V_{fi\text{-}i}$" that acts on the *i-i* axis of the footing is the "P_1" force that acts on column 1 minus the pressure volume of the area formed by the *i-i* axis and corners 1 and 2 of the footing, and it is shown as follows:

$$V_{fi-i} = P_1 - \int_{-a/2+c_3+d}^{\frac{a}{2}} \int_{-\frac{b}{2}}^{\frac{b}{2}} \sigma(x,y)dxdy = \frac{P_1 a^3 - [Ra^2 + 6M_{xT}(c_3+d)](a-c_3-d)}{a^3} \quad (39)$$

2.3.3. Bidirectional shear force (penetration shearing)

The critical section for the bidirectional shear force appears at a "*d/2*" distance from the edge of the column in both directions, as shown in Figure 7.

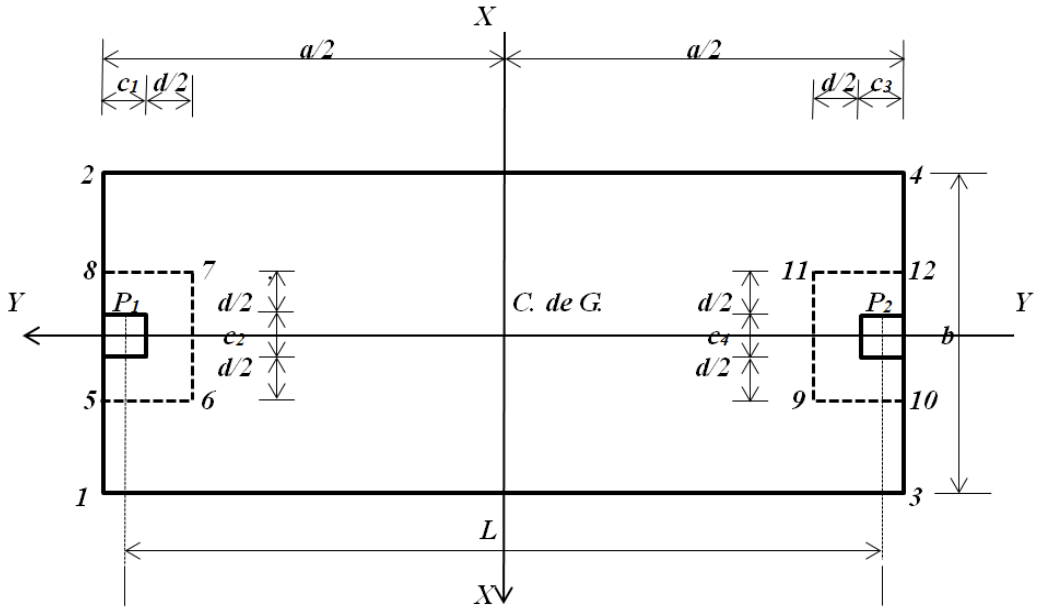

Figure 7. Critical sections for the bidirectional shear forces

2.3.3.1. Penetration shear force for column 1

The penetration shear force of column 1 "V_{p1}" that acts on the footing is the "P_1" force minus the rectangular area formed by points 5, 6, 7, and 8 as is shown below:

$$V_{p1} = P_1 - \int_{\frac{a}{2}-c_1-\frac{d}{2}}^{\frac{a}{2}} \int_{-\frac{c_2}{2}-\frac{d}{2}}^{\frac{c_2}{2}+\frac{d}{2}} \sigma(x,y)dxdy$$

$$= \frac{P_1 a^3 b - \left[Ra^2 + 6M_{xT}\left(a - c_1 - \frac{d}{2}\right)\right](c_2+d)\left(c_1+\frac{d}{2}\right)}{a^3 b} \quad (40)$$

2.3.3.2. Penetration shear force for column 2

The penetration shear force of column 2 "V_{p2}" that acts on the footing is the "P_2" force minus the rectangular area formed by points 9, 10, 11, and 12 as is shown below:

$$V_{p2} = P_2 - \int_{-a/2}^{-a/2+c_3+d/2} \int_{-c_4/2-d/2}^{c_4/2+d/2} \sigma(x,y)dxdy = \frac{P_2 a^3 b - [Ra^2 - 6M_{xT}(a - c_3 - d/2)](c_4 + d)(c_3 + d/2)}{a^3 b} \quad (41)$$

3. NUMERIC EXAMPLE

The design of a combined boundary footing with two restricted opposite sides that supports two square columns is shown in Figure 2, along with the following basic information : Column 1 = 40x40 *cm;* Column 2 = 40x40 *cm; L* = 5.60 *m; H* = 2.0 *m;* P_{D1} *= 600 kN;* P_{L1} *= 400 kN;* M_{Dx1} *= 140 kN-m;* M_{Lx1} *= 100 kN-m;* M_{Dy1} *= 120 kN-m;* M_{Ly1} *= 80 kN-m;* P_{D2} *= 500 kN;* P_{L2} *= 300 kN;* M_{Dx2} *= 120 kN-m;* M_{Lx2} *= 100 kN-m;* M_{Dy2} *= 110 kN-m;* M_{Ly2} *= 90 kN-m;* f'_c *= 21 MPa;* f_y *= 420 MPa;* q_a *= 220 kN/m*^{2}*;* γ_{ppz} *= 24 kN/m*^{3}*;* γ_{pps} *= 15 kN/m*^{3}.

Where: *H* is the depth of the footing, P_D is the dead load, P_L is the live load, M_{Dx} is the moment around the "X-X" axis of the dead load, M_{Lx} is the moment around the "X-X" axis of the live load, M_{Dy} is the moment around the "Y-Y" axis of the dead load, and M_{Ly} is the moment around the "Y-Y" axis of the live load.

The design is done using the criterion of last resistance, and is obtained through the procedure used by Luévanos-Rojas (2014b).

Step 1: The loads and moments that act on the ground are: P_1 = 1000 *kN;* M_{x1} = 240 *kN-m;* M_{y1} = 200 *kN-m;* P_2 = 800 *kN;* M_{x2} = 220 *kN-m;* M_{y2} = 200 *kN-m; R* = 1800 *kN;* M_{yT} *= 400 kN-m;* M_{xT} = 1020 *kN-m.*

Step 2: The available load capacity of the ground: a thickness "*t*" of the footing is proposed, the first proposal is a minimum thickness of 25 cm in accordance with the ACI regulation; subsequently, the thickness is revised to comply with the conditions: moments, flexural shearing, and penetration shearing. If these conditions are not complied with, a greater thickness is proposed until the three aforementioned conditions are met. The thickness of the footing that complies with the three conditions mentioned above is of 85 cm. Using equation (6) the available load capacity of the ground is obtained "σ_{adm}", which is of 182.35 *kN/m*^{2}.

Step 3: The value of "*a*" by equation (2) is obtained as: *a* = 6.00 *m*. The value of "*b*" by equation (4) is obtained as: *b* = 3.08 *m*, and by equation (5) it is obtained as: *b* = 3.25 *m*. Therefore, the dimensions of the footing are: *a* = 6.00 *m* and *b* = 3.30 *m*.

Step 4: The mechanical elements (P, M_x, M_y) that act on the footing are factorized: P_{u1} = 1360 *kN;* M_{ux1} = 328 *kN-m;* M_{uy1} = 272 *kN-m;* P_{u2} = 1080 *kN;* M_{ux2} = 304 *kN-m;* M_{uy2} = 276 *kN-m; R* = 2440 *kN;* M_{uyT} *= 548 kN-m;* M_{uxT} = 1416 *kN-m.*

Step 5: The moments that act on the footing. The moments around the axes parallel to the Y-Y axis are: $M_{a\text{-}a}$ = 544.64 *kN-m;* $M_{b\text{-}b}$ = 457.08 *kN-m.* The moments around the axes parallel to the X-X axis are: $M_{c\text{-}c}$ = –549.43 *kN-m;* $M_{d\text{-}d}$ = –1652.53 *kN-m;* $M_{e\text{-}e}$ = +102.49 *kN-m.*

Step 6: The effective depth (effective cant). The effective cant for the maximum moment of the axes parallel to the Y-Y axis is: *d* = 37.61 *cm*. The effective cant for the maximum moment of the axes parallel to the X-X axis is: *d* = 31.95 *cm*. The effective depth after different proposals is: *d* = 77.00 *cm*, *r* = 8.00 *cm*, *t* = 85.00 *cm*.

Step 7: The flexural shear force (unidirectional shear force). The shear forces in the axes parallel to the Y-Y axis, the permissible flexural shear force is: $\emptyset_v V_{cf}$ = 400.26 *kN;* the acting flexural shear forces are: $V_{ff\text{-}f}$ = 361.15 *kN;* $V_{fg\text{-}g}$ = 304.64 *kN*. Therefore, it complies. The shear forces on the axes parallel to the

X-X axis, the permissible flexural shear force is: $\emptyset_v V_{cf}$ = 1682.60 *kN;* the acting flexural shear forces are: $V_{fh\text{-}h}$ = 1176.23 *kN;* $V_{fg\text{-}g}$ = – 826.48 *kN*. Therefore, it complies.

Step 8: The penetration shear force (bidirectional shear force). The permissible penetration shear force is: $\emptyset_v V_{cp}$ = 4191.22 *kN;* $\emptyset_v V_{cp}$ = 7114.75 *kN;* $\emptyset_v V_{cp}$ = 2711.96 *kN*. The acting penetration shear force is: for column 1: V_{cp1} = 1189.73 *kN*; for column 2: V_{cp2} = 1023.91 *kN*. Therefore, it complies.

Step 9: The reinforcing steel. w = 0.0425.

a) The longitudinal reinforcing steel (reinforcing steel in the direction of the "*Y*" axis).

- Reinforcing steel in the upper part: A_{sp} = 58.35 cm^2. A_{smin} = 84.62 cm^2. Therefore, minimum steel by flexure is suggested "A_{smin}". Use 17 rods of 1" (2.54 *cm*) in diameter.
- The reinforcing steel in the lower part: A_{sp} = 3.53 cm^2. A_{smin} = 84.62 cm^2. Therefore, minimum steel by flexure is suggested "A_{smin}". Use 17 rods of 1" (2.54 *cm*) in diameter.

b) The transversal reinforcing steel (reinforcing steel in the direction of the "*X*" axis):

- The reinforcing steel in the lower part: Under column 1: A_{sp} = 19.45 cm^2. A_{smin} = 20.13 cm^2. Therefore, minimum steel by flexure is suggested "A_{smin}". Use 8 rods of 3/4" (1.91 *cm*) in diameter. Under column 2: A_{sp} = 16.22 cm^2. A_{smin} = 20.13 cm^2. Therefore, minimum steel by flexure is suggested "A_{smin}". Use 8 rods of 3/4" (1.91 *cm*) in diameter.
- The reinforcing steel in the excess part of the columns: Steel by temperature is suggested: A_{st} = 0.0018$b_w t$ = 67.78 cm^2. Use 24 rods of 3/4" (1.91 *cm*) in diameter.
- Reinforcing steel in the upper part: Steel by temperature is suggested: A_{st} = 0.0018$b_w t$ = 91.80 cm^2. Use 33 rods of 3/4" (1.91 *cm*) in diameter.

Step 10: The longitude of the development for corrugated bars:

a) Reinforcing steel in the upper part

where: ψ_t = 1.3 as it has more than 30 *cm* of fresh concrete under the reinforcement, $\psi_e = \lambda = 1$.

$$l_d = \frac{f_y \psi_t \psi_e}{1.7\lambda\sqrt{f'_c}} d_b = \frac{(420)(1.3)(1)}{1.7(1)\sqrt{21}}(2.54) = 178.02\ cm$$

$$y_m = 0.5019\ m$$

The available length in the longitudinal direction of the footing is: 300 – 50.19 – 8 = 241.81 *cm.*
Thus, the developmental length is lower than the available length. Therefore, a hook is not required.

b) Reinforcing steel in the lower part

where: ψ_t = 1, $\psi_e = \lambda = 1$.

$$l_d = \frac{f_y \psi_t \psi_e}{2.1\lambda\sqrt{f'_c}} d_b = \frac{(420)(1)(1)}{2.1(1)\sqrt{21}}(1.91) = 83.36\ cm$$

The available length in the longitudinal direction of the footing is: 330/2 – 40/2 – 8 = 137 *cm.*
Therefore, the developmental length is lower than the available length. Therefore, a hook is not required.
The dimensions and the reinforcing steel of the rectangular boundary footing that supports two square columns with two restricted opposite sides are shown in Figure 8.

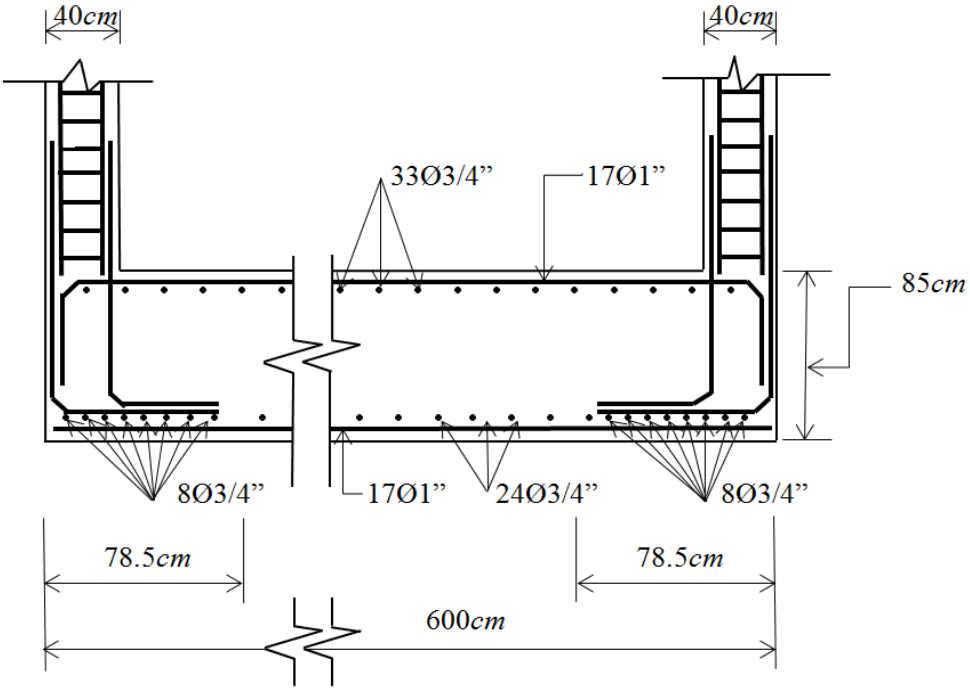

Figure 8. Final design of the combined rectangular footing

4. CONCLUSIONS

The model presented in this document is only applicable for the design of rectangular combined boundary footings with two restricted opposite sides that support two columns. It is assumed that the ground under the footing is of an elastic and homogeneous material, and that the footing is rigid, which complies with the expression of the bidirectional flexure, meaning, the variation of the pressure is linear.

The equations proposed directly offer the dimensions in the layout of the foundation, guaranteeing that the permissible pressure in the ground will not be exceeded. On the other hand, the mechanical elements for moments, flexural shear force (unidirectional shear force), and penetration shear force (bi-directional shear force) can also differ from the ones obtained with a constant ground pressure. In this work, we also propose expressions to obtain these design elements in a systematic manner.

The model proposed in this document can be applied to the three types of rectangular combined boundary footings with two restricted opposite sites in terms of the loads applied to each column: 1) concentric axial load, 2) Axial load and moment in one direction (unidirectional bending), 3) Axial load and moment in two directions (bidirectional bending).

Suggestions for future investigations: 1) When the rectangular combined boundary footings with two restricted opposite sides support more than two columns; 2) When another type of soil is present, for example, in the case of completely cohesive soils (clay soils) and completely granular soils (sandy soils), the pressure diagram is not linear and they must be treated in a different manner (Figure 1); 3) In the event that only a portion of the base of the foundation generates compression on the ground, with only a portion of its contact surface working—which is allowed in some hypotheses of infrequent loads, especially in the foundations of industrial equipment, the solution of which is iterative (Bowles, 1970).

5. REFERENCES

ACI (2013), "*Building Code Requirements for Structural Concrete and Commentary*", (New York, USA: American Concrete Institute, Committee 318).
Bowles, J. E. (1970), "*Engineering properties of soils and their measurement*", (New York, USA: McGraw-Hill).
Bowles, J. E. (1996), "*Foundation analysis and design*", (New York, USA: McGraw-Hill).
Calavera-Ruiz, J. (2000), "*Cálculo de estructuras de cimentación*", (Distrito Federal, México: Intemac ediciones).
Das, B. M., Sordo-Zabay, E., Arrioja-Juárez, R. (2006), "*Principios de Ingeniería de Cimentaciones*", (Distrito Federal, México: Cengage Learning Latín América).
Gere, J. M., Goodo, B. J. (2009), "*Mecánica de materiales*", (Distrito Federal, México: Cengage Learning).
González-Cuevas, O. M., Robles-Fernández-Villegas, F. (2005), "*Aspectos fundamentales del concreto reforzado*", (Distrito Federal, México: Limusa).
Kurian, N. P. (2005), "*Design of foundation systems*", (New Delhi, India: Alpha Science Int'l Ltd.).
Luévanos-Rojas, A., Faudoa-Herrera, J. G., Andrade-Vallejo, R. A., Cano-Alvarez, M. A. (2013), "*Design of isolated footings of rectangular form using a new model*", International Journal of Innovative Computing, Information and Control, Vol. 9, No. 10, pp. 4001-4022.
Luévanos-Rojas, A. (2014a), "*Design of isolated footings of circular form using a new model*", Structural Engineering and Mechanics, Vol. 52, No. 4, pp. 767-786.
Luévanos-Rojas, A. (2014b), "*Design of boundary combined footings of rectangular shape using a new model*", Dyna-Colombia, Vol. 81, No. 188, pp. 199-208.
McCormac, J. C. Brown, R. H. (2013), "*Design of reinforced concrete*", (New York, USA: John Wiley & Sons).
Nilson A. H. (1999), "*Diseño de estructuras de concreto*", (Distrito Federal, México: McGraw-Hill).
Punmia, B. C., Kumar-Jain, A., Kumar-Jain, A. (2007), "*Limit state design of reinforced concrete*", (New Delhi, India: Laxmi Publications (P) Limited).
Tomlinson, M. J. (2008), "*Cimentaciones, diseño y construcción*", (Distrito Federal, México: Trillas).
Varghese, P. C. (2009), "*Design of reinforced concrete foundations*", (New Delhi, India: PHI Learning Pvt. Ltd.).

ALCONPAT Journal, Volume 6, Issue 2, may – august 2016, Pages 190 – 201

ALCONPAT Journal

www.revistaalconpat.org

eISSN 2007-6835

Journal of the Latin-American Association of Quality Control, Pathology and Recovery of Construction

Experimental analysis of various configurations of metal sheets in the reinforcement of flexion of reinforced concrete beams

C. C. Deghenhard[1], T. Teixeira[1], A. Vargas[1], M. Vito[1], Â. C. Piccinini[1], B. Do Vale Silva[1]

[1] Civil Engineering Department; Laboratorio Experimental de Estructuras (LEE); Universidad de Extremo Sul Catarinense (UNESC) - Criciúma/SC; Brazil.

Article information
DOI:
http://dx.doi.org/10.21041/ra.v6i2.137
Article received on November 28th 2015, reviewed under publishing policies of ALCONPAT journal and accepted on February 20th 2016. Any discussion, including the replica of the authors, shall be published in the first number of the year 2017 as long as the information is received prior to the closing of the third number of the year 2016.

ABSTRACT

The external structural reinforcing steel, in the way of steel sheets attached with epoxy adhesive, is an option to increase the load capacity of reinforced concrete elements. This study evaluated concrete beams reinforced with steel sheets SAE 1020 of different thicknesses (0.75, 1.50, and 2.25 mm), longitudes (80 and 150 cm), and configurations (U-shape or flat) with the purpose of reviewing and comparing the best practices with sheets adhered to the structural reinforcement. Twenty-one beams were built with a cross-section of 12 x 20 cm and a longitude of 200 cm, with C25 concrete, and flexion frame with 2 Ø10 mm. The beams where subject to a four-point flexural test, which allowed analyzing the optimal loads and vertical displacements. Thus, a comparison relative to the performance of the beams is presented.
Keywords: structural reinforcement; cast steel plates; reinforced concrete beams.

RESUMO

O reforço estrutural externo com chapa metálica colada com adesivo epóxi é uma opção que possibilita aumentar a capacidade de carga em elementos de concreto armado. Este trabalho avaliou experimentalmente vigas de concreto armado com reforço de chapas de aço SAE 1020 de diferentes espessuras (0,75; 1,50 e 2,25 mm), comprimentos (80 e 150 cm) e configurações (perfil U ou simplesmente plana) com intuito de revisar e comparar as melhores práticas de reforço estrutural com chapa colada. Foram fabricadas 21 vigas com seções transversais de 12x20 cm e comprimento de 200 cm, utilizando concreto C25 e armadura de flexão com 2 Ø10 mm. As vigas foram submetidas a ensaios de flexão em 4 pontos, o que permitiu analisar as cargas últimas e deslocamentos verticais. Como resultado, apresenta-se um comparativo de desempenho das vigas.
Palavras-chave: reforço estrutural; chapa de aço colada; vigas de concreto armado.

RESUMEN

El acero de refuerzo estructural externo, a través de chapas de acero pegadas con adhesivo epóxico, es una opción para incrementar la capacidad de carga de elementos de concreto reforzado. En este estudio se evaluaron vigas de concreto reforzadas con chapas de acero SAE 1020 de diferentes espesores (0.75, 1.50 y 2.25 mm), longitudes (80 and 150 cm) y configuración (en forma de U o plana) con el propósito de revisar y comparar las mejores prácticas con chapas pegadas al refuerzo estructural. Se elaboraron 21 vigas construidas con una sección trasversal de 12 x 20 cm y una longitud de 200 cm, con concreto C25 y armadura de flexión con 2 Ø10 mm. Las vigas fueron sometidas a ensayos de flexión en 4 puntos, lo que permitió analizar las cargas últimas y desplazamientos verticales. Como resultado, se presenta una comparación relativa al desempeño de las vigas.
Palabras clave: refuerzo estructural; placas de acero coladas, vigas de concreto reforzado.

Corresponding author: Bruno do Vale Silva (dovalesilva@unesc.net)

1. INTRODUCTION

The condition for the recuperation services and the reinforcement of the concrete structures depends on the precise analysis of the causes that make these necessary, as well as on a detailed study of the effects produced. In some cases, to guarantee the stability of the construction, there is need for structural rehabilitation or reinforcement (Silva Filho and Helene, 2011; Jumaat and Alam, 2008). Having clarified this factor, the adequate technique is chosen, which includes the careful selection of the material and equipment to be used, as well as the necessary labor for the execution of the work. Reinforcement is characterized as an activity specific for the cases in which the resistance and/or rigidity of a structure is sought to be increased. (Helene, 2000; Alfaiate and Costa, 2004; Tisot, 2010).

Reinforcement by the external addition of casted metal sheets is characterized by the bond of the surface of the concrete with steel sheets, using a resin with a high adhesion capacity and mechanical resistance. This is an option for the reinforcement of concrete elements, it is quick and simple to execute, and it is mainly recommended when it is necessary to reinforce the structure within a short time, or when it is not possible to make significant changes in the geometry of the piece (Campagnolo et al., 1994; Santos, 2008; Aykac et al., 2013). At the end of the processes, a structural element comprised of concrete-resin-steel is obtained, which provides the structure with a higher resistance than the requested efforts. Consequently, a more rigid element is obtained that deforms a little before starting to collapse. It is fundamentally important that the resin utilized to bind the concrete-steel is of proven quality and that the surface of the concrete and steel have been duly prepared (Cánovas, 1998; Cánovas, 1985). The adhesion to bind the metallic sheets is done using epoxy resins, because they show an adequate modulus of rigidity and excellent adhesive properties with concrete and steel, as well as low retraction during the curing process, all of which guarantees the integrity of the contact surface (Melo Júnior, 1997; Patiño, 2005; Simões, 2007).

The adherence between concrete-resin-steel is primordial for the good functioning of the reinforcement, as it provides the transference of stress between the elements. Studies done show different solutions to prevent types of rupture due to failure in adherence and the separation of the sheet, for example: an increase in the relation width/thickness of the sheet; finishing of the sheets close to the supports; and the use of anchor bolts and other devices to anchor the sheets (Oehlers, 1990; Hussain, 1995; Ali, 2005; Simões, 2007; Narayanamurthy, 2012). Another important factor to improve the durability of the reinforcement is to carry out a treatment with anticorrosive paint on the external surfaces of the sheet that are not in contact with the epoxy resin (Souza; Ripper, 1988). In this context, the selection of the adequate configurations and techniques are fundamentally important for the good mechanical performance of the structural reinforcement (Perelles et al., 2013), in addition to providing a better cost/benefit relation on the rehabilitation process of the structure.

The objective of this study is to experimentally evaluate the carrying capacity of reinforced concrete beams with different configurations of metallic reinforcement using steel sheets SAE 1020: i) different thicknesses (0.75 mm, 1.50 mm, and 2,25 mm); ii) longitudes (80 cm and 150 cm); and iii) either a U-shape or flat. The end goal is to review and compare the practical improvements of structural reinforcement with casted sheets.

2. EXPERIMENTAL PROCEDURE

Twenty-one beams with 12x20 cm cross-sections and a longitude of 200 cm were casted out of concrete with an average resistance to compression of 25 MPa at 28 days of age, and the reinforcement used steel CA-50 with 2xØ = 10 mm (power 3 – x/d = 0.2893). The abutments utilized had Ø=5 mm and a spacing of 10 cm. Figure 1 shows the details of the reinforcement used on the beams.

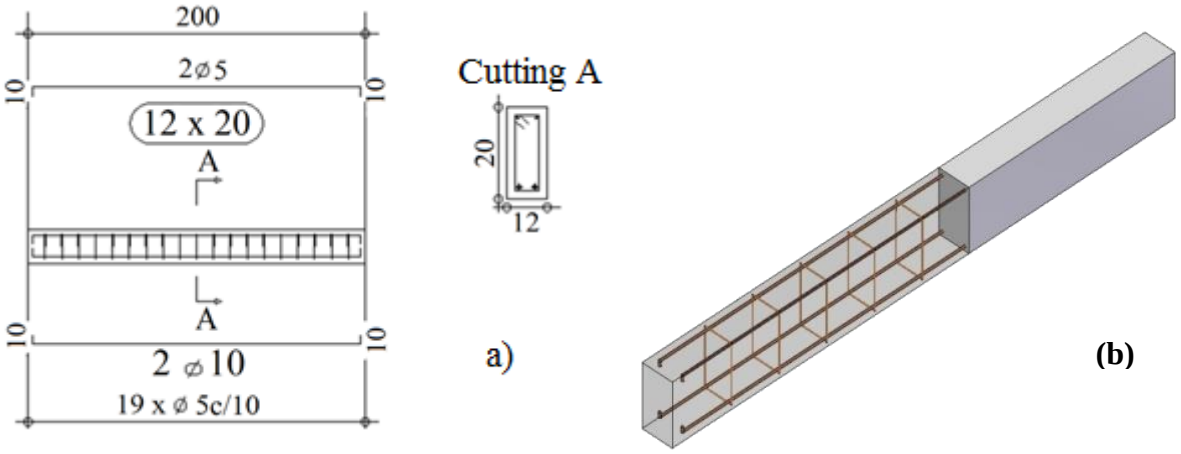

Figure 1. Details of the reinforcement on the beams – (a) Longitudinal detail; (b) Perspective of the reinforcement.

The beams were casted using immersion vibrators, using 2.5 cm plastic separators to ensure the coating of the reinforcement. Figure 2 shows the manufacturing sequence of the beams.

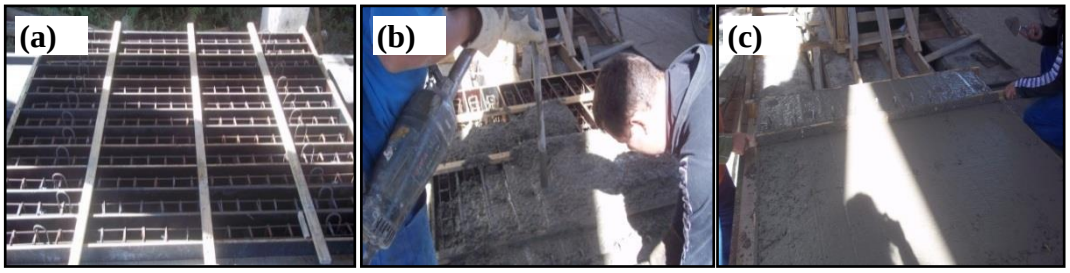

Figure 2. Manufacture of the reinforced concrete beams – (a) Molds with the reinforcement ready for casting; (b) Casting and vibration; (c) Leveling of the concrete in the molds.

The uncasing processes of the beams took place after 7 days. At 28 days, the beams were subjected to four-point flexural tests, which permitted the analysis of the final loads and vertical displacements. For the control of the resistance to compression of the concrete, 12 cylindrical (cps) test tubes were casted (Ø10x20 cm) to be tested at 7 and 28 days (3 cps per age/2 castings), and a slump-test was carried out to verify the workability of the concrete. The beams were divided into 7 groups with 3 samples each, as shown on Table 1. The beams from groups A, B, C, and D were manufactured in the same cast as the beams from groups E, F, and G, though with different castings. The beams of groups A and E were taken as reference for each casting. Groups E, F, and G were prepared using the most satisfactory result among the thicknesses of the sheets for groups B, C, and D.

Table 1. Distribution of the groups of reinforced concrete beams.

Reference beams without reinforcement	Beams with straight sheets with different thicknesses	Beams with U-shape sheets with different longitudes
Group A	Group B (0.75 mm)	Group F (150 cm)
Group E	Group C (1.50 mm)	Group G (80 cm)
-	Group D (2.25 mm)	-

2.1 Application of the reinforcement – 1st stage: straight sheets with different thicknesses.

To implement the structural reinforcement, steel sheets SAE 1020 with a width of 12 cm and a longitude of 150 cm were used. The structural adhesive utilized was EP, an epoxy-based bicomponent of the Bautech® brand with the following characteristics: high adhesion, chemical and mechanical resistance, pre-dosage material, impermeable to water and oil, in addition to an initial hardness after 12 hours, and total curing in 7 days. The application of the epoxy structural adhesive on the beams followed the supplier's recommendations, starting with the preparation of the substrate in which the application surface was cleaned of dust, oils or any substance that could damage the adhesion, carrying out this process with the use of a steel brush. The preparation of the epoxy structural adhesive was done through the homogenization of the components separated by hand. Subsequently, component B (hardener) was added to component A (resin), mixing for 5 minutes. The application of the epoxy structural adhesive was done with the help of a spatula over the entire surface to be casted, with a minimum thickness of 2 mm and a yield of approximately 0.7 kg/m^2.

Before the application of the adhesive, grooves were made on the steel sheets with an electric sander to improve the adherence conditions along with the concrete surface. After fixing the sheets, they are subject to a quick and uniform pressure as to eliminate the excess resin. This pressure is applied with a rubber mallet. Subsequently, concrete blocks are placed at the extremes and on the region of the sheets, maintaining this for 7 days while covered with a plastic canvas. The application of the epoxy structural adhesive on the main beams was done at 21 days, and the flexural test at 28 days after casting. The substrate preparation stages of the epoxy structural adhesive, as well as the application of the steel sheets on the beams can be seen on Figure 3.

Figure 3. (a) Preparation of the sheets; (b) Application of the epoxy structural adhesive; (c) Fixing and support of the sheets.

2.2 Application of the reinforcement – 2nd stage: profile of the U-shaped steel with equal thickness.

From the results obtained with the tests of groups B, C, and D, the beams of groups F and G were prepared and reinforced with the steel profile SAE 1020, with a base of 12 cm, and wings with a height of 15 cm and a thickness of 0.75 mm (U-shaped profile); with group F having a longitude of 150 cm and group G having a longitude of 80 cm. The difference in the longitude of the sheets was premeditated to evaluate the area with the greatest concentration of stress, which is on the application points of the load, that is, on the central third of the beam.

The adhesive utilized was the same as the one described on point 2.1. The application can be seen in Figure 4, having been carried out in accordance with the manufacturer's specifications for the two

longitudes of the profile: (i) execution of the grooves on the surface of the steel for a better adherence between the profile and the surface of the concrete; (ii) concrete surface without dust or oil, or any substance that could affect the adhesion, cleaned with the use of a steel brush; (iii) mixture of components A (resin) and B (Hardener), made within 5 minutes; (iv) application of the epoxy adhesive on the beams using a minimum thickness of 2 mm; (v) placement of the fasteners (sergeants) so that the steel profile can be pressed as close as possible to the beam, favoring the adherence of the profile to the concrete. This system was maintained for 7 days.

Figure 4. (a) Application of the epoxy adhesive to anchor the steel profiles; (b) Placement of the fasteners; (c) Final fastening system of the sheets.

2.3 Four-point flexural test

It can be observed in Figure 5 that the beams are placed on a metal portico, where the load was applied through a hydraulic cylinder with a capacity of 500 kN, transferred to the central thirds of the beam through the metal profile while supported on two wooden rolls. The load increment values throughout the tests were obtained from a load cell positioned on the base of the cylinder. The displacements in the central span of the beam were measured from the 2 inductive displacement transducers (LVDTs) with a reading capacity of 100 mm, which were placed on the opposite sides of the central span of the beam to obtain the average of the values for a better consideration of the central displacement of the beam. To acquire the data the Quantum X® system was used, which utilizes the Catman Easy® software, both having the HBM brand.

The verifications were done to analyze the behavior of each group at different instances of load application: (i) at the maximum displacement (L/250) allowed by the standard ABNT NBR 6118:2014; (ii) at the rupture load; (iii) separation of the sheet and breakage mode.

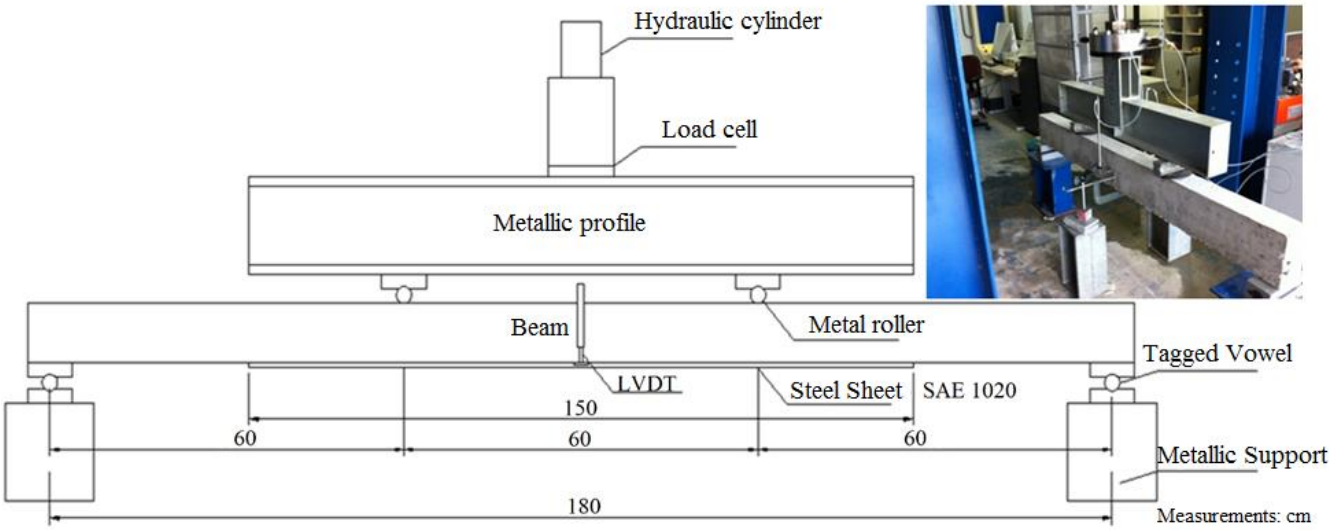

Figure 5. Schematic drawing and photo of the four-point flexural test.

3. RESULTS AND DISCUSSIONS

The result of the settling was of 11.0 cm for the concrete of groups A, B, C and D, and 10.0 cm for the concrete of groups E, F, and G. The results obtained from the tests on the axial resistance to compression, in accordance with the ABNT 5739:2007, are indicated in Table 2.

Table 2. Results of the resistance to compression of the test tubes of each group of beams.

Groups	Age (days)	Test tube	*fc* (MPa)	*fcm* (MPa)	Standard deviation
A, B, C, and D	7	1	21.5	21.2	2.0
		2	23.0		
		3	19.1		
	28	4	24.1	25.2	1.3
		5	26.5		
		6	25.0		
E, F, and G	7	7	18.1	21.4	3.0
		8	24.0		
		9	22.0		
	28	10	30.0	29.7	1.8
		11	27.8		
		12	31.3		

3.1 Results – 1st stage: straight sheets with different thicknesses.

When applying the load until reaching the maximum displacement stablished by the standard ABNT NBR 6118:2014, it was observed that the groups showed disparities in the resistance values as presented in Table 3. Group A is the reference for the analysis and interpretation of the results in general, due to being beams without reinforcement. In this manner, groups B, C, and D reached higher average loads for the maximum admissible displacement (7.20 mm), with group B being 36% higher in relation to Group A. Likewise, group C showed a 30% increase, and group D reached a 26% higher load for the determined displacement.

Table 3. Results of the load in the maximum displacement allowed by the standard (L/250).

Group	Beams	Load (kN)	Arrow (mm)
A	A1	38.6	7.2
	A2	42.8	7.2
	A3	42.6	7.2
	Average	41.4	-
	Standard deviation	2.4	-
B	B1	58.1	7.2
	B2	56.9	7.2
	B3	53.3	7.2
	Average	56.1	-
	Standard deviation	2.5	-
C	C1	54.1	7.2
	C2	53.4	7.2
	C3	-	7.2

	Average	53.8	-
	Standard deviation	0.5	-
D	D1	-	7.2
	D2	51.2	7.2
	D3	53.2	7.2
	Average	52.2	-
	Standard deviation	1.4	-

The largest load increase was of 36%, lower than the maximum of 50% recommended by Souza and Ripper (1998). The growing load and the displacements reached in the breakage are presented in Table 4. In this stage, the behavior of the percentages that justify the increase in the bearing capacity between the groups was comparable to the maximum displacement allowed by the standard (L/250). Group B reached a load 29% higher than group A, and the displacements obtained were close between the two groups. Therefore, the final displacements for groups C and D are presented below the regulatory determination, as the beams reached their breaking point abruptly moments after going above the admissible displacement (7.20 mm). The load of group C was 24% higher in comparison to group A, as well as group D, which was of 16%. The behavior of the tests can be observed in Figure 6.

Table 4. Load and displacement results to push the beams to their breaking point.

Group	**Beams**	**Load (kN)**	**Arrow (mm)**
A	A1	48.8	9.7
	A2	51.9	9.4
	A3	51.7	9.9
	Average	50.8	9.7
	Standard deviation	1.7	0.3
B	B1	66.2	9.4
	B2	65.3	9.8
	B3	65.4	10.6
	Average	65.6	9.9
	Standard deviation	0.5	0.6
C	C1	64.1	6.1
	C2	61.8	5.9
	C3	-	-
	Average	63.0	6.0
	Standard deviation	1.6	0.1
D	D1	-	-
	D2	55.1	3.6
	D3	63.1	4.2
	Average	59.1	3.9
	Standard deviation	5.6	0.4

The beams of groups C and D do not have the same tendency in the graph (Figure 6), reaching breaking point at 62.96 kN in group C and 59.10 kN in group D. In these two groups, the breakage of the reinforcement occurred abruptly on one of the extremes of the beams, tearing down with it a portion of concrete with the casted steel sheet, which reached all the way up to the positive reinforcement. These breakages occurred before having reached the admissible displacement limit (L/250).

Images of the beams are shown in Figure 7 to demonstrate the separation of the sheets and the means of breakage during the execution of the tests.

Groups A and B have similar behaviors regarding the emergence of cracks among the central thirds and in the separation of the steel sheet SA 1020 of 0.75 mm. Groups C and D have similar behaviors among them, in relation to the most emphasized cracks, up to the end of the reinforcement and the tearing of the concrete with the sheet up to the bending reinforcement. Considering the non-satisfactory results of groups C and D, a solution could be the introduction of anchoring bolts at the ends of the casted steel sheets SAE 1020, which would help dissipate the accumulation of stress in this region. Figure 8 shows that with the increase of the thickness of the steel sheets SAE 1020, a decrease occurs on the support load of the beams, that is, a decreasing linear behavior.

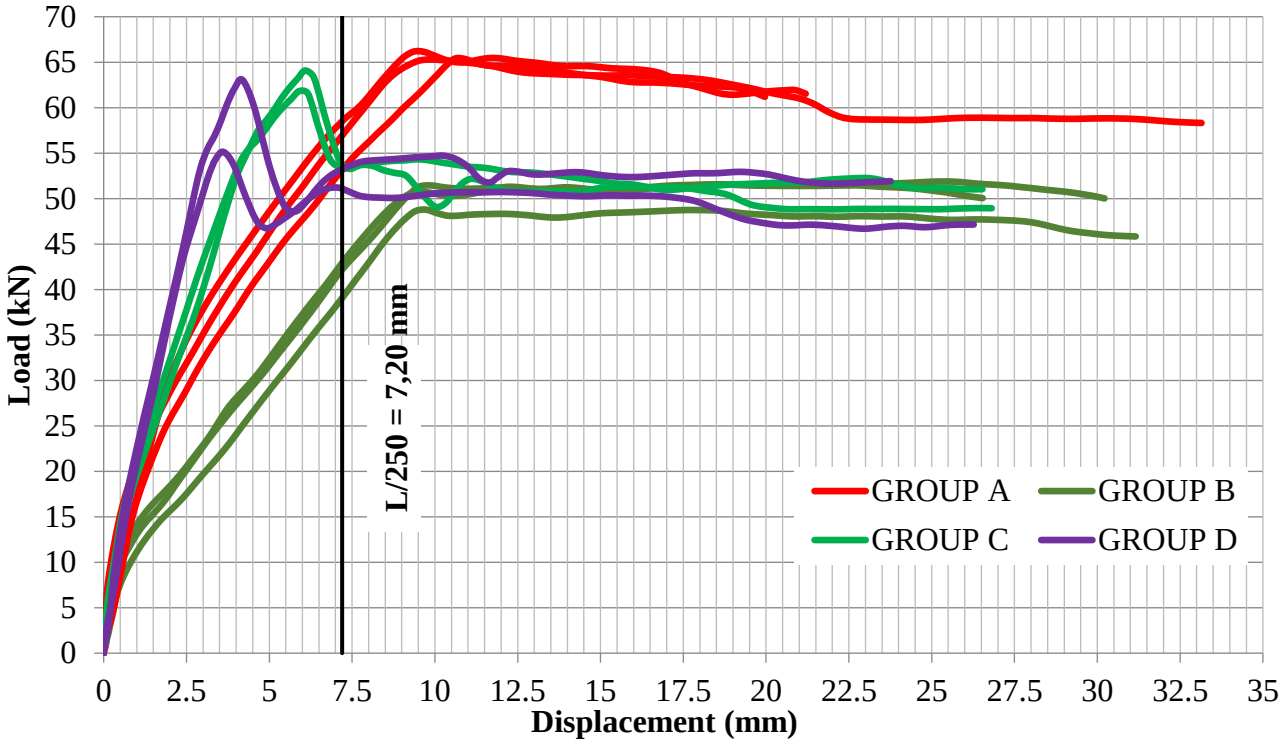

Figure 6. Behavior of the beams of groups A, B, C, and D – load vs displacement.

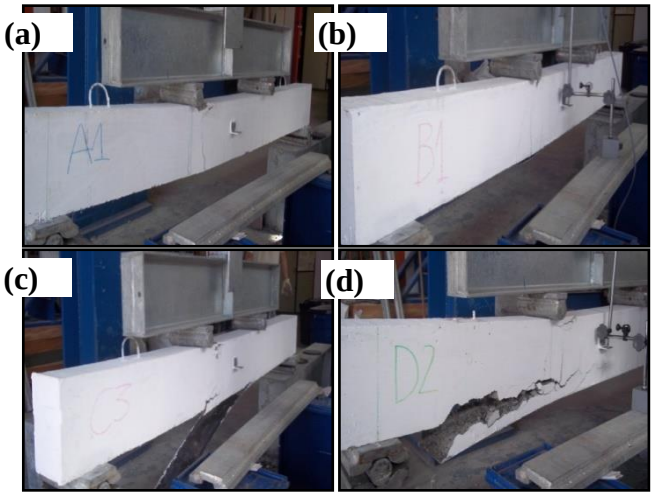

Figure 7. Means of breakage – (a) Group A; (b) Group B; (c) Group C; (d) Group D.

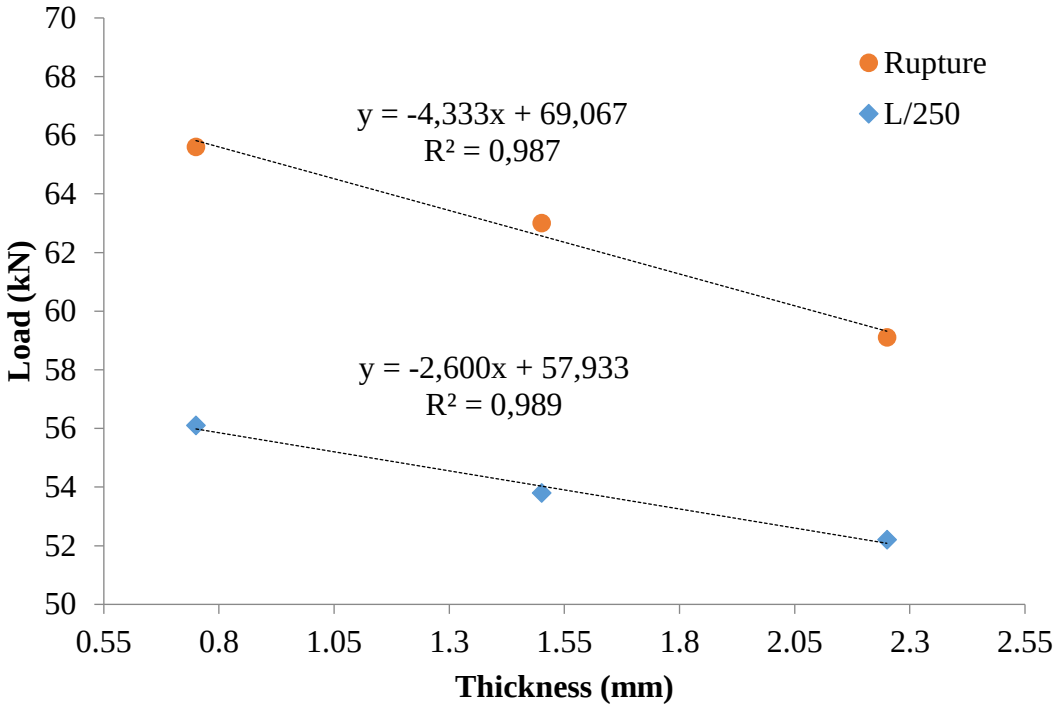

Figure 8. Behavior of the beams of groups B, C, and D – breakage load and load in L/250 *vs* thickness of the steel sheets.

3.2 Results – 2nd stage: U-shaped sheets of equal thicknesses.

In the load of the maximum displacement allowed by the standard (L/250), group F has a 20% increase in the average of the values in relation to group E (reference), whereas group G showed an average increase of 16% (Table 5). It is noted that the group reinforced with the profile with the greater longitude (Group F) has greater efficiency when the resistance to reach the displacement is of 7.2 mm.

The load necessary to push the beams to their breaking point (Table 6) has a greater load increase when compared to group F (150 cm). This group had a 14% increase in resistance, whereas group G decreased the resistance when compared to group E (reference), with a value of 6%. From Figure 9, it is possible to observe the behavior of each group in terms of the load and the respective displacement.

Table 5. Load at the maximum displacement allowed by the standard (L/250).

GROUP E			GROUP F (150 cm)			GROUP G (80 cm)		
Beams	**Load (kN)**	**Arrow (mm)**	**Beams**	**Load (kN)**	**Arrow (mm)**	**Beams**	**Load (kN)**	**Arrow (mm)**
E1	44.2	7.2	F1	43.0	7.2	G1	53.5	7.2
E2	46.0	7.2	F2	61.1	7.2	G2	51.1	7.2
E3	44.9	7.2	F3	57.6	7.2	G3	52.6	7.2
Average	45.0	-		53.9	-		52.4	-
Standard deviation	0.9	-		9.6	-		1.2	-

Table 6. Results of the load and displacements to push the beams to their breaking point.

GROUP E			GROUP F (150 cm)			GROUP G (80 cm)		
Beams	**Load (kN)**	**Arrow (mm)**	**Beams**	**Load (kN)**	**Arrow (mm)**	**Beams**	**Load (kN)**	**Arrow (mm)**
E1	63.4	23.4	F1	61.0	28.7	G1	59.9	18.1
E2	66.3	17.8	F2	82.6	13.1	G2	60.4	11.9
E3	64.3	11.4	F3	77.3	12.6	G3	61.6	8.9
Average	64.6	17.5		73.6	18.1		60.6	13.0
Standard deviation	1.5	6.0		11.3	9.2		0.9	4.7

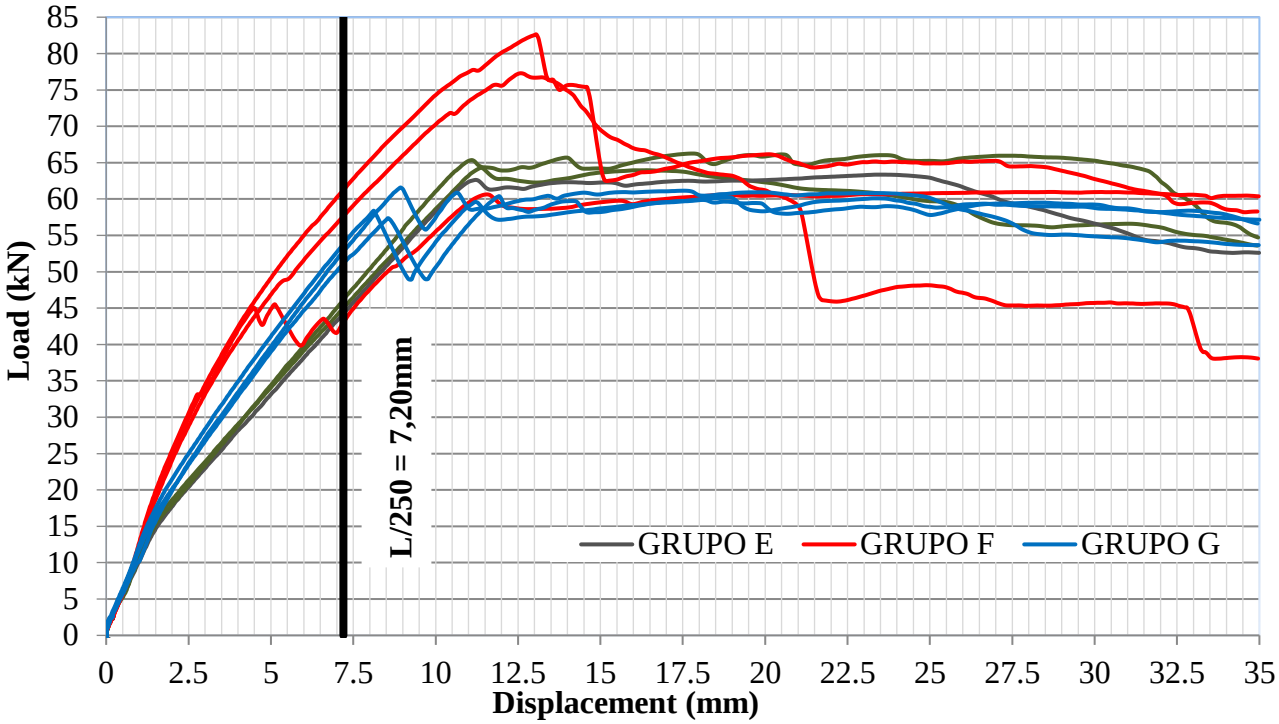

Figure 9. Behavior of the beams from groups E, F, and G – load vs displacement.

The increase in the rigidity of the beam with the addition of the steel sheet is evident. Beam F1 (Figure 10b) behaves differently from the others, as the steel sheet was prematurely separated from the beam, decreasing the increase in stress resistance, and subsequently reaching breaking point with a load of 60.97 kN, not unlike the reference beam of group E. This could possibly be the result of the bad application of the epoxy adhesive, which did not provide a good anchorage of the metal profile to the concrete.

Figure 10. Means of breakage – (a) Group E; (b) Group F; (c) Group G.

It is possible to note the efficiency of the reinforcement of the beams of group F (beams F2 and F3), with the profile of 150 cm, therefore, the separation of the sheet (Figure 9) also occurs with elevated loads. The beams of group B, with the profile of 80 cm, had a behavior that was inferior to group E (reference group). The average displacements were similar among groups E and F, with an average of 17.8 mm, whereas in group G the average displacement was of 13.0 mm. Beam F1 broke due to bending and the separation of the steel profile, followed by the crushing of the concrete in the central region of the beam. Beams F2 and F3 had cracks due to shear stress as well as breakage due to the separation of the steel profile, with crushing of the concrete at the center of beam F2 and on the region close to the support in beam F3. The analysis carried out on the beams of group G, reinforced with a steel rofile with a longitude of 80 cm, showed that they have a cracking behavior similar to group F: breakage by the separation of the steel profile, given that in beams G1 and G3 the breakage of the concrete was close to the central region, and in beam G2 it was close to the support.

4. CONCLUSIONS

Based on the results obtained, it can be concluded that:
(i). The increase in the thickness of the reinforcement with the steel sheet SAE 1020 provided less flexural resistance of the beams, as the sheet thickness of 1.50 mm and 2.25 mm caused the separation of the sheet from the concrete before the normative limit of displacement in L/250 = 7.2 mm. It is worth noting that this fact has certain risks for the implementation of sheets of this thickness. Meanwhile, it could be said that the use of straight sheets with a thickness of 0.75 mm is viable and of quick execution, as there was no need to insert anchorage bolts.
(ii). The use of the profile with 150 cm promoted an increase in the flexural resistance, thus with rupture by lateral separation of the sheet with displacements in the upper central spans at 7.20 mm (L/250). The use of the profile with 80 cm was shown to be unviable due to the premature separation of the sheet immediately after reaching the central displacement of 7.20 mm (L250).
(iii). In general, it can be said that the use of casted sheets without the use of anchorage bolts is viable when the objective is the immediate increase in the bearing capacity of reinforced concrete beams, in addition to the relative low cost of this reinforcement configuration. Therefore, its efficiency is directly correlated to the anchorage of the sheets to avoid their failure by separation. It is worth noting that the parameters linked to durability, such as the corrosion of the steel sheet and the stability of the epoxy resin, were not taken into consideration in this investigation; however, in a real application such parameters must be rigorously considered, especially in relation to cost/benefit for the effective structural safety.

5. REFERENCES

Alfaiate, J., Costa, R. (2004), *"O refuerzo de vigas de betão armado com chapas metálicas coladas com resina"*, Métodos Computacionais em Engenharia, APMTAC, Portugal. pp. 1-13.

Ali, M. S. M., Oehlers, D. J., Bradford, M. A. (2005) *"Debonding of steel plates adhesively bonded to the compression faces of RC beams"*, Construction and Building Materials, V.19, No.6, pp. 413-422.
Associação Brasileira de Normas Técnicas (ABNT). NBR 5739: *Concreto - ensaio de compressão de corpos de prova cilíndricos*. Rio de Janeiro, 2007.
Associação Brasileira de Normas Técnicas (ABNT). NBR 6118: *Projeto de estruturas de concreto*. Rio de Janeiro, 2014.
Aykac, S., Kalkan, I., Aykac, B., Karahan, S., Kayar, S. (2013), "*Strengthening and Repair of Reinforced Concrete Beams Using External Steel Plates"*, Journal of Structural Engineering, V.139, No.6, pp. 929–939.
Campagnolo J. L; Campos Filho A., Silva Filho, L. C. P. (1994), "*Técnicas de ancoragem em vigas de concreto armado reforzadas com chapas de acero coladas*", In: 36a. REIBRAC - Reunión Anual do Instituto Brasileiro do Concreto, 1994, Porto Alegre/ RS.
Cánovas M. F. (1998), *"Patologia e Terapia do Concreto Aramado"*, São Paulo: Editora PINI, 522p.
Cánovas, M. F. (1985), *"Refuerzo de elementos estructurales de hormigón armado mediante encolado de bandas de acero con adhesivos epoxídicos"*, Informes de la Construcción, V.37, No. 373, pp. 27-38.
Helene, P. R. L. (2000) *"Manual para reparo, refuerzo e proteção de estruturas de concreto"*, 2 Ed, São Paulo: Editora PINI, 213 p.
Hussain, M. (1995), "*Flexural behavior of pre-cracked reinforced concrete beams strengthened externally by steel plates*", ACI Structural Journal, V.92, No. 1, pp. 14-23.
Jumaat, M. Z., Alam A. (2008), *Experimental and analytical investigations on the structural behaviour of steel plate and CFRP laminate flexurally strengthened reinforced concrete beams*", Journal of Applied Sciences, V.8, pp. 4383-4389.
Melo Júnior, L. O. (1997), *"Comportamento ao cisalhamento de vigas em concreto armado reforzadas com chapas de acero coladas lateralmente"*, Mestrado em Engenharia Civil, Universidade Federal de Pernambuco (UFPE), Recife/PE, 81p.
Narayanamurthy, V., Chen, J. F., Narayanamurthy, J., Cairns, D.J., Oehlers, D.J. (2012) *"Plate end debonding in the constant bending moment zone of plated beams"*, Composites Part B: Engineering, V.43, No. 8, pp. 3361-3373.
Oehlers, D., Moran, J. (1990), *"Premature failure of externally plated reinforced concrete beams"*, Journal of Structural Engineering, V.116, No. 4, pp. 978-995.
Patiño, A. L. (2005) *"Comportamiento mecánico de vigas de hormigón armado reforzadas con bandas encoladas con resinas epoxi"*, Tesis Ingeniería Civil, Universidad Politécnica de Madrid (UPM), 323p.
Perelles, D. H., Medeiros, M. F., Garcez, M. R. (2013), "*Aplicação da análise hierárquica como ferramenta de tomada de decisão para escolha do compósito de refuerzo com polímeros reforçados com fibras*", Revista ALCONPAT, V.3, No. 3, pp. 165-180.
Santos, P. M. (2008), *"Comparação de refuerzo com chapas de acero e fibras de carbono em vigas de concreto armado submetida à flexión simples"*, Trabalho de Final de Curso em Engenharia Civil, Universidade Estadual de Feira de Santana (UEFS), Feira de Santana/BA.
Silva Filho L. C. P., Helene P. R. L. (2011), *"Análises de estruturas de concreto com problemas de resistência e fissuração"*, In.: Isaia G. C., Concreto: Ciência e Tecnologia. 1ª Edição. São Paulo: Editora IBRACON, V.2, Cap.32, pp. 1124-1174.
Simões, M. L. F. (2007), *"Refuerzo à flexión de vigas de concreto armado por encamisamento parcial"*, Mestrado em Engenharia Civil, Universidade Federal do Rio de Janeiro (UFRJ), Rio de Janeiro/RJ, 162p.
Souza, V. C. M., Ripper, T. (1988), *"Patologia, recuperação e refuerzo de estruturas de concreto"*, São Paulo: Editora PINI, 255 p.
Tisot, G. D. D. (2010), *"Refuerzo à flexión de vigas de concreto armado submetidas a carregamento precoce"*, Trabalho de Conclusão de Curso em Engenharia Civil, Universidade de Passo Fundo (UPF), Passo Fundo/RS.